



**APPLICATION OF A
FINITE-VOLUME TIME-DOMAIN
MAXWELL EQUATION SOLVER
TO THREE-DIMENSIONAL OBJECTS**

THESIS

Frederick G. Harmon, Captain, USAF

AFIT/GE/ENG/96D-06

DISTRIBUTION STATEMENT A

Approved for public release;
Distribution Unlimited

**DEPARTMENT OF THE AIR FORCE
AIR UNIVERSITY
AIR FORCE INSTITUTE OF TECHNOLOGY**

Wright-Patterson Air Force Base, Ohio

DTIC QUALITY INSPECTED

19970214 029

**APPLICATION OF A
FINITE-VOLUME TIME-DOMAIN
MAXWELL EQUATION SOLVER
TO THREE-DIMENSIONAL OBJECTS**

THESIS

Frederick G. Harmon, Captain, USAF

AFIT/GE/ENG/96D-06

Approved for public release, distribution unlimited

The views expressed in this thesis are those of the author
and do not reflect the official policy or position of the
Department of Defense or the U.S. government

**APPLICATION OF A
FINITE-VOLUME TIME-DOMAIN
MAXWELL EQUATION SOLVER
TO THREE-DIMENSIONAL OBJECTS**

THESIS

Presented to the faculty of the Graduate School of Engineering
of the Air Force Institute of Technology
Air University in Partial Fulfillment of the
Requirements for the Degree of
Master of Science in Electrical Engineering

Frederick G. Harmon, B.S.E.E.
Captain, USAF

December, 1996

Approved for public release, distribution unlimited

Acknowledgments

I dedicate this thesis to my Lord and Savior, Jesus Christ, my wife, Marie, and my dog, Hannah. Jesus gave me the determination to complete this research and was faithful in answering prayer throughout the thesis effort. Marie, who completed her graduate education simultaneously with me, supported me throughout the thesis research and proofed the thesis drafts numerous times. As my best friend, she was understanding, helpful, and instrumental in the completion of the thesis. Hannah was patient during the many hours that I “ignored” her while I was on the computer. We have all completed this together and grown as a family.

For guidance, encouragement, and assistance, I want to thank my thesis advisor, Dr. Andrew Terzuoli, and the members of my thesis committee, Dr. William Baker, Major Tom Buter, and Major Gerald Gerace. Dr. Naishadham, from Wright State University, and Captain Doug Blake, a Ph.D. candidate at AFIT, also provided invaluable assistance.

Further, I want to thank my sponsors, Dr. J.S. Shang and Dr. Kueichien Hill, from Wright Laboratory. Their guidance and insight kept me focused on the work that needed to be accomplished. Dr. Hill was also very helpful in providing Moment Method results.

To my classmate, Jim Taylor, the AFIT experience has been tough but worthwhile and enjoyable. Thanks for the friendship and the memories.

Dr. Vijaya Shankar from Rockwell and Ken Wurztler from Wright Laboratory deserve recognition for generating the complicated grids. Also, this thesis research was supported in part by a grant of high performance computing (HPC) time from the DoD HPC Centers, CEWES (Cray 90) and Maui (SP-2). The personnel at these HPC centers generously provided computer support for the Cray 90 and SP-2 used throughout this research effort.

Frederick G. Harmon

Table of Contents

	Page
Acknowledgments	ii
Table of Contents	iii
List of Figures.....	vi
List of Tables.....	ix
List of Abbreviations and Variables.....	x
Abstract.....	xii
 1 Introduction	 1
1.1 Background	2
1.2 Problem Statement	4
1.3 Summary of Current Knowledge	5
1.4 Assumptions.....	7
1.5 Scope.....	7
1.6 Thesis Organization	8
 2 Literature Review	 9
2.1 Overview	9
2.2 Grid Generation of Finite-Volume Cells	9
2.3 Maxwell's Equations	10
2.4 Maxwell's Equations in Conservation Form	11
2.5 Coordinate Transformation.....	12
2.6 Finite-Volume Formulation	13
2.7 Boundary Conditions	14
2.8 Flux Evaluation and Time Integration	15
2.9 Green's-Function-Based Near-to-Far Field Transformation	16
2.10 Applications	17
2.11 Summary	18
 3 Methodology.....	 19
3.1 Overview	19
3.2 FVTD FORTRAN Code Modifications	21
3.2.1 Geometry: Ogive	21
3.2.2 Geometry: Cone-sphere.....	23
3.2.3 Grid Files.....	24
3.2.4 Grid Modifications	27

3.2.5 Direction and Polarization of the Incident Wave	28
3.2.6 Incident Wave Type	29
3.2.7 Scattered-Field Checks	32
3.2.8 Bistatic-to-Monostatic Approximation	33
3.3 FVTD Computational Issues	34
3.3.1 Scattered-Field Formulation	34
3.3.2 Stability	35
3.3.3 Numerical Dispersion	36
3.3.4 Transient Waves	36
3.3.5 Creeping Waves and Traveling Waves	37
3.3.6 Diffraction	37
3.4 Comparisons/Benchmarks	38
3.4.1 Method of Moments	38
3.4.2 Empirical Data	39
3.4.3 Error Calculations and Metrics	39
3.5 Computer Support	40
3.5.1 AFIT's Sparc 20	41
3.5.2 AFIT's DEC Alpha	41
3.5.3 CEWES HPCC's Cray 90	41
3.5.4 Maui HPCC's IBM SP-2	41
3.6 Summary	42
4 Applications, Results, and Comparisons	43
4.1 Overview	43
4.2 Ogive Electromagnetic Scattering Results	44
4.2.1 Ogive Bistatic RCS Results for 1.18 GHz, Sinusoid Incident Wave	48
4.2.2 Ogive Bistatic RCS Results for 1.18 GHz, Gaussian Pulse Incident Wave	56
4.2.3 Ogive Monostatic RCS Results for 1.18 GHz	58
4.2.4 Ogive Bistatic RCS Results for 9.0 GHz	61
4.2.5 Ogive Bistatic RCS Results for the Gaussian Pulse Incident Wave	63
4.3 Cone-Sphere Electromagnetic Scattering Results	74
4.3.1 Cone-sphere Bistatic RCS Results for 0.869 GHz, Sphere-Cap Incidence	77
4.3.2 Cone-Sphere Bistatic RCS Results for 0.869 GHz, Tip-On Incidence	81
4.3.3 Cone-sphere Monostatic RCS Results for 0.869 GHz	83
4.3.4 Cone-sphere Bistatic RCS Results for 3.0 GHz	85
4.4 Summary	87
5 Conclusions and Recommendations	89
5.1 Conclusions	89
5.1.1 Ogive RCS Results	90
5.1.2 Cone-Sphere RCS Results	92
5.1.3 FVTD Computational Issues	93
5.2 Suggested Areas for Further Research	95
5.2.1 Surface Boundary Condition	96
5.2.2 Radiation Boundary Condition	96
5.2.3 Material Interfaces	96
5.2.4 Dielectric Materials	97

5.2.5 Frequency-Dependent and Time-Dependent Materials	97
5.2.6 Anisotropic Materials.....	97
5.2.7 Multi-zoning for Complicated Objects	98
5.2.8 Hybrid Techniques	98
5.2.9 Multi-discipline Applications.....	98
5.2.10 Code Optimization	99
5.2.11 Summary.....	99
Appendix A: FVTD Formulation and Numerical Algorithm.....	100
A.1 Maxwell's Equations	100
A.2 Maxwell's Equations in Conservation Form	101
A.3 Coordinate Transformation.....	102
A.4 Finite-Volume Formulation	104
A.5 Eigenvalues and Eigenvectors	107
A.6 Flux Evaluation using a Local Orthogonal Coordinate System.....	110
A.7 Time Integration.....	112
A.8 Incident Wave	113
A.9 Boundary Conditions	114
A.9.1 Scatterer Surface Boundary Conditions	114
A.9.2 Radiation Boundary Condition.....	114
A.10 Fourier Transform.....	115
A.11 Near-to-Far Field Transformation.....	115
A.11.1 Surface Equivalence Theorem.....	116
A.11.2 Transformation	117
A.12 RCS Calculations	118
A.13 Summary	119
Appendix B: Finite-Volume Time-Domain FORTRAN Code	120
B.1 FVTD FORTRAN Code Outline	120
B.2 FVTD Code Listings of Modifications	122
B.2.1 Input File.....	122
B.2.2 Ogive Grid Modifications.....	128
B.2.3 Incident Field	132
B.2.4 RCS Convergence Check.....	135
B.2.5 Scattered-Field Threshold Check	138
B.2.6 Bistatic-to-Monostatic Approximation.....	140
B.3 Additional Codes.....	142
B.3.1 Error Calculations and Metrics.....	142
B.3.2 Scattered Electric Field Movie	144
B.4 FVTD FORTRAN Code	147
Bibliography	148
Vita	153

List of Figures

	Page
Figure 1: FVTD Thesis Research Block Diagram	19
Figure 2: Mesh Plot of EMCC-Defined Ogive.....	22
Figure 3: Mesh Plot of EMCC-Defined Cone-Sphere.....	23
Figure 4: Slice of the Ogive Grid (10-121-30) in the yz Plane	25
Figure 5: Slice of the Ogive Grid (10-121-30) in the xy Plane	25
Figure 6: Slice of the Cone-Sphere Grid (50-73-45) in the xz Plane	26
Figure 7: Slice of the Cone-Sphere Grid (50-73-45) in the xy Plane	26
Figure 8: Incident Wave Specification	28
Figure 9: Gaussian Pulses with Different Bandwidths.....	31
Figure 10: Frequency Spectrum of Gaussian Pulses Shown in Figure 9	31
Figure 11: Flowchart for RCS Convergence and Threshold Checks	32
Figure 12: Ogive Bistatic RCS, 1.18 GHz, VV, Number of Cells Varied in R Direction	49
Figure 13: Ogive Bistatic RCS, 1.18 GHz, VV, Number of Cells Varied in θ Direction.....	49
Figure 14: Ogive Bistatic RCS, 1.18 GHz, VV, Number of Cells Varied in ϕ Direction.....	50
Figure 15: Ogive Bistatic RCS, 1.18 GHz, VV, Fine (71-125-55) vs. Coarse (71-43-25) Grid .	51
Figure 16: Ogive Bistatic RCS, 1.18 GHz, VV, Difference Between FVTD and MoM RCS.....	51
Figure 17: Ogive Bistatic RCS, 1.18 GHz, VV, Cross-Correlation of FVTD and MoM RCS....	52
Figure 18: Ogive Bistatic RCS, 1.18 GHz, VV, Fourier Transform of FVTD and MoM RCS...	53
Figure 19: Ogive Bistatic RCS, 1.18 GHz, HH, Fine (71-125-55) vs. Coarse (71-43-25) Grid ..	54
Figure 20: Ogive Bistatic RCS, 1.18 GHz, HH.....	55
Figure 21: Ogive Bistatic RCS, 1.18 GHz, HH, Difference Between FVTD and MoM RCS.....	55

Figure 22: Ogive Bistatic RCS, 1.18 GHz, VV, Gaussian Pulse Incident Wave	57
Figure 23: Ogive Bistatic RCS, 1.18 GHz, HH, Gaussian Pulse Incident Wave	57
Figure 24: Ogive Monostatic RCS, 1.18 GHz, HH	59
Figure 25: Ogive Monostatic RCS, 1.18 GHz, HH, Error Between RCS Results	59
Figure 26: Ogive Monostatic RCS, 1.18 GHz, VV	60
Figure 27: Ogive Bistatic RCS, 9.0 GHz, HH	62
Figure 28: Ogive Bistatic RCS, 9.0 GHz, VV	62
Figure 29: Ogive Bistatic RCS, 1.0 GHz, HH, Gaussian Pulse vs. Sinusoid Incident Wave	65
Figure 30: Ogive Bistatic RCS, 1.0 GHz, VV, Gaussian Pulse vs. Sinusoid Incident Wave	65
Figure 31: Ogive Bistatic RCS, 2.0 GHz, HH, Gaussian Pulse vs. Sinusoid Incident Wave	66
Figure 32: Ogive Bistatic RCS, 2.0 GHz, VV, Gaussian Pulse vs. Sinusoid Incident Wave	66
Figure 33: Ogive Bistatic RCS, 3.0 GHz, HH, Gaussian Pulse vs. Sinusoid Incident Wave	68
Figure 34: Ogive Bistatic RCS, 3.0 GHz, VV, Gaussian Pulse vs. Sinusoid Incident Wave	68
Figure 35: Ogive Bistatic RCS, 4.0 GHz, HH, Gaussian Pulse vs. Sinusoid Incident Wave	70
Figure 36: Ogive Bistatic RCS, 4.0 GHz, HH, Difference Between RCS Results	70
Figure 37: Ogive Bistatic RCS, 4.0 GHz, HH, Cross-Correlation of FVTD and MoM RCS	71
Figure 38: Ogive Bistatic RCS, 4.0 GHz, VV, Gaussian Pulse vs. Sinusoid Incident Wave	72
Figure 39: Ogive Bistatic Results, 4.0 GHz, Electric Field Contour Plot	72
Figure 40: Cone-Sphere Bistatic RCS, 0.869 GHz, VV, Sphere-Cap Incidence, Coarse Grid	78
Figure 41: Cone-Sphere Bistatic RCS, 0.869 GHz, VV, Sphere-Cap Incidence, Fine Grid	78
Figure 42: Cone-Sphere Bistatic RCS, 0.869 GHz, VV, Difference Between RCS Results	80
Figure 43: Cone-Sphere Bistatic RCS, 0.869 GHz, VV, Cross-Correlation of RCS Data	80
Figure 44: Cone-Sphere Bistatic RCS, 0.869 GHz, HH, Sphere-Cap Incidence, Fine Grid	81
Figure 45: Cone-Sphere Bistatic RCS, 0.869 GHz, HH, Tip-On Incidence	82

Figure 46: Cone-Sphere Bistatic RCS, 0.869 GHz, VV, Tip-On Incidence	82
Figure 47: Cone-Sphere Monostatic RCS, 0.869 GHz, HH	83
Figure 48: Cone-Sphere Monostatic RCS, 0.869 GHz, VV	84
Figure 49: Cone-Sphere Bistatic RCS, 3.0 GHz, HH, Sphere-Cap Incidence	85
Figure 50: Cone-Sphere Bistatic RCS, 3.0 GHz, VV, Tip-On Incidence	86
Figure A.1: Finite-Volume Cell	106
Figure A.2: Virtual Surface and Far-Field Sketch	118
Figure B.1: FVTD.F Flowchart	121

List of Tables

	Page
Table 1: Ogive Test Matrix	44
Table 2: Stability and Time Data for the Ogive Tests.....	46
Table 3: Grid Point Densities for the Ogive Tests	47
Table 4: MSE and Comparisons for the Ogive Tests	73
Table 5: Cone-Sphere Test Matrix	75
Table 6: Stability and Time Data for the Cone-Sphere Tests	76
Table 7: Grid Point Densities for the Cone-Sphere Tests	76
Table 8: MSE and Comparisons for the Cone-Sphere Tests.....	87
Table B.1: Gaussian Pulse Parameters for a Specified Bandwidth.....	126

List of Abbreviations and Variables

BC	boundary condition
BOR	body-of-revolution
c	velocity of electromagnetic waves in free space (m/s)
CAD	computer-aided design
CEM	computational electromagnetics
CFD	computational fluid dynamics
CFL	Courant-Friedrichs-Lewy stability value
E	electric field strength vector (V/m)
E_θ, E_ϕ	components of the incident E field vector
D	electric flux density vector (C/m^2)
B	magnetic flux density vector (Wb/m^2 or Tesla)
EMCC	Electromagnetic Code Consortium
F, G, H	flux vectors
$\hat{F}, \hat{G}, \hat{H}$	flux vectors in transformed curvilinear coordinates
FDTD	finite-difference time-domain
FVTD	finite-volume time-domain
GPD	grid point density (cells/ λ)
GTD	geometrical theory of diffraction
H	magnetic field strength vector (A/m)
HH	polarization, transmit horizontal and receive horizontal
HPCC	high performance computing center
i, j, k	indices of a discretized finite-volume cell

\mathbf{k}	propagation vector of incident wave
\mathbf{J}	electric current density vector (A/m ²)
MoM	method of moments
MSE	mean-square error
MUSCL	monotone upstream-centered scheme for conservation laws
n	time index
PEC	perfect electric conductor
R, θ, ϕ	spherical coordinates
RAM	radar absorbing material
t	time variable (s)
\mathbf{U}	vector containing dependent variables, Cartesian components of \mathbf{B} and \mathbf{D}
UTD	uniform theory of diffraction
V	Jacobian of coordinate transformation, finite volume
VV	polarization, transmit vertical and receive vertical
x, y, z	Cartesian coordinates
ϵ	electric permittivity (F/m)
Λ	diagonal matrix containing the eigenvalues of the coefficient matrices
λ	wavelength (m)
μ	magnetic permeability (H/m)
ξ, η, ζ	general curvilinear coordinates
ρ	electric charge density (C/m ³)
σ	radar cross section (dBsm)
ω	radian frequency (rad/s)

Abstract

Concurrent engineering approaches for the disciplines of computational fluid dynamics (CFD) and electromagnetics (CEM) are necessary for designing future high-performance, low-observable aircraft. A characteristic-based finite-volume time-domain (FVTD) computational algorithm developed for CFD and herein applied to CEM is implemented to analyze the radar cross section (RCS) of two three-dimensional objects, the ogive and cone-sphere, by utilizing a scattered-field formulation of the time-dependent Maxwell equations. The FVTD formulation uses a van Leer's kappa scheme for the flux evaluation and a Runge-Kutta multi-stage scheme for the time integration. The RCS results are obtained from the electromagnetic fields subsequent to a Fourier transform and a near-to-far field transformation.

Developmental work for the thesis focused on modifying the original code to analyze scattering and obtain RCS data for closed-surface perfect electric conductor (PEC) 3-D objects using either a Gaussian pulse or sinusoid incident wave. Specification of the direction and polarization of the incident wave provides monostatic and bistatic results for various polarizations. A RCS convergence check, used with a sinusoid, ends the simulation after the transients diminish and the bistatic RCS values are within 0.1 dB of the RCS values calculated during the previous period. A threshold check, used with a Gaussian pulse, ends the simulation once the amplitude of the scattered field is 140 dB below the peak of the Gaussian pulse. A bistatic-to-monostatic RCS approximation saves computer run time by a factor of nearly 40.

The FVTD code and algorithm are validated for electromagnetic scattering problems by comparing FVTD code RCS results to data obtained from the Moment Method (MoM) code, CICERO, and empirical RCS data published by the Electromagnetic Code Consortium (EMCC). The FVTD RCS results for the ogive and cone-sphere are within 3.0 dB of the bistatic MoM results and 3.1 dB of the monostatic empirical RCS data. Accurate FVTD computations of diffraction, traveling waves, and creeping waves require a surface grid point density of 15-30 cells/ λ and a PEC boundary condition grid density of 200-400 cells/ λ , dependent on frequency.

APPLICATION OF A FINITE-VOLUME TIME-DOMAIN MAXWELL EQUATION SOLVER TO THREE-DIMENSIONAL OBJECTS

1 Introduction

When designing low-observable, high-performance military aircraft, engineers must consider both a low radar cross section (RCS) and excellent aerodynamic performance. However, an optimum electromagnetic design may not be an optimum aerodynamic design. The efficient design of future military aircraft requires concurrent multi-disciplinary approaches for the electromagnetic and fluid dynamic disciplines. One computational design tool, the finite-volume time-domain (FVTD) technique, can potentially consider optimum electromagnetic and aerodynamic designs concurrently, benefiting the design process of low-observable, high-performance aircraft [47]. Researchers have used FVTD successfully in the computational fluid dynamics (CFD) discipline since the early 1980's [48] to analyze the airflow about an aircraft, and recently, Shang, Shankar, Blake, Bishop, Huh, Noack, and others have applied the technique to the computational electromagnetics (CEM) discipline [5, 6-7, 15, 22, 29-47]. The application of the FVTD technique to the time-domain Maxwell equations of electromagnetics is relatively new compared to other CEM techniques but is proving to be successful.

FVTD requires application to complicated three-dimensional (3-D) benchmark objects for researchers to consider it a feasible computational tool for electromagnetic scattering

problems. In this thesis research, the comparison of FVTD scattering results for the three-dimensional objects, the ogive and cone-sphere, to Method of Moments (MoM) and empirical RCS data validates the FVTD technique in the area of electromagnetics. The MoM calculations, obtained from the code CICERO, and the empirical RCS data, published by the Electromagnetic Code Consortium (EMCC), serve as benchmarks for the FVTD RCS computations.

1.1 Background

FVTD is a logical choice for simulations in both computational fluid dynamics and computational electromagnetics. Fluid dynamics utilizes FVTD to solve the Euler equations by calculating the fluxes, such as energy or mass, through finite-volume cells of a discretized space [8]. The Maxwell equations, which model electromagnetic phenomena, are hyperbolic like the Euler equations; that is, both systems of partial differential equations have real eigenvalues (characteristic values). Their similar mathematical form permits the use of the same algorithm to numerically solve each set of equations. Thus, hyperbolic equation solvers developed for CFD, such as FVTD, can potentially be applied to Maxwell's equations of CEM.

In addition to multi-discipline applications, FVTD has other potential advantages including [18, 51]

- the direct solution of Maxwell's two curl partial differential equations
- the analysis of electromagnetic propagation through frequency-dependent, time-dependent, and anisotropic materials
- the ability to obtain multiple frequency results with a single simulation

Specifically, the direct solution of Maxwell's time-dependent equations is robust and potentially as accurate as the Method of Moments [18, 51]. The finite-difference time-domain (FDTD) technique, which also directly solves Maxwell's partial differential equations, provides highly

accurate simulations for free space electromagnetic scattering problems [51]. The Helmholtz equations, the time-harmonic wave equations derived from the Maxwell equations, are not used; therefore, the propagation of electromagnetic waves through frequency-dependent and time-dependent materials can be calculated. FVTD also permits the analysis of anisotropic materials, such as radar absorbing materials (RAM) found in filled honeycomb structures [42]. Additionally, the time-domain algorithm allows the solution of a problem for more than one frequency. Broadband incident waves, such as Gaussian pulses, can be used to obtain multiple frequency results.

The two most prominent FVTD researchers in the area of CEM are Dr. Vijaya Shankar of the Rockwell International Science Center [42-47] and Dr. Joe Shang of the Air Force's Wright Laboratory [29-41]. Both have written characteristic-based FVTD codes for analyzing the electromagnetic scattering from objects. The two codes differ in several significant areas: mathematical algorithm, order of accuracy, and capability. Shang has implemented a spatially third-order accurate algorithm and a temporal fourth-order accurate scheme in the FVTD code, while Shankar has implemented a second-order accurate algorithm. The higher-order accurate code can potentially reduce the required number of grid points per wavelength permitting the computation of the electromagnetic scattering from electrically larger objects and reducing the computer simulation time [36, 40]. The differences between the algorithms and the accuracy of the codes are discussed in more detail in Chapter 2.

The Rockwell FVTD code currently has more capability than the Wright Laboratory FVTD code. The Rockwell FVTD code has the ability to analyze the scattering from complicated objects and surfaces such as airfoils, inlets, and edges, while the Wright Lab FVTD code, prior to this research, was limited to calculating the scattering from a sphere [39, 41, 44, 46]. The Rockwell code can also calculate the electromagnetic scattering from layered dielectric

surfaces such as those found on low-observable aircraft. The Wright Lab FVTD requires modification to calculate the electromagnetic scattering from complicated 3-D objects and dielectric surfaces. After first modifying the Wright Lab FVTD code for this thesis research, an analysis of the electromagnetic scattering is performed for the complicated perfect electric conductor (PEC) objects: ogive and cone-sphere. The code has yet to be modified for dielectric surfaces.

1.2 Problem Statement

The objectives of this research are to

- modify the Wright Lab FVTD code to analyze the electromagnetic scattering from complicated perfect electric conductor (PEC) three-dimensional (3-D) objects
- validate the characteristic-based FVTD formulation by using the modified code to analyze the scattering from the 3-D objects, ogive and cone-sphere, and compare the FVTD RCS results to MoM results and empirical data published by the EMCC.

Prior to the thesis research, the Wright Lab FVTD code required modification to analyze the electromagnetic scattering from complicated three-dimensional objects such as an ogive and cone-sphere or other closed-surface, single-zone objects. The original FVTD code was limited to calculating the RCS from a sphere and required modification for closed-surface three-dimensional objects. A modification changing the spherical coordinate system dependency to a curvilinear grid system which is applicable for closed-surface objects permits the code to be applied to complicated 3-D geometries. Code modifications also include the ability to add grid points near tips of objects to ensure accuracy. The incident wave specification in the original FVTD code also required modification. The original code limited the specification of the incident wave to a sinusoid with one polarization and one direction of propagation.

Modifications permit an incident wave with options for specifying the direction, polarization, and type, either a sinusoid or broadband Gaussian pulse. The incident wave modifications permit the calculation of monostatic and bistatic RCS results for different polarizations. The Gaussian pulse provides scattering results for multiple frequencies with one simulation. A bistatic-to-monostatic approximation reduces computer simulation times for monostatic RCS calculations.

An analysis of the effectiveness of using FVTD to compute the electromagnetic scattering from complicated objects is a requirement before the Wright Lab FVTD code and algorithm can be considered a feasible computational design tool. The comparison of FVTD RCS calculations to a historically proven CEM method such as the Method of Moments and to empirical RCS data validates its capability and accuracy. This validation is completed for the EMCC-defined ogive and cone-sphere in this thesis research.

1.3 Summary of Current Knowledge

The FVTD formulation is characteristic-based. Chapter 2 gives an overview of the characteristic-based schemes used by different researchers. Dr. Shang's specific FVTD formulation and characteristic-based numerical algorithm are described in detail in Appendix A. Reportedly, the advantages of characteristic-based computational algorithms are [30]

- a naturally enforced well-posedness condition for specifying initial values
- a windward spatial discretization based on the direction of wave propagation
- a radiation boundary condition (BC) based on a compatibility condition

Specifically, the windward spatial discretization imitates the physics of the electromagnetic scattering. For instance, it imitates the direction of wave propagation. The sign of the eigenvalue corresponds to the direction of propagation. Forward differencing is used with the

negative eigenvalues and backward differencing with the positive eigenvalues. The compatibility condition minimizes erroneous numerical reflections from the outer boundary of the grid.

The process of applying the characteristic-based FVTD formulation to electromagnetics problems is sequential and follows a logical procedure. First, the physical space surrounding the object of interest, such as an aircraft, is discretized into finite-volume cells. The space grid refers to the computational space containing the cells [51]. The frequency of interest and the electrical length of the object determines the number of cells required in the space grid [47]. The finite truncated space of a computational domain will generate numerical reflections in the space and produce erroneous computations [37]. Radiation boundary conditions, such as the compatibility condition which sets the incoming flux component equal to zero, are implemented at the edges of the truncated space and reduce the numerical reflections in the grid space.

Second, for use in the FVTD algorithm, the time-domain Maxwell partial differential equations are placed in conservation form (See Chapter 2 or Appendix A) [47]. Maxwell's equations comprise a hyperbolic system of partial differential equations which can be solved using characteristic-based analysis. The Maxwell equations in conservation form are applied to every finite-volume cell in the grid and solved numerically in the spatial and temporal domains using one of several techniques. The spatial techniques, or flux evaluation methods, are broadly categorized as implicit or explicit (See Chapter 2) [37]. For the time integration, Maxwell's equations in FVTD form are integrated using one of several techniques.

For the implementation of the FVTD technique, the scattered-field formulation is used as opposed to the total-field formulation. Only the scattered electric and magnetic fields and not the total fields propagate through the space grid. The scattered-field formulation is implemented for a PEC object by setting the tangential electric field on the scatterer surface equal to the negative of the tangential incident field. The incident field never appears in the FVTD calculations.

Finally, the far-field RCS is computed. The scattered fields computed by FVTD give calculations in the near-field and in the time-domain. A Fourier transform permits frequency data to be obtained from the time-domain data. A Green's-function-based transformation allows the far-field RCS to be easily calculated from the near-field frequency data [51].

1.4 Assumptions

To modify the Wright Lab FVTD code for complicated objects, several assumptions were made. First, the radiation boundary condition, or compatibility condition, implemented by Shang was assumed to be sufficient. The compatibility condition sets the incoming flux component equal to zero. The boundary condition is only accurate if the scattered electromagnetic wave is parallel to one of the transformed coordinates [30, 38]. Numerical errors introduced because the propagating wave is not parallel to a coordinate axis were not addressed. The first-order surface boundary condition for a PEC surface was also assumed to be sufficient for the purposes of this thesis research.

Second, the mathematical algorithm used by Shang, van Leer's kappa scheme, was assumed to be the most adequate method for the flux evaluation in Maxwell's equations. Shang has studied numerous FVTD numerical techniques for solving Maxwell's equations and the current flux evaluation technique is assumed to be the most efficient and accurate [29-41].

1.5 Scope

The focus of this thesis research was to modify the Wright Lab FVTD code to compute the scattering from the ogive and cone-sphere and validate the FVTD code by comparing FVTD RCS results to MoM and empirical RCS data.

Perfect electric conductor (PEC) surfaces are used for the complicated three-dimensional objects. Dielectric surfaces were not studied; therefore, multi-zoning which requires generating different grids for each dielectric surface or layer, is not implemented in the FVTD code.

FVTD codes potentially require massive amounts of computational time and memory. Modifying the code for speed optimization or parallel computing was not emphasized because other researchers such as Blake are optimizing the code for parallel computing [6, 7].

1.6 Thesis Organization

With Chapter 1 serving as the basic foundation for FVTD and the research which needs to be completed in the area of CEM, Chapter 2 discusses the FVTD formulation and the numerical techniques used by various researchers such as Shang and Shankar to solve electromagnetic scattering problems. Chapter 3 discusses the methodology used in completing the research and the code modifications that were required to thoroughly analyze the scattering from the ogive and cone-sphere using FVTD. The FVTD RCS results for the ogive and cone-sphere using the modified Wright Lab FVTD code are presented in Chapter 4 along with a discussion of the results. Also in Chapter 4, FVTD results are compared to MoM results and empirical RCS data. Chapter 5 contains conclusions on the FVTD research and includes proposed areas of future FVTD research. The two appendices contain supplemental data on the FVTD formulation and code development. In Appendix A, the FVTD formulation and numerical algorithm implemented by Dr. Shang in the Wright Lab FVTD code are discussed. Appendix B contains code listings and descriptions of the FVTD code modifications.

2 Literature Review

2.1 Overview

The FVTD computational technique is capable of concurrently solving the Euler equations of fluid dynamics and the Maxwell equations of electromagnetics. CFD has used the FVTD technique since the early 1980's [48] to analyze the airflow about an aircraft or airfoil and the technique has recently been applied to CEM. Several engineers, Blake, Shang, Shankar, Bishop, Huh, and Noack, are exploring and advancing the application of the FVTD technique to the Maxwell equations of electromagnetics [5, 6-7, 15, 22, 29-41, 42-47].

The FVTD technique follows a logical procedure from grid generation and formulating the Maxwell equations in FVTD form to evaluating the fields or fluxes through each cell of the grid. The computed scattered-field results are then transformed from the near-field to the far-field. From the far-field calculations, RCS results are obtained. The following sections discuss the FVTD procedures for applying FVTD to electromagnetic scattering problems and the characteristic-based FVTD formulations and numerical algorithms implemented by Shang and Shankar. Appendix A describes in detail one specific formulation and numerical algorithm used by Shang and implemented in the FORTRAN code in this thesis research.

2.2 Grid Generation of Finite-Volume Cells

Computer simulations require that 3-D geometries in a physical space be accurately represented in a computational domain [47]. To use FVTD, the physical space surrounding an object of interest, such as the ogive and cone-sphere used in this thesis, must be discretized into volumetric cells. The space containing the finite-volume cells is referred to as the space grid

[51]. The frequency of interest and the electrical length of the object determines the number of cells in the grid [47]. The grid can take on several forms, either structured or unstructured.

A structured grid is defined by clearly distinguishable coordinate directions [7]. Simple shapes or surfaces which can align with the axes of the three-dimensional coordinate system use the structured grid. In contrast to the structured grid, an unstructured grid contains undefinable coordinate directions [7]. An advantage of the unstructured grid is its ability to conform the grid to the surfaces of irregular objects.

For characteristic-based FVTD formulations, a structured grid using curvilinear coordinates is used so the wave propagation is aligned closely with one of the coordinate axes [34]. The compatibility condition used for the radiation boundary condition is exact if the wave propagation parallels a coordinate axis. In addition, the curvilinear coordinates permit higher accuracy in the computation of the electric and magnetic scattered fields. The fields at the centers of the cells and the fluxes at the faces of the cell are calculated using the metrics of the cell and the curvilinear coordinates better represent the geometric features of the object resulting in higher accuracy of the scattered field computations.

2.3 Maxwell's Equations

The time-domain Maxwell equations, in differential form, are shown below and will be used in the development of the electromagnetic FVTD equations:

$$\text{Faraday's Law:} \quad \nabla \times \mathbf{E} = -\frac{\partial \mathbf{B}}{\partial t} \quad (1)$$

$$\text{Ampere's Law:} \quad \nabla \times \mathbf{H} = \frac{\partial \mathbf{D}}{\partial t} + \mathbf{J} \quad (2)$$

$$\text{Gauss's Electric Law:} \quad \nabla \cdot \mathbf{D} = \rho \quad (3)$$

$$\text{Conservation of Magnetic Charge:} \quad \nabla \cdot \mathbf{B} = 0 \quad (4)$$

where \mathbf{E} : Electric field strength vector (V/m)
 \mathbf{D} : Electric flux density vector (C/m²)
 \mathbf{H} : Magnetic field strength vector (A/m)
 \mathbf{B} : Magnetic flux density vector (Wb/m² or T)
 \mathbf{J} : Electric current density vector (A/m²)
 ρ : Electric charge density (C/m³)

The constitutive parameters relate the field strength vectors and the flux density vectors.

The constitutive parameters, the electric permittivity and the magnetic permeability, are normally expressed as tensors. However, if the material is linear and isotropic, the constitutive parameters are scalars and the constitutive relations become

$$\mathbf{D} = \epsilon \mathbf{E} \text{ and } \mathbf{B} = \mu \mathbf{H} \quad (5)$$

where ϵ : Electric permittivity (F/m)

μ : Magnetic permeability (H/m)

The four Maxwell equations are interdependent. The two divergence equations can be derived from the two curl equations using the conservation of charge relationship

$\nabla \cdot \mathbf{J} = -\partial \rho / \partial t$ assuming the material is linear and isotropic. The FVTD calculations do not use the two divergence equations, but the equations can be used as a check on the predicted field response [18].

2.4 Maxwell's Equations in Conservation Form

For use in FVTD, the two curl Maxwell equations are cast in conservation form [37].

The solution of Maxwell's equations do not require the conservation form; however, the form is required by the Euler equations to conserve physical properties such as energy, mass, and momentum [8]. The Maxwell equations are also cast in conservation form to take advantage of

the same computational technique used to solve the Euler equations. To place the two curl Maxwell equations in conservation form, the curl operations are carried out and the constitutive parameters are implemented. The result is given by [37]

$$\frac{\partial \mathbf{U}}{\partial t} + \frac{\partial \mathbf{F}}{\partial x} + \frac{\partial \mathbf{G}}{\partial y} + \frac{\partial \mathbf{H}}{\partial z} = -\mathbf{J} \quad (6)$$

where

$$\mathbf{U} = \begin{bmatrix} B_x \\ B_y \\ B_z \\ D_x \\ D_y \\ D_z \end{bmatrix} \quad \mathbf{F} = \begin{bmatrix} 0 \\ -D_z / \epsilon \\ D_y / \epsilon \\ 0 \\ B_z / \mu \\ -B_y / \mu \end{bmatrix} \quad \mathbf{G} = \begin{bmatrix} D_z / \epsilon \\ 0 \\ -D_x / \epsilon \\ -B_z / \mu \\ 0 \\ B_x / \mu \end{bmatrix} \quad \mathbf{H} = \begin{bmatrix} -D_y / \epsilon \\ D_x / \epsilon \\ 0 \\ B_y / \mu \\ -B_x / \mu \\ 0 \end{bmatrix} \quad \mathbf{J} = \begin{bmatrix} 0 \\ 0 \\ 0 \\ J_x \\ J_y \\ J_z \end{bmatrix}$$

Equation (6) is a system of six linear equations. \mathbf{U} is the independent variable and the \mathbf{F} , \mathbf{G} , and \mathbf{H} flux vectors are the dependent variables. The equations are not linearly independent; therefore, a characteristic-based technique is needed to uncouple the six equations.

2.5 Coordinate Transformation

To analyze the scattering of various objects, including the ogive and cone-sphere analyzed in this thesis, a curvilinear coordinate transformation is required [37]. A curvilinear structured grid minimizes the errors introduced in the cell metrics and the flux calculations. The order of accuracy will be below the formal order of accuracy if a poor curvilinear grid is generated [34]. The coordinate transformation converts the Cartesian coordinates to curvilinear coordinates. The transformation defines a one-to-one relationship between two sets of temporal and spatially dependent variables. The variables used are ξ , η , and ζ and are all functions of x , y , and z . Equation (6), after a coordinate transformation, becomes [37, 38]

$$\frac{\partial \hat{U}}{\partial t} + \frac{\partial \hat{F}}{\partial \xi} + \frac{\partial \hat{G}}{\partial \eta} + \frac{\partial \hat{H}}{\partial \zeta} = -\hat{J} \quad (7)$$

where $\hat{U} = \frac{U}{V}$

$$\hat{J} = \frac{J}{V}$$

$$\hat{F} = \left(\frac{\partial \xi}{\partial x} F + \frac{\partial \xi}{\partial y} G + \frac{\partial \xi}{\partial z} H \right) \frac{1}{V}$$

$$\hat{G} = \left(\frac{\partial \eta}{\partial x} F + \frac{\partial \eta}{\partial y} G + \frac{\partial \eta}{\partial z} H \right) \frac{1}{V}$$

$$\hat{H} = \left(\frac{\partial \zeta}{\partial x} F + \frac{\partial \zeta}{\partial y} G + \frac{\partial \zeta}{\partial z} H \right) \frac{1}{V}$$

V is the Jacobian of the coordinate transformation and is equal to [34]

$$V = \begin{vmatrix} \frac{\partial \xi}{\partial x} & \frac{\partial \xi}{\partial y} & \frac{\partial \xi}{\partial z} \\ \frac{\partial \eta}{\partial x} & \frac{\partial \eta}{\partial y} & \frac{\partial \eta}{\partial z} \\ \frac{\partial \zeta}{\partial x} & \frac{\partial \zeta}{\partial y} & \frac{\partial \zeta}{\partial z} \end{vmatrix} = \begin{vmatrix} \frac{\partial \xi}{\partial x} & \frac{\partial \eta}{\partial x} & \frac{\partial \zeta}{\partial x} \\ \frac{\partial \xi}{\partial y} & \frac{\partial \eta}{\partial y} & \frac{\partial \zeta}{\partial y} \\ \frac{\partial \xi}{\partial z} & \frac{\partial \eta}{\partial z} & \frac{\partial \zeta}{\partial z} \end{vmatrix} \quad (8)$$

A coordinate transformation closely aligns the direction of propagation of the scattered electric and magnetic fields to the coordinate directions [37]. The radiation boundary condition produces fewer numerical reflections if the coordinate axis closely parallels the direction of propagation of the scattered fields.

2.6 Finite-Volume Formulation

Equation (7) is applied to every finite-volume cell in the grid. An integration is performed over each finite-volume cell:

$$\iiint_V \frac{\partial \hat{U}}{\partial t} dV + \iiint_V \left(\frac{\partial \hat{F}}{\partial \xi} + \frac{\partial \hat{G}}{\partial \eta} + \frac{\partial \hat{H}}{\partial \zeta} \right) dV = - \iiint_V \hat{J} dV \quad (9)$$

The divergence theorem is then applied to the second integral:

$$\iiint_V \frac{\partial \hat{U}}{\partial t} dV + \oint_S (\hat{F} + \hat{G} + \hat{H}) \cdot \mathbf{n} dS = - \iiint_V \hat{J} dV \quad (10)$$

where \mathbf{n} : Unit vector normal to the surface (ξ , η , and ζ for \hat{F} , \hat{G} , and \hat{H} , respectively)

S : Closed surface bounding the finite volume (m^2)

Equation (10) is the expression for a generic FVTD formulation. The unknown components of the \hat{U} vector are the magnetic and electric flux densities. The vectors \hat{F} , \hat{G} , and \hat{H} are the flux vectors and can be expressed in terms of the magnetic and flux densities. A multitude of techniques are used to solve Equation (10) and differentiate the myriad of FVTD numerical algorithms.

2.7 Boundary Conditions

Realistically, radar waves scattered from an object travel away from the object and are not reflected back to the target. However, the truncated space of a computational domain will generate numerical reflections in the space and produce erroneous computations [45]. Implementing a radiation boundary condition (BC) reduces the numerical reflections in the grid space.

Shankar and Shang use a first-order accurate radiation BC [30, 45]. For precise calculations, first-order accuracy is not acceptable and higher-order BCs would ensure higher accuracy. Shang and Shankar use a compatibility condition in which the incoming flux component is set to zero at the boundary [37]. For the compatibility condition, the fields traveling perpendicular to the boundary are not reflected. For example, in the case of the

propagation of a wave from a dipole, the BC is exact since the wave travels along the radial coordinate direction. However, numerical errors can result if the wave is not traveling perpendicular to the boundary. The coordinate transformation discussed previously increases the component of the wave traveling perpendicular to the outer boundary [37].

A surface boundary condition is implemented on the surface of PEC scatterers. The BC sets the tangential electric field equal to zero and the normal component of the magnetic flux density equal to zero [7]. Details for the PEC BCs implemented for this thesis research can be found in Appendix A. Boundary conditions are also required for dielectric interfaces and details for these BCs can be found in the Shankar references [42-47].

2.8 Flux Evaluation and Time Integration

The flux vectors in Equation (10) can be evaluated numerically using one of several techniques which can be broadly categorized as explicit or implicit [30, 47]. Explicit numerical expressions place the independent and dependent variables on different sides of the equation. Implicit expressions are recognized by the intermixing of the dependent and independent variables on each side of the equation.

The techniques implemented by Shang and Shankar are explicit characteristic-based schemes. The objective of the characteristic-based numerical procedures is to achieve the Riemann approximation to a three-dimensional problem in each spatial dimension [30]. The three-dimensional Maxwell equations can then be solved in each dimension sequentially.

Shang has studied and applied several characteristic-based implicit and explicit techniques. He is presently using an explicit van Leer's kappa scheme in which the flux on a surface of a cell is extrapolated from data of adjacent cell centers [34]. The scheme is referred to as a Monotone Upstream-Centered Scheme for Conservation Laws (MUSCL) and is a

windward approach that considers the direction of wave propagation. The MUSCL approach produces various orders of accuracy. The approach used in this thesis research produces results which are third-order accurate. The details of van Leer's kappa scheme are discussed in Appendix A.

A flux-vector splitting algorithm developed by Steger and Warming [48] is used to calculate the fluxes from the independent variable \hat{U} . The incoming and outgoing electromagnetic waves are split based on the positive and negative sign of the characteristic, hence, the name split-flux vectors.

Shankar uses an explicit Lax-Wendroff upwind scheme that is characteristic-based. The scheme uses a predictor and a corrector step. The predictor step results in a first-order accurate solution. The corrector step increases the accuracy of the solution to second-order [42].

Equation (10), in the temporal or time-stepping domain, can be solved using several techniques, just as in the spatial domain. Shankar uses the same second-order Lax-Wendroff upwind scheme. Shang uses a Runge-Kutta family of single-step multi-stage procedures [32, 38] which gives varying degrees of accuracy. For example, with van Leer's kappa scheme for the flux evaluation, he uses either a two-stage or four-stage Runge-Kutta method that produces second-order accuracy and fourth-order accuracy, respectively [34].

The higher-order accurate Wright Lab code can potentially reduce the required number of grid points per wavelength permitting the computation of the electromagnetic scattering from electrically larger objects and reducing the computer simulation time [36, 40].

2.9 Green's-Function-Based Near-to-Far Field Transformation

The spatial and time integration of Equation (10) gives results in the near-field. Various calculations, such as the RCS, are far-field results. The FVTD grid is in the near field; however,

Green's-function-based transformations allow the scattered fields in the far-field to be easily calculated from the near-field results subsequent to a Fourier transform [51]. The near-to-far field transformation permits the FVTD grid to be truncated in the near-field and does not have to extend out to the far-field to obtain the RCS data.

The far-field results are obtained by creating a virtual surface around the object. This surface does not have to conform to the object. An imaginary surface in the FVTD grid space can serve as a virtual surface. The surface equivalence theorem is applied to the surface to obtain the equivalent time-harmonic electric and magnetic currents and charges. The currents and charges on the virtual surface are then weighted by a free-space Green's function to obtain the far-field \mathbf{E} and \mathbf{H} fields [51]. The far-field results, such as the RCS, are easily calculated from the far-field scattered \mathbf{E} and \mathbf{H} fields.

2.10 Applications

As mentioned previously, FVTD is relatively new to CEM. Shankar, Shang, Blake, and others have applied the FVTD codes to analyzing the electromagnetic scattering from various objects. Shankar has analyzed a two-dimensional PEC and dielectric circular cylinder [44]. Also in 2-D, Shankar has analyzed a simple engine inlet, ogive, and airfoil [44]. In addition, Shankar has completed extensive 3-D research in which he has analyzed a PEC sphere and missile. He has also worked with frequency-dependent materials [44]. Other applications can be found in Shankar's contract report [42].

Shang has used his various FVTD codes to analyze the scattering from a sphere, propagation from a dipole, and the propagation of a wave through a waveguide. Blake has rewritten Shang's FVTD vectorized code for parallel computing machines and has used his

modified code to study the propagation of an electromagnetic wave in a waveguide and the scattering from a single sphere and dual spheres [6, 7].

2.11 Summary

Computational techniques which permit simultaneous trade-offs between the electromagnetic and aerodynamic disciplines would greatly improve the efficiency of the engineering design process for low-observable aircraft. The FVTD computational technique is capable of solving the Euler equations of fluid dynamics and the Maxwell equations of electromagnetics. The FVTD technique, historically proven for fluid dynamics, has excellent potential in computational electromagnetics. Several engineers, such as Shang, Shankar, and Blake, are advancing the application of the FVTD technique to solving the Maxwell equations of electromagnetics.

The FVTD technique follows a logical process for calculating electromagnetic data for a scattering object. A curvilinear grid is generated about an object to ensure accurate results from the FVTD formulation. The Maxwell equations are placed in conservation form and then solved in the spatial and temporal domains using a technique dependent on the desired accuracy. Numerical reflections in the domain are reduced by implementing outer boundary conditions. Depending on the desired results, transformations can be applied to the computational results.

3 Methodology

3.1 Overview

For the thesis research, a disciplined approach was taken to modify the code and validate the FVTD formulation by studying the electromagnetic scattering from an ogive and cone-sphere. Figure 1 illustrates the basic approach used to complete the FVTD research. By performing several tasks concurrently, more research was completed successfully and efficiently. The columns in the block diagram correspond to the tasks which were performed in parallel and include the broad areas of FVTD code, comparisons/benchmarks, and computer support.

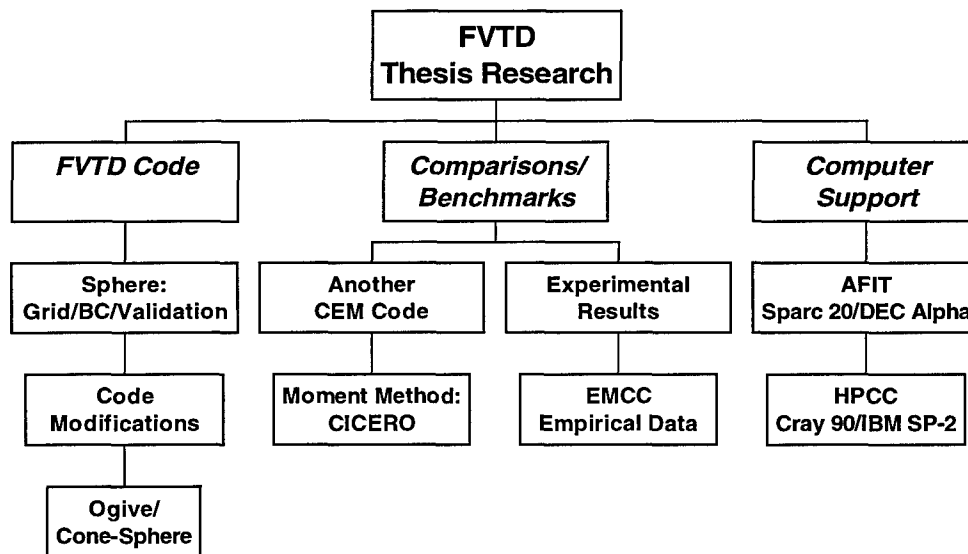


Figure 1: FVTD Thesis Research Block Diagram

The first task, FVTD code, was the focus of the thesis research. The FVTD code was first used to solve for the scattering of a PEC sphere to become familiar with the software, the FVTD formulation, grid generation, and boundary conditions. Analytical solutions for the

scattering of a sphere were used as benchmarks and for verifying code modifications to ensure accurate changes. Shang has published results for the sphere using the original FVTD code [38]. The reference includes comparisons to analytical solutions.

After becoming familiar with the code, it was modified to obtain electromagnetic scattering results from the PEC surfaces of an ogive and cone-sphere. The modified code can be used for other closed-surface perfect electric conductor (PEC) 3-D objects if an appropriate grid is generated. Appendix B contains the detailed requirements for the grid. The Rockwell International Science Center generated the grid for the ogive and the Flight Dynamics Directorate of Wright Labs generated the grid for the cone-sphere. In addition to modifying the code for a generic 3-D object, the option of specifying the direction, polarization, and type of the incident wave was programmed. Also programmed was an RCS convergence check used with a sinusoid incident wave which ends the simulation after the transients diminish. A threshold check, used with a Gaussian pulse incident wave, ends the simulation once the scattered field is below a pre-determined threshold. A bistatic-to-monostatic approximation saves computer simulation time for monostatic computations.

To complete the research, another CEM technique and experimental measurements were used as benchmarks. Column two in Figure 1 corresponds to the code and experimental results used as comparisons. The Method of Moments, considered as a very accurate CEM code, is used as a benchmark. The body-of-revolution Moment Method code, CICERO [55], was used to obtain bistatic and monostatic RCS results for the ogive and cone-sphere. Experimental measurements published by the Electromagnetic Code Consortium (EMCC) are benchmarks for the monostatic calculations [55]. The empirical results are excellent data to use as benchmarks and validate developmental CEM codes such as the FVTD code.

The third task, computer support, was critical in the completion of the research. The Air Force Institute of Technology (AFIT) machines, the SUN Sparc 20 and DEC Alpha machines, were used to assess code modifications. A Cray 90 at the USAE Waterways Experiment Station (CEWES) high performance computing center (HPCC) in Vicksburg, Mississippi was used to complete the majority of the computer simulations for the ogive. The SP-2 at the Maui HPCC in Maui, Hawaii, was used to complete the monostatic tests for the cone-sphere. The Cray 90 and SP-2 were invaluable in completing the research.

3.2 FVTD FORTRAN Code Modifications

The original FVTD FORTRAN code calculated the electromagnetic scattering from a sphere. The code modifications permit the calculation of the scattering from other closed-surface, single-zone, 3-D objects. The capability was added to read grid files generated by computer-aided design (CAD) software programs. Options for changing the size of the grid, such as the addition of grid points at diffraction points, were implemented to improve accuracy of the scattered-field computations. The original code specified the incident wave to propagate from only one direction with one polarization. The direction and type of incident wave was added along with an RCS convergence check and a threshold check for the scattered field. A bistatic-to-monostatic approximation obtains monostatic results from bistatic results. Appendix B contains the code and subroutines written for the code modifications and related functions.

3.2.1 Geometry: Ogive

The ogive is a very common test body for code validation and is a classic low-observable shaped body. The ogive is a body-of-revolution formed by rotating a convex arc around a chord [27]. No analytical solution for the electromagnetic scattering from an ogive is available;

therefore, MoM results and experimental data are used as benchmarks. The EMCC-defined ogive is 10 inches (0.254 m) long, has a maximum radius of 1 inch (0.0254 m), and a half-angle of 22.62 degrees [55]. The single ogive with a metallic surface is described mathematically as

$$f(z) = -\cos(22.62^\circ) + \sqrt{1 - \left(\frac{z}{5.0}\right)^2 \sin^2(22.62^\circ)} \quad (11)$$

$$x = \frac{f(z) \cos \Psi}{1 - \cos(22.62^\circ)} \quad (12)$$

$$y = \frac{f(z) \sin \Psi}{1 - \cos(22.62^\circ)} \quad (13)$$

for $-5.0 < z < 5.0$ inches

$-\pi < \Psi < \pi$ radians

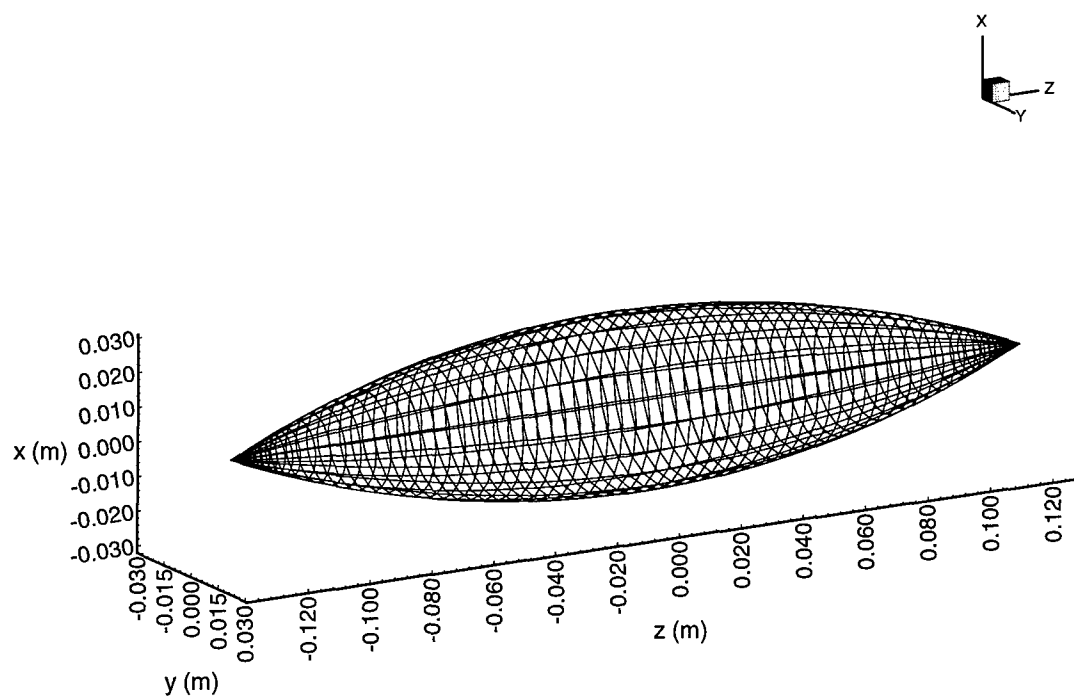


Figure 2: Mesh Plot of EMCC-Defined Ogive

Figure 2 is a mesh plot of the single ogive. Note that the ogive is approximately one wavelength long at 1.18 GHz [55]. The units in the plot are in meters.

3.2.2 Geometry: Cone-sphere

The cone-sphere is another common RCS test body which is also a body-of-revolution. The EMCC-defined cone-sphere has a half-angle of 7.0 degrees, radius of 2.947 inches (0.07485

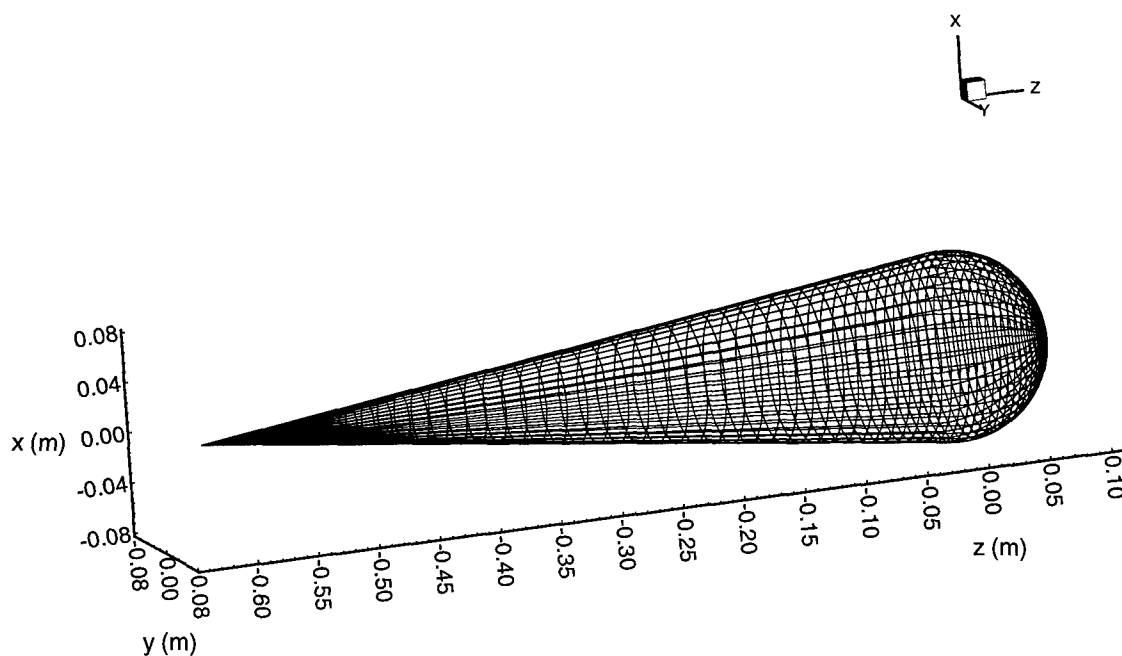


Figure 3: Mesh Plot of EMCC-Defined Cone-Sphere

m), and length of 27.127 inches (0.6890 m) [55]. The metallic surface of the cone portion of the cone-sphere is described mathematically as

$$x = 0.12279 \cos(\psi)(z + 23.821) \quad (14)$$

$$y = 0.12279 \sin(\psi)(z + 23.821) \quad (15)$$

for $-23.821 < z < 0.0$ inches

$$-\pi < \Psi < \pi \text{ radians}$$

The surface of the sphere portion of the cone-sphere is described mathematically as

$$x = 2.947 \cos(\psi) \sqrt{1 - \left(\frac{z - 0.359}{2.947} \right)^2} \quad (16)$$

$$y = 2.947 \sin(\psi) \sqrt{1 - \left(\frac{z - 0.359}{2.947} \right)^2} \quad (17)$$

for $0.0 < z < 3.306$ inches

$$-\pi < \Psi < \pi \text{ radians}$$

Figure 3 is a mesh plot of the cone-sphere. The cone-sphere is approximately two wavelengths long at 0.869 GHz [55]. The units in the plot are in meters.

3.2.3 Grid Files

A grid file for the ogive was obtained from NASA but was originally generated by the Rockwell International Science Center. Slices of the ogive grid are shown in Figures 4 and 5. The dimensions of the ogive equal the size of the EMCC-defined ogive. Figure 4 is a slice of the grid in the yz plane. The original grid size is (10-121-30) in spherical coordinates (R, θ, ϕ) . As seen, the radial lines of the grid are approximately perpendicular to the surface of the ogive. This characteristic will produce more accurate results from the first-order surface boundary condition (See Appendix A). The spacing of the cells in the radial direction also increases with an increase in R . The larger grid spacing with an increase in R minimizes the computer simulation time due to the fewer number of cells but retains the numerical accuracy of a finer grid near the surface.

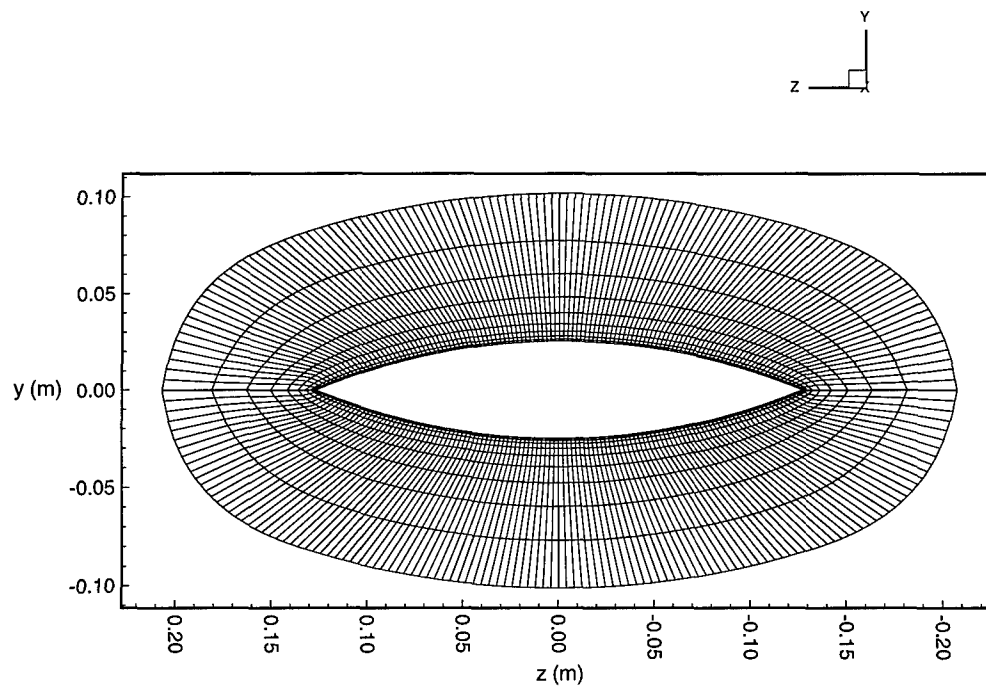


Figure 4: Slice of the Ogive Grid (10-121-30) in the yz Plane

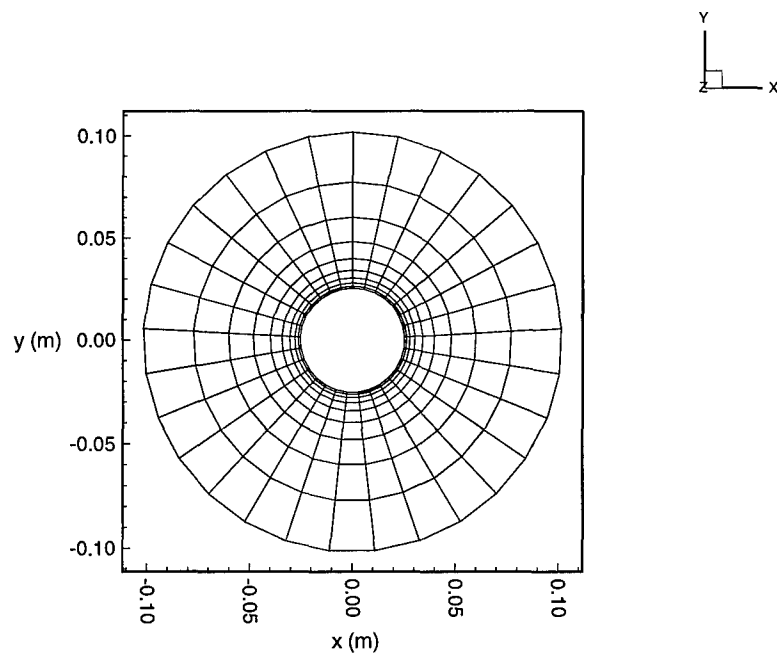


Figure 5: Slice of the Ogive Grid (10-121-30) in the xy Plane

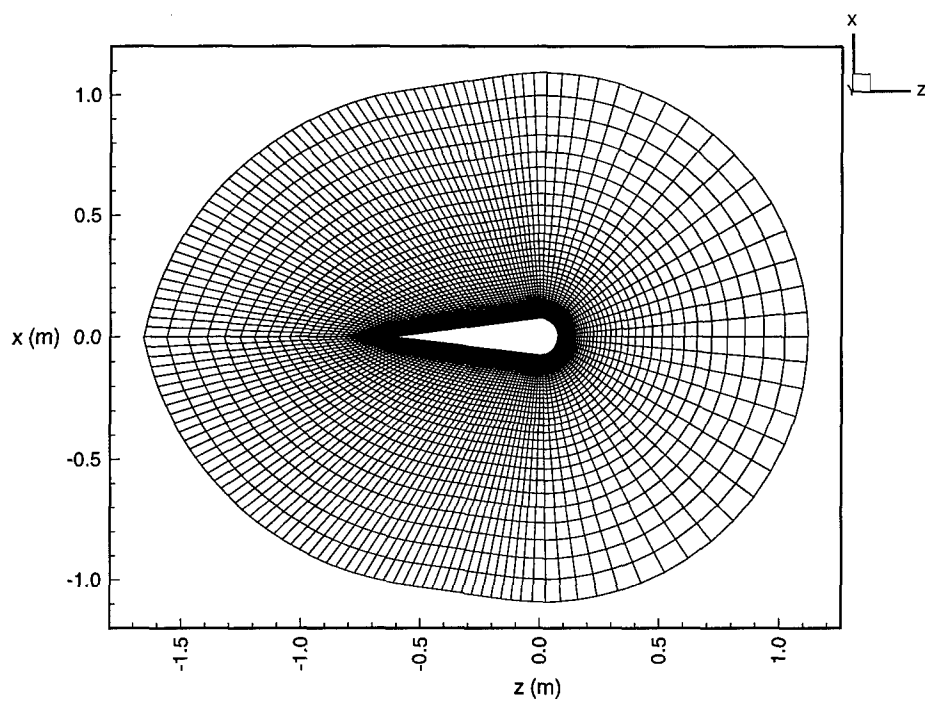


Figure 6: Slice of the Cone-Sphere Grid (50-73-45) in the xz Plane

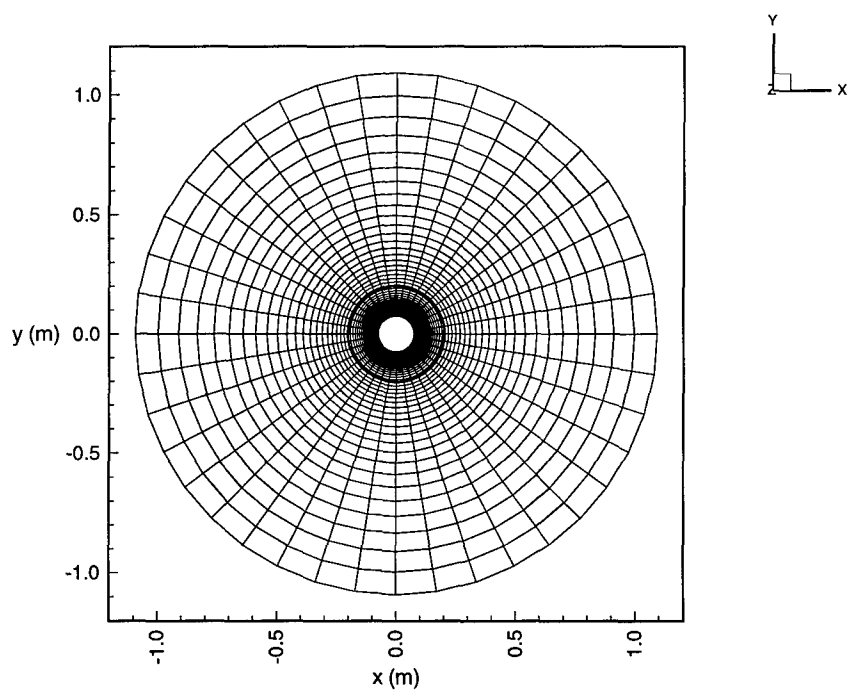


Figure 7: Slice of the Cone-Sphere Grid (50-73-45) in the xy Plane

The original cone-sphere grid was generated by the Flight Dynamics directorate of Wright Laboratory using GRIDGEN, a common CFD CAD package. The size of the original grid is (50-73-45) in spherical coordinates (R,θ,φ). The grid has the same characteristics as the ogive grid such as the increase in the spacing of the cells in the radial direction and tightly packed cells at the surface. A hyperbolic tangent distribution was used to generate the grid spacing in the radial direction. The radial lines are also approximately perpendicular to the surface, similar to the ogive grid. Slices of the cone-sphere grid are shown in Figures 6 and 7. Figure 6 is a slice of the grid in the xz plane and Figure 7 is a slice in the xy plane. The dimensions, in meters, of the cone-sphere match the size of the EMCC-defined cone-sphere.

3.2.4 Grid Modifications

Simple calculations included in the code change the size of the original grid, grid spacing, and the distance of the outer boundary from the scatterer. For the ogive and cone-sphere grids, the number of grid points in the phi direction are changed by finding the length of the radial. Then the desired spacing is calculated and (x, y) coordinates are generated based on the same radial distance, desired spacing, and number of grid points.

For each grid, to change the number of grid points in the radial direction and distance to the outer boundary, the following method is used:

$$R = (1 - \alpha)R_o + \alpha R_i \quad (18)$$

where R: Distance to the new coordinate
 R_o : Distance to outer radial coordinate at the edge of grid
 R_i : Distance to inner radial coordinate at the surface of the scatterer
 α : Scaling factor or increment

The sizes and densities of the grids were changed to analyze the effects of grid size and the number of grid points per wavelength. Grid points are added by averaging the grid coordinates of the surrounding points. Grid points can also be removed. A listing of the code containing the methods for changing the grid sizes for the ogive and cone-sphere is given in Appendix B.

3.2.5 Direction and Polarization of the Incident Wave

The incident wave's direction of propagation and polarization are specified as shown in Figure 8. The direction of the incident wave, \mathbf{r} , is specified by the spherical coordinates, θ and ϕ .

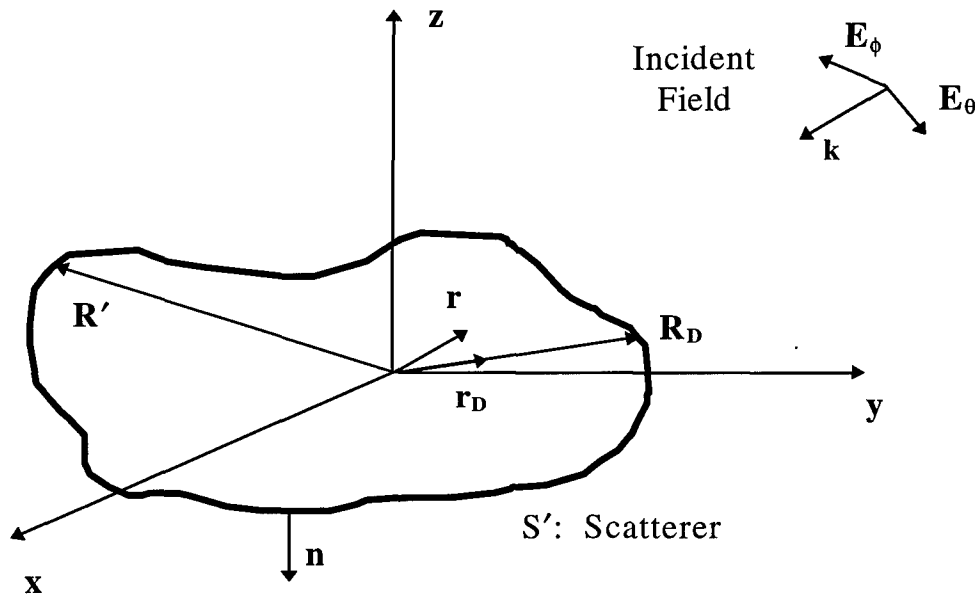


Figure 8: Incident Wave Specification

The direction is specified using the angle from which the incident field is propagating. This angle should not be confused with the angle of the propagation vector, \mathbf{k} . The polarization is specified with E_θ and E_ϕ [18]. The magnitude of the polarization components is unity and the

amplitude of the wave is specified separately. The displacement unit vector, \mathbf{r}_D , is used to define the relative spatial delay for each component of the incident field. The vector, \mathbf{R}' , is used to calculate the value of the incident field at each location on the surface of the scatterer. Appendix B contains more details on specifying the incident field.

3.2.6 Incident Wave Type

3.2.6.1 Sinusoid

The sinusoid incident wave, $\sin(\omega(t+(\mathbf{R}' \cdot \mathbf{r}_D)/c))$, is specified easily at one frequency. The sinusoidal wave provides bistatic RCS results for one frequency. At the beginning of each time step for the scattered-field formulation, the tangential scattered electric field is specified as the negative of the sinusoid at the scatterer surface. The amplitude of the sinusoid at one time step will depend on the location of the grid point on the surface. The spatial delay is found by taking the dot product of \mathbf{R}' and the displacement unit vector, \mathbf{r}_D . The initial application of the sinusoidal wave at the surface generates transients which must attenuate before accurate frequency data can be obtained. The time for the transients to die out is discussed in Chapter 4. The frequency data for the near-to-field transformation are taken after the transients diminish.

3.2.6.2 Gaussian Pulse

An advantage of the time-domain analysis is the capability to obtain multiple frequency results simultaneously. A Gaussian pulse is ideal to use as an incident wave for multiple frequency analysis. The Gaussian pulse is specified as [18]

$$g(t) = \exp \left[- \left(\frac{t + (\mathbf{R}' \cdot \mathbf{r}_D) / c - t_D - t_0}{T} \right)^2 \right] \quad (19)$$

where c : Velocity of the incident wave in free space

$g(t)$: Gaussian pulse with an amplitude of unity

t_0 : Center of Gaussian pulse, mean

t_D : Delay of Gaussian pulse due to maximum spatial delay in the direction of the incident wave ($|\mathbf{R}_D|/c$)

T : Duration of the Gaussian pulse

The parameters, T and t_0 , of the Gaussian pulse can be specified to obtain accurate results for a desired bandwidth of frequencies [18]. T is the duration of the pulse. The parameter t_0 determines the delay of the center of the pulse and the amplitude of the pulse at truncation. The pulses used for the thesis research are truncated 140 dB from the peak of the pulse [18]. The location of the truncation point is approximately 5.7 standard deviations from the center of the pulse. Two Gaussian pulses are illustrated in Figure 9. The wider pulse has a duration of 0.1278 nsec, delay of 0.5111 nsec, and a bandwidth (BW) of 10 GHz. The narrower pulse has a width of 0.07099 nsec, delay of 0.2840 nsec, and a BW of 18 GHz. The frequency spectra of the same pulses are shown in Figure 10. The useful range of frequencies is taken to be roughly one-third of the bandwidth shown [18]. As seen in Figure 10, sufficient amplitude is available for that range of frequencies. Appendix B contains a reference for specifying the parameters for a Gaussian pulse incident wave.

The use of either a Gaussian pulse or a sinusoid wave for the incident field is dependent on the results desired. The simulation for a Gaussian pulse is usually longer due to the time that it takes the pulse to travel through the computational space and for the scattered field to diminish. Therefore, the Gaussian pulse is advantageous only if the time required for the simulation is less than the total time required to complete tests for individual sinusoid cases.

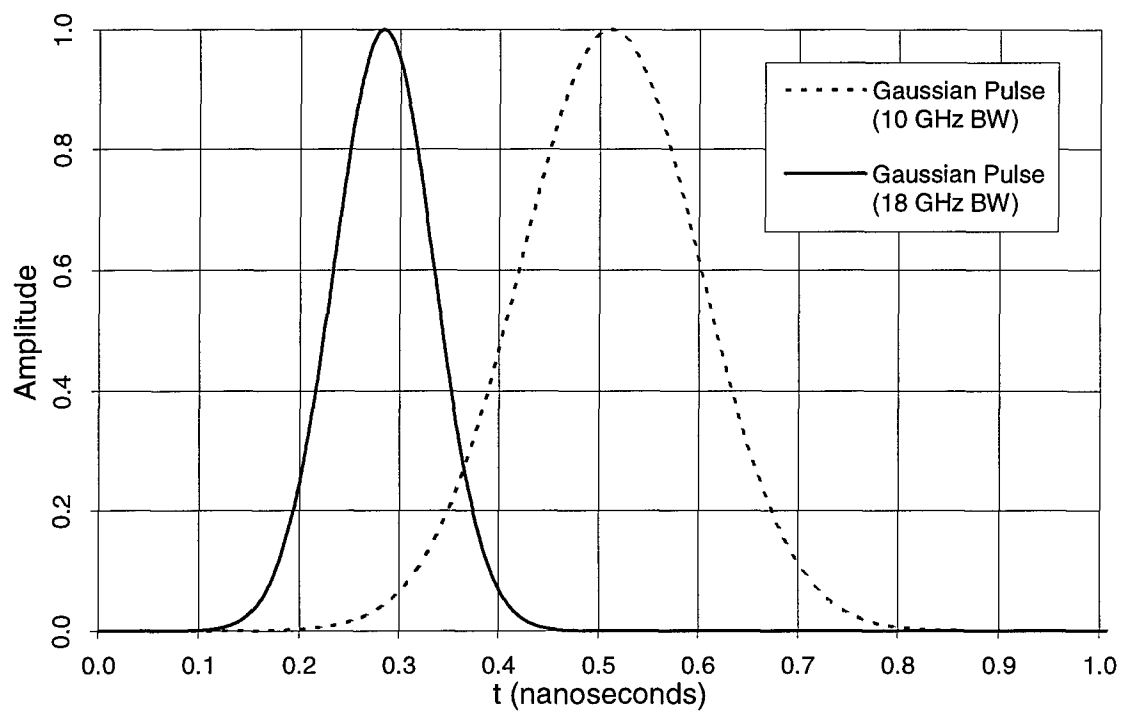


Figure 9: Gaussian Pulses with Different Bandwidths

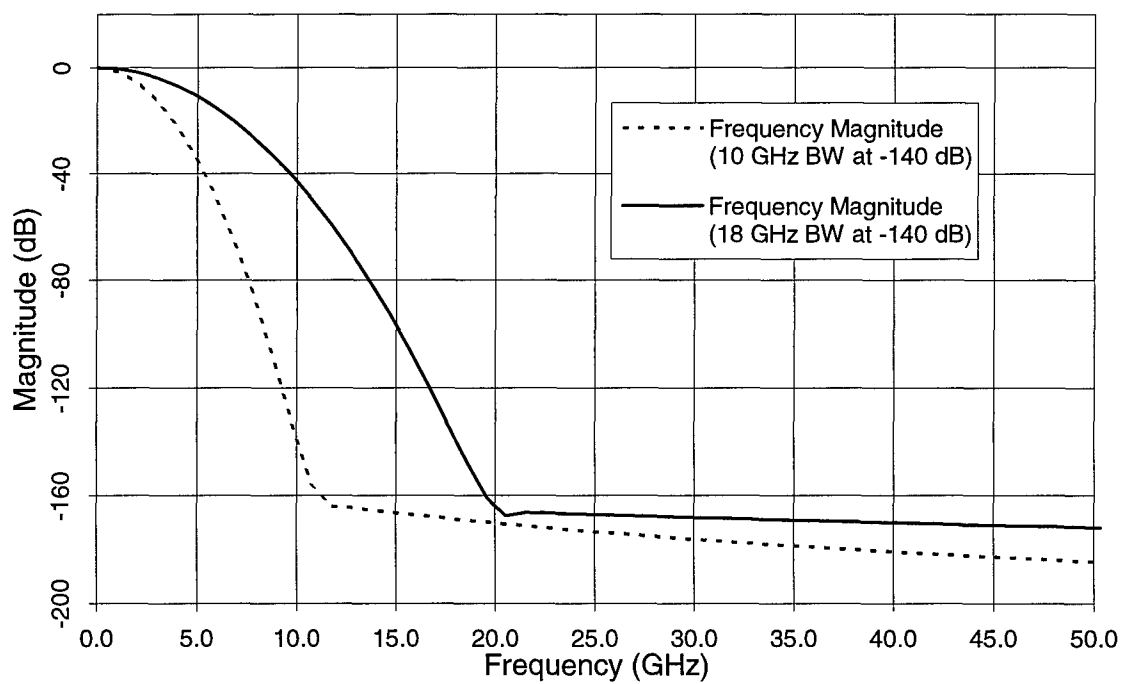


Figure 10: Frequency Spectrum of Gaussian Pulses Shown in Figure 9

3.2.7 Scattered-Field Checks

Figure 11 shows the decision flowchart for the scattered-field checks added to the FVTD code. The checks ensure that accurate frequency data is taken before the simulation ends. The checks occur at the end of a time step or a period. If the checks result in a “Yes,” the simulation ends and the RCS values are calculated. If the result is “No”, the time loop is entered again to calculate the fluxes for another time step. If the checks are not enabled, the Fourier transform parameters included in the input file end the simulation (See Appendix B).

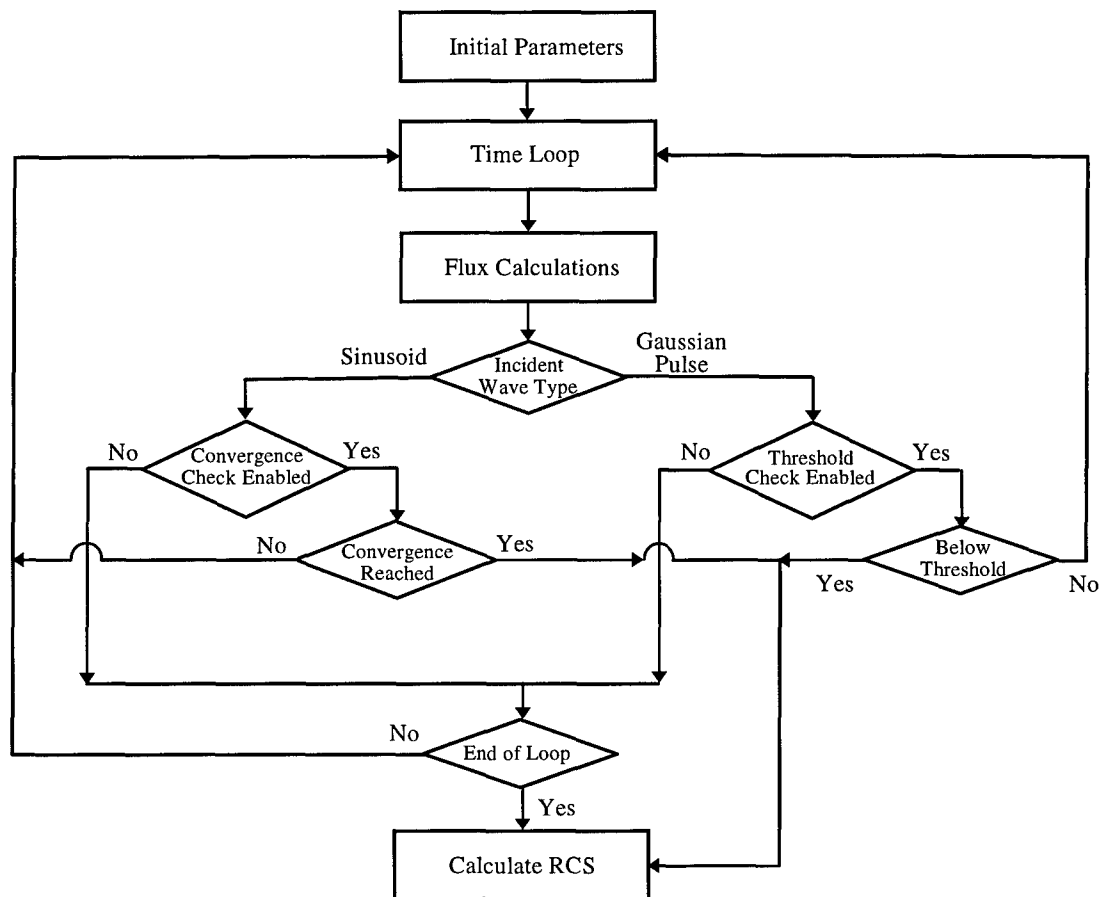


Figure 11: Flowchart for RCS Convergence and Threshold Checks

3.2.7.1 RCS Convergence

When initially specified, the sinusoid incident wave generates transients that must die out before accurate results can be obtained. To ensure convergence for the RCS values when a sinusoidal incident wave is implemented, a convergence check was programmed in the code. The check calculates the RCS value at ten different viewing angles. If the RCS values are within 0.1 dB of the RCS values from the previous time step, convergence has been reached. The bistatic RCS values are calculated from the frequency data taken for one period after convergence. Appendix B contains the code listing for the RCS convergence check.

3.2.7.2 Threshold Check

A threshold check for the scattered field resulting from a Gaussian pulse incident wave was added to the code. The check ends the simulation if the amplitude of the scattered field is less than 140 dB of the maximum amplitude of the incident wave. The check is performed by sampling the scattered field one cell away from the scatterer surface. The virtual surface which is used to calculate equivalent currents and the far-field RCS results is also located one cell away from the target surface. Sampling scattered-field amplitudes on the virtual surface ensures that the frequency data is accurate for the RCS calculations.

3.2.8 Bistatic-to-Monostatic Approximation

One simulation of the FVTD code gives bistatic data at 721 receiving locations. The angles are spaced 0.25° degrees apart, providing a 180° sweep of bistatic RCS values. A monostatic calculation is obtained for only one location. To obtain monostatic results for the entire 180° sweep, a monostatic FVTD test must be performed for every viewing location which would require 721 computer simulations. Obviously, this would require an enormous amount of

computer time and effort. A bistatic-to-monostatic approximation provides the entire monostatic sweep and decreases the number of monostatic tests required [28].

The bistatic-to-monostatic approximation is expressed as

$$RCS_M(0.5 \cdot \alpha) = RCS_B(\alpha) \quad (20)$$

where RCS_B : Calculated bistatic RCS value

RCS_M : Approximate monostatic RCS value

α : Angle at which bistatic value is calculated

The approximation originated when researchers at RCS test ranges observed that experimental monostatic RCS values are equal to bistatic values at twice the receiving angle [28]. The angle must be small, usually less than or equal to 5° .

The monostatic calculations in Chapter 4 are obtained by performing monostatic simulations every 10° . The bistatic-to-monostatic approximation uses the bistatic data at angles on each side of the incident angle to obtain the monostatic data. For example, the bistatic data from 0.50° to 10° is used to calculate the monostatic data from 0.25° to 5° . As will be seen in the monostatic plots, the approximation is sufficient for obtaining reasonable RCS results.

3.3 FVTD Computational Issues

3.3.1 Scattered-Field Formulation

The FVTD code uses a scattered-field formulation in which only the scattered field propagates through the computational space. The scattered-field formulation, as opposed to the total-field/scattered field formulation, avoids the numerical dispersion and dissipation of the incident wave as it propagates through the grid [52]. Also, the scattered field is analytically specified at the scatterer surface. A disadvantage of the scattered-field formulation is that it

requires the calculation of the scattered field at every time step at every point on the surface of the scatterer.

The scattered-field formulation is implemented for a PEC object by specifying the scattered tangential electric field as the negative of the incident field at the surface. The total tangential electric field is zero at the surface of the PEC object: $E^T = E^i + E^s = 0$. Therefore, the tangential scattered electric field is equal to the negative of the incident electric field at the surface: $E^s = -E^i$.

The scattered field is specified at the boundary of the scatterer. Because of the unknown electric and magnetic fields required at the scatterer surface for the FVTD formulation, an extrapolated boundary condition is used for the magnetic field. See Appendix A for the details on the extrapolated boundary condition.

3.3.2 Stability

The stability of the explicit FVTD formulation is based on the relationship between the spatial discretization and the time step. The time step is directly proportional to the smallest grid spacing and is inversely proportional to the wave velocity. The Courant-Friedrichs-Lewy (CFL) number determines the stability of the algorithm [38]. For example, for a three-dimensional problem, the CFL number has a maximum of 1.74. The stability condition is [51]

$$\Delta t \leq \frac{\text{CFL} / c}{\sqrt{\frac{1}{(\Delta x)^2} + \frac{1}{(\Delta y)^2} + \frac{1}{(\Delta z)^2}}} \quad (21)$$

where CFL: Courant-Friedrichs-Lewy number

Δt : Time step

$\Delta x, \Delta y, \Delta z$: Spatial increments

The stability of a system is also related to the eigenvalues of the system of equations. An advantage of the characteristic-based formulation is that it addresses the fundamental issues of well-posedness and numerical stability of a system of hyperbolic differential equations.

Several disadvantages of the explicit FVTD formulation are due to the stability criteria. First, surface characteristics such as tips and edges produce converging grid lines resulting in extremely small cells. The small cell sizes result in a very small time step which increases simulation times. Also, for higher frequencies, the wavelength decreases and the grid spacing decreases to maintain the same number of cells/ λ increasing the computation time.

3.3.3 Numerical Dispersion

The discretized space causes unwanted dispersion of the scattered field. Numerical dispersion varies with the direction of propagation, frequency, and variation of the cell size [52]. The amount of dispersion increases as the electrical size of the object increases. To minimize the effects of the numerical dispersion on the RCS results, the virtual surface used for calculating equivalent currents is located close to the scatterer, usually one cell away from the surface.

3.3.4 Transient Waves

Several issues arise with the use of either a sinusoid or Gaussian incident wave. The introduction of the sinusoid wave at the surface of the scatterer produces transient waves in the computational space. The frequency data for the RCS calculations cannot be taken until the transients diminish. The electrical size of the target determines the time required for the transients to diminish. Taflov reports that the minimum time is four times the longest electrical length of the object [52]. The required time may be shorter or longer, as will be seen in Chapter 4, to obtain converged solutions.

3.3.5 Creeping Waves and Traveling Waves

Creeping waves and traveling waves are electromagnetic phenomena that can significantly affect the RCS results. Knott defines creeping waves as the phenomenon associated with smooth bodies such as a sphere or cylinder which are not large with respect to λ . The wave is launched at the shadow boundary and travels around on the shadow side of the object and emerges at the other shadow boundary [17]. Because the amplitude of the creeping wave attenuates exponentially, creeping waves are usually negligible for bodies which are larger than 7λ [27]. Since the cone-sphere and ogive bodies used for this thesis research are less than 7λ , creeping waves contribute to the scattering results [17].

Surface traveling waves are an electromagnetic phenomenon similar to creeping waves except the wave is launched along smooth surfaces when the grazing incidence is small. The traveling wave occurs on the “illuminated” side of the object, as opposed to the creeping wave which occurs on the shadow side of an object. The E field must be parallel to the surface and a surface discontinuity must exist to reflect the wave back along the surface.

FVTD will accurately calculate creeping and surface traveling waves if the grid is correctly generated and the grid density at the surface is relatively high. The waves travel close to the surface, and thus, the grid must be dense to accurately predict the propagation of waves near the surface. The exact grid density required will be discussed in more detail in Chapter 4.

3.3.6 Diffraction

The correct prediction of diffraction, another electromagnetic phenomenon, is critical for the accurate calculation of scattering results. Diffraction occurs at the tips or edges of an object. The grid requirements for correctly predicting diffraction are similar to the grid requirements for creeping and traveling waves. The requirements for the grid will be discussed in Chapter 4.

The terms, traveling waves, creeping waves, and diffraction, originated with the use of high frequency techniques which do not necessarily account for these interactions. The terms refer to electromagnetic phenomena that have to be accounted for by using other methods or correction terms. FVTD's direct solution of Maxwell's equations account for all of these phenomena because the wave physics and interactions are inherent in the governing equations. The traditional high frequency terms are used in the discussion to easily refer to the phenomena.

3.4 Comparisons/Benchmarks

3.4.1 Method of Moments

Analytical solutions do not exist for objects such as the ogive and cone-sphere. A low frequency CEM method commonly used for validation purposes is the Method of Moments (MoM). The accuracy of the MoM permits it to be used for validation. The MoM requires the surface of the PEC scatterer to be discretized; whereas, for FVTD, a volume discretization is required.

The MoM solves for the equivalent current density induced on the surface of the scatterer. The method produces a system of linear equations which can be written in matrix form as

$$\mathbf{V} = \mathbf{Z} \cdot \mathbf{I} \quad (22)$$

where \mathbf{I} : Current Vector

\mathbf{V} : Voltage Vector

\mathbf{Z} : Impedance Matrix

The known variables are the voltage vector and the entries of the impedance matrix. The current vector is the unknown; therefore, the left-hand inverse of \mathbf{Z} is required to solve for \mathbf{I} . The \mathbf{Z}

matrix is usually dense and can become very large for electrically large objects, limiting the size of the scatterer that can be studied. The inversion of the \mathbf{Z} matrix required to solve for the equivalent currents can be computationally extensive limiting the size of the usable matrix [51]. The traditional radiation integral uses the equivalent currents to calculate the scattered fields.

3.4.2 Empirical Data

The EMCC has published empirical results for the ogive and cone-sphere discussed previously. The FVTD computational results are compared to the monostatic RCS experimental data. The Volakis reference contains the details on the measurement methods for the validation objects [55].

3.4.3 Error Calculations and Metrics

The FVTD results are compared to MoM and empirical RCS data. Metrics are established to compare the FVTD results to MoM results and empirical results. Only theoretical solutions are known for a few simple shapes such as the sphere. The MoM code results and the empirical data for the ogive and cone-sphere will not be considered “exact,” but as very accurate RCS results which can be used as benchmarks.

Four methods are used to analytically determine the difference between the FVTD and MoM or empirical results. The various methods include the

- difference, in dB, after considering phase by calculating the minimum error between the FVTD RCS result at one angle and several surrounding (± 5 degrees) MoM RCS results
- Mean-Square Error (MSE) using FVTD and MoM results (square meters). The phase is taken into account in the same way as for the previous method

- Cross-Correlation between FVTD and MoM results (square meters)
- FFT of the FVTD and MoM results (square meters)

The first two methods are common ways to calculate the difference or error. As will be seen in several plots in Chapter 4, a small phase shift of one or two degrees will result in a greater error if the phase shift is not considered. The phase shift is considered for the first two methods by calculating the minimum difference between the FVTD RCS result at one point and the MoM RCS result at surrounding points (± 5 degrees). The expression for the MSE is

$$\text{MSE} = \frac{1}{N} \sum_{n=1}^N (x_f - x_m)^2 \quad (23)$$

where x_f : FVTD RCS value at a bistatic or monostatic angle

x_m : MoM RCS value at a bistatic or monostatic angle

The last two methods are mathematically more rigorous techniques to compare the FVTD and MoM results. The cross-correlation gives the similarity between two plots and locates the point of maximum correlation. The absolute value of the Fourier Transform eliminates the phase shift by transforming the data (in degrees) to a non-physical quantity in units of 1/degrees. A MATLAB program which calculates the difference in dB, MSE, and the data for the cross-correlation and Fourier transform plots is listed in Appendix B.

3.5 Computer Support

The FVTD code, written in FORTRAN 77, was run on Air Force Institute of Technology (AFIT) machines, such as the SUN Sparc 20 and Digital Electric Corporation (DEC) Alpha, to obtain familiarization with the code. After modifications were made to the code, accounts were created on high performance supercomputers managed by high performance computing centers (HPCC).

3.5.1 AFIT's Sparc 20

AFIT's Sparc 20s use the UNIX operating system. The Sparcs were useful for short FVTD tests because of the relatively quick turn around time and accessibility. For tests requiring longer simulation times and more memory, other computing machines were more useful.

3.5.2 AFIT's DEC Alpha

The Digital Electric Corporation (DEC) Alpha machines use an AXP central processing unit (CPU). The CPU uses a 21064 chip, a 64-bit reduced instruction set chip (RISC) processor, which operates at 190 MHz. The DEC Alpha machines utilize the OpenVMS version 6.2 operating system. The DEC Alpha machines were useful for short tests for the 3-D objects.

3.5.3 CEWES HPCC's Cray 90

The Cray 90, located at USAE Waterways Experiment Station (CEWES) HPCC in Vicksburg, Mississippi, is a 16 processor high performance vector machine. The Cray 90, or C90, uses the UNICOS 9.0 operating system. The peak performance for each processor is one GigaFlop. The FVTD code, optimized for a vector machine, has a faster run time on the Cray 90 than any other computing machine.

3.5.4 Maui HPCC's IBM SP-2

The IBM SP-2 is a scalable parallel machine with 400 RS/6000 processors which operate at 66.7 MHz each. The SP-2 is a high performance computing machine with a peak throughput of 266 Mflops per processor. The IBM SP-2 used in this thesis research is located in Maui, Hawaii, at the Maui HPC. Although the FVTD code is optimized for a vector machine, shorter simulations were completed on one processor of the parallel SP-2 machine.

3.6 Summary

The successful code modifications permit the analysis of the electromagnetic scattering from an ogive and cone-sphere. The modified code can be applied to other closed-surface perfect electric conductor (PEC) 3-D objects if an appropriate grid is generated. In addition to modifying the code for a generic 3-D object, the option of specifying the direction and polarization of the incident wave was programmed. Other options, such as convergence checks, ensure accurate RCS data is computed.

In the next chapter, the options programmed into the code are used to perform computer simulations for the ogive and cone-sphere for different grid sizes, frequencies, types of incident waves, etc. The option added to specify the direction and polarization of the incident wave permits the completion of monostatic tests. The monostatic results are compared to MoM and empirical data. The different computational issues discussed in this chapter serve as a foundation for explaining the results and the differences between the FVTD and MoM or empirical RCS data. The ogive and cone-sphere RCS results in the next chapter validate the FVTD code and algorithm for CEM.

4 Applications, Results, and Comparisons

4.1 Overview

The electromagnetic scattering and RCS results for the EMCC-defined RCS test bodies ogive and cone-sphere are presented in this chapter. Bistatic and monostatic RCS results are presented for each PEC test body. The bistatic results are compared to MoM results and the monostatic results are compared to empirical data and MoM data to validate the FVTD algorithm and code for CEM. Sinusoid incident wave results for the ogive are compared to Gaussian pulse incident wave results to illustrate the trade-offs between the two types of incident waves. The metrics established in Chapter 3 depict the differences between the FVTD RCS results and MoM and empirical RCS data.

To analyze the scattering from the ogive, the size of the grid is varied in each coordinate direction (R, θ, ϕ) to perform a grid convergent study and to obtain the optimum grid point density (GPD) for each coordinate direction. The grid for the cone-sphere was then generated using these optimal GPDs. The RCS results for the cone-sphere confirm the grid requirements obtained for the ogive and validate the FVTD algorithm for another PEC test body.

Several different computing platforms were used (See Chapter 3) to complete the FVTD tests for each scattering object. Several test simulations were completed on each platform to ensure the results were independent of the platform. Platform differences such as compiler optimization and floating point accuracy can affect the results. For example, the Cray 90 has a floating point accuracy of 14 digits as compared to the 7 digit accuracy of the DEC Alpha and SP-2 computing machines. Compiler options were used on the DEC Alpha and SP-2 machines to increase the floating point accuracy to that comparable to the Cray 90.

4.2 Ogive Electromagnetic Scattering Results

Table 1 is the test matrix listing the computer simulations completed for the ogive. The five ogive tests include several subtests. "OG" in the test number refers to a test for the ogive, and the number in the test designator refers to the test number. The last letter in each test number refers to the subtest. The subtests are groups of tests that use a specific incident wave, frequency, or grid size. In the discussion, a designator such as OG1X refers to the entire group of subtests. The tests are easily referenced in the discussion with the use of the test numbers.

Table 1: Ogive Test Matrix

Test Number	Incident Wave Type	Frequency (GHz)	Angle of Incidence	Grid Size (R, θ , ϕ)
OG1a	Sinusoid	1.18	0.0	36-74-45
OG1b	"	"	"	71-43-45
OG1c	"	"	"	71-74-25
OG1d	"	"	"	71-125-55
OG1e	"	"	"	71-43-25
OG1f ¹	"	"	"	71-74-45
OG2a	Gaussian	1.18	0.0	71-74-45
OG2b	"	"	"	"
OG3a ¹	Sinusoid	1.18	10.0	71-74-45
OG3b ¹	"	"	20.0	"
OG3c ¹	"	"	30.0	"
OG3d ¹	"	"	40.0	"
OG3e ¹	"	"	50.0	"
OG3f ¹	"	"	60.0	"
OG3g ¹	"	"	70.0	"
OG3h ¹	"	"	80.0	"
OG3i ¹	"	"	90.0	"
OG4a	Sinusoid	9.0	0.0	61-125-95
OG5a	Gaussian	1.0-7.0, $\Delta f=0.5$	0.0	76-125-75
OG5b	Sinusoid	1.0	0.0	83-74-35
OG5c	"	2.0	"	70-74-35
OG5d	"	3.0	"	69-74-45
OG5e	"	4.0	"	76-125-75

¹Separate tests were completed for HH (transmit horizontal, receive horizontal) and VV (transmit vertical, receive vertical) polarization. The grid size for HH polarization is (71-74-45). For VV, the grid size is (71-43-25).

The RCS results for the ogive for each test is compared to MoM RCS results and experimental data for VV and HH polarization. The first ogive tests, OG1X, are simulations which analyze the variation of the number of cells in each coordinate direction (R, θ, ϕ) using a sinusoid incident wave at 1.18 GHz. The ogive is one wavelength long at 1.18 GHz. Tests OG2X are two tests at 1.18 GHz using a Gaussian pulse for the incident wave with the frequency of interest near the center of the pulse and near the edge of the pulse. Tests OG3X are tests for monostatic calculations at 1.18 GHz. The bistatic RCS for the ogive at 9.0 GHz is test OG4a. The final tests, OG5X, compare results using sinusoid incident waves for various frequencies to the results from a Gaussian pulse incident wave test to illustrate the trade-offs between the use of each incident wave. For all of the bistatic tests, the angle of incidence is tip-on at 0° .

The data in Table 2 lists the stability and time data for each computer simulation such as the CFL value, time step, number of time steps per period, total number of periods, total number of time steps, and total CPU time. The CFL value used for the majority of the tests is 1.5. The maximum CFL value to enforce stability is 1.74; however, a smaller CFL value provides greater accuracy. A value of 1.5 provides reasonable accuracy and a time step close to the maximum. The time steps are normalized to the wave velocity of the medium. The time steps, if not normalized, are in the picosecond range. As discussed in the thesis scope in Chapter 1, this thesis research did not focus on speed optimization. Due to the structure of the grids and the tips of the ogive, the cell size can be very small relative to λ and the resulting time step is very small (i.e. $2.3221\text{E-}5$ or 0.07740 picoseconds for test OG4a). The total number of periods required for the test is related to the electrical size of the object. Normally, the computer test must be, in periods, two to four times the electrical length of the object. The computer simulation times for several tests are large (e.g. OG4a) for the higher frequencies due to the electrical length of the object and the small time step.

Table 2: Stability and Time Data for the Ogive Tests

Test Number	CFL	Δt (Seconds(c))	Time Steps/ Period	Total Periods	Total Time Steps	CPU Time ¹ (seconds)
OG1a	1.5	1.5030E-4	1692	7	11844	13194
OG1b	"	1.1674E-4	2178	"	15246	18137
OG1c	"	2.0210E-4	1258	"	8806	8831
OG1d	"	9.5292E-4	2668	"	18676	66744
OG1e	"	2.0210E-4	1258	"	8806	N/A
OG1f	"	1.1674E-4	2178	"	15246	27773
OG2a	"	2.0210E-4	N/A	N/A	14263	N/A
OG2b	"	2.0210E-4	N/A	N/A	14263	N/A
OG3X-HH	"	1.1674E-4	2178	7	15246	27851
OG3X-VV	1.7	2.2904E-4	979	5	4895	3156
OG4a ²	1.7	5.1749E-5	644	22	14168	79922
OG5a	1.5	5.8723E-5	N/A	N/A	17020	117396
OG5b	"	1.4938E-4	2009	7	14063	22831
OG5c ²	"	1.3159E-4	1140	8	18240	25902
OG5d ²	"	9.71272E-5	1030	13	13390	24190
OG5e ²	"	5.8723E-5	1277	14	17878	104909

¹Cray 90 CPU time

²The RCS convergence check was used for these FVTD tests

The grid point densities (GPD) in each coordinate direction (R, θ, ϕ) for each ogive test are shown in Table 3. The grid point density is defined as the number of finite-volume cells per wavelength, λ , and is significant when generating a grid for an object to ensure accuracy. In the radial direction, as explained in Chapter 3, the spacing of the cells increases as the distance increases from the surface of the scatterer. Therefore, the grid point density is much larger at the surface of the scatterer as compared to the outer edge of the grid. As can be seen in the table, the GPD varies from 200 to 602 cells/ λ at the surface and from 8.2 to 24.7 cells/ λ at the outer edge of the grid. The spacing required at the surface is due to the object's small electrical size and the tips which requires the correct calculation of the electromagnetic phenomena occurring at the surface such as creeping waves, traveling waves, and diffraction. In the radial direction, the outer edge of the grid is three wavelengths from the surface of the scatterer for every test.

Table 3: Grid Point Densities for the Ogive Tests

Test Number	GPD: R at Surface	GPD: R at Outer Edge	GPD: θ at Body	GPD: θ at Tip	GPD: ϕ at Body	GPD: ϕ at Tip
OG1a	255	10.5	57.4	104	64.2	1975
OG1b	513	21.1	21.8	104	65.2	1974
OG1c	510	20.9	57.4	104	32.1	987
OG1d	509	20.8	116	104	79.8	2468
OG1e	513	21.1	21.8	104	32.6	987
OG1f	510	20.9	57.4	104	64.2	1974
OG2a	513	21.1	21.8	104	32.6	987
OG2b	513	21.1	21.8	104	32.6	987
OG3X-HH	510	20.9	57.4	104	64.2	1974
OG3X-VV	513	21.1	21.8	104	32.6	987
OG4a	200	8.2	15.2	13.6	18.8	582
OG5a ¹	375	15.4	34.2	30.7	32.9	1019
OG5b	602	24.7	67.7	123	56.8	1747
OG5c	451	18.5	33.8	61.4	28.4	874
OG5d	401	16.4	22.6	40.9	25.2	777
OG5e	375	15.4	34.2	30.7	32.9	1019

¹Grid optimized for 4.0 GHz

For the other coordinate directions, theta and phi, the GPD is usually the smallest at the middle of the ogive and largest at the tips. For the cases in which the theta GPD at the tips is slightly less than the GPD at the body, as for test OG5a, the original grid was not changed in the theta direction and the grid spacing at the tip was slightly greater in the middle of the ogive body as compared to the tip. The theta GPD at the tips varies from 13.6 to 123 cells/ λ . In the phi direction, the body-of-revolution object forces the GPD to be large at the tips and smaller in the center of the body. The phi GPD in the center of the body is as large as 79.8 cells/ λ and as small as 18.8 cells/ λ . The GPD at the tips is the parameter used for determining the optimal GPD in the theta direction and the lowest GPD in the phi direction is the parameter used for determining the optimal GPD in that direction.

4.2.1 Ogive Bistatic RCS Results for 1.18 GHz, Sinusoid Incident Wave

The first set of tests, OG1X, study the scattering from the ogive at 1.18 GHz using a sinusoid incident wave. The incident wave is incident at 0° , or tip-on. Figures 12 through 15 are plots of the nose-on bistatic scattering from the ogive for VV polarization. Figures 12, 13, and 14 show the results as the grid point density is varied in the radial, theta, and phi directions, respectively (i.e. tests OG1a, OG1b, and OG1c). Test OG1f is considered the acceptable FVTD result after a grid convergence study was completed. The original size of the grid limited the grid sizes which could be generated. The number of grid points have to be a multiple of the original grid size.

As can be seen in Figure 12, the largest errors occur when the number of cells is decreased in the radial direction. The primary reason for the change is due to the first-order surface boundary condition which does not accurately predict diffraction and traveling waves unless the grid points are tightly packed at the surface. The GPD for OG1a as shown in Figure 12 is 255 cells/ λ in the radial direction and does not produce good results. To maintain accuracy, the first two cells in the radial direction must be small relative to the wavelength. For the ogive tests, OG1b through OG1f, the grid point density (GPD) at the surface in the radial direction is 513 cells/ λ . If the object is electrically larger, the GPD at the surface in the radial direction does not have to be as large, as will be seen for test OG4a, because the electromagnetic phenomena can be considered local.

In the theta and phi directions, the density can be decreased to 21.8-32.6 cells/ λ from 80-110 cells/ λ as can be seen in Figure 15 to obtain accurate results. As the grid point density decreases, the errors in the RCS occur first in the backscatter and forward scattering directions as would be expected because of the diffraction at the tips of the ogive.

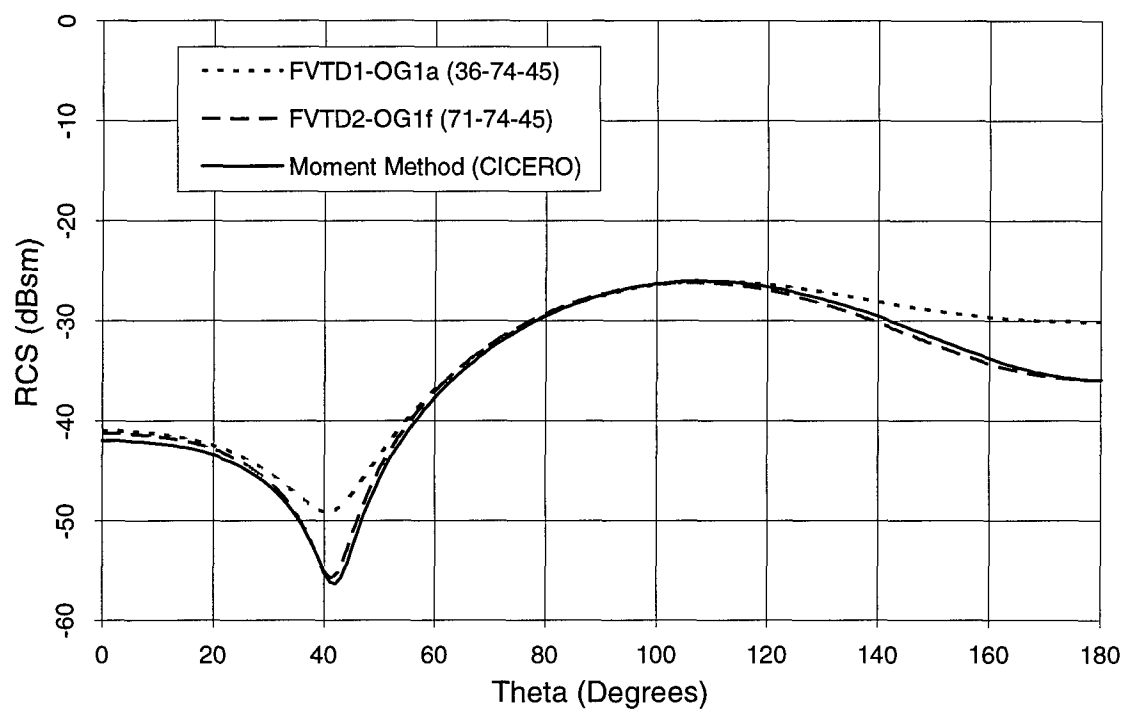


Figure 12: Ogive Bistatic RCS, 1.18 GHz, VV, Number of Cells Varied in R Direction

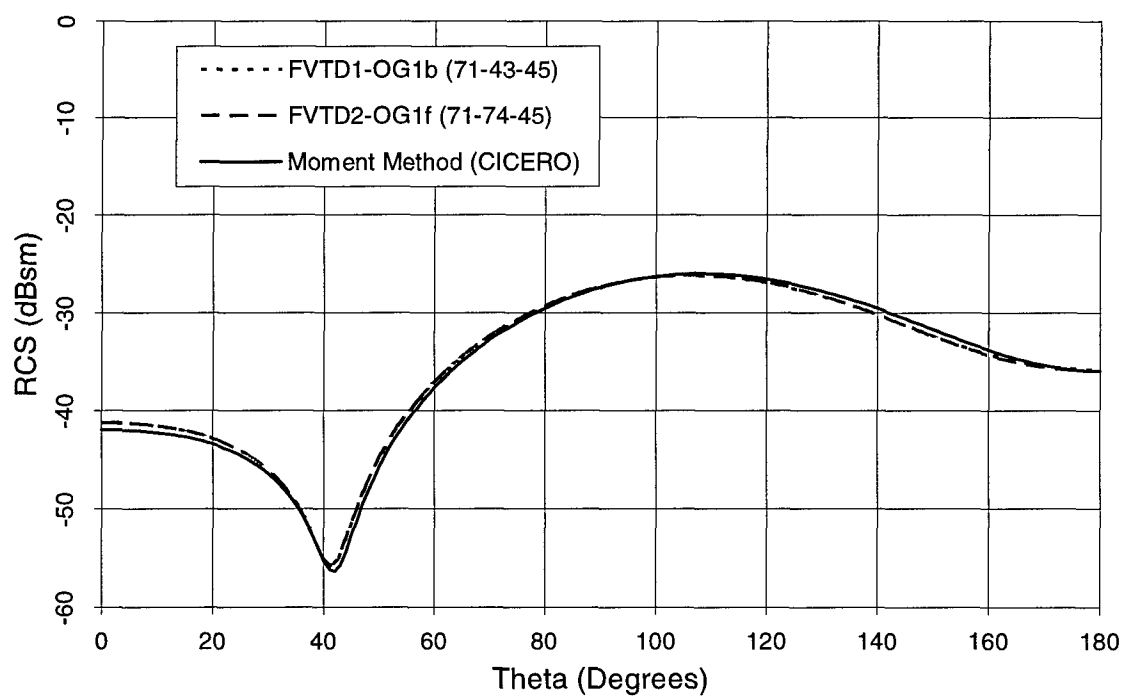


Figure 13: Ogive Bistatic RCS, 1.18 GHz, VV, Number of Cells Varied in θ Direction

In each plot for the ogive at 1.18 GHz, VV, the FVTD results are plotted against MoM results. A surface grid with 31 points along the arc was used to obtain the MoM results. Figure 16 shows the difference or error between the FVTD results for test OG1f and the CICERO MoM

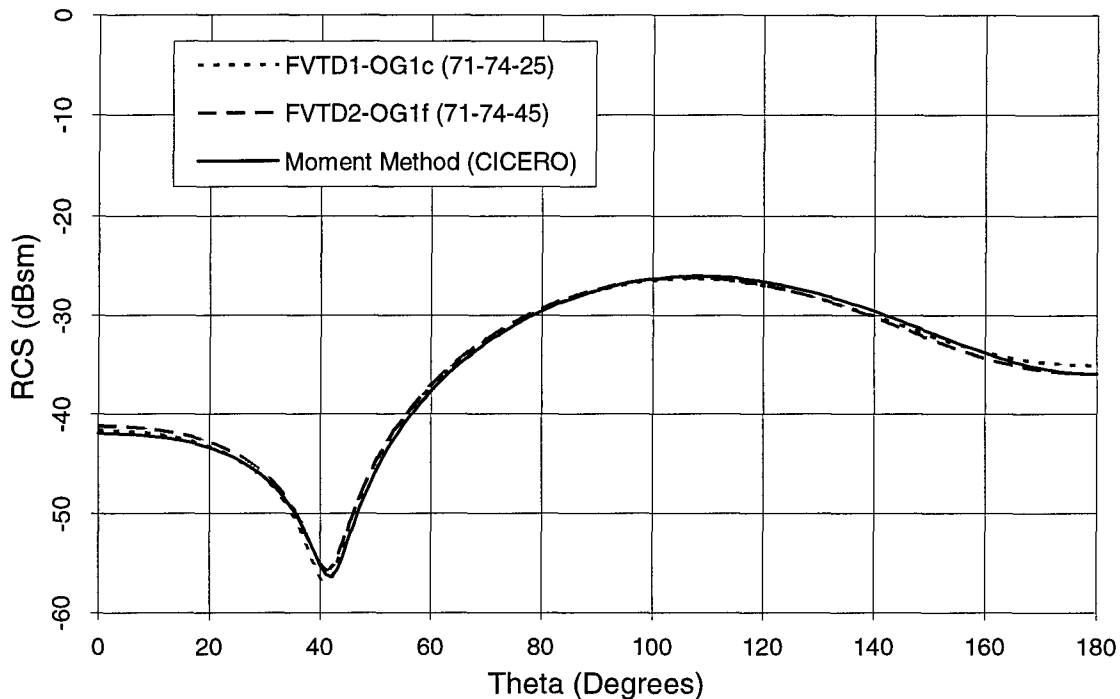


Figure 14: Ogive Bistatic RCS, 1.18 GHz, VV, Number of Cells Varied in ϕ Direction

results. The difference is no more than 0.71 dB if the phase difference is considered as described in Chapter 3. The largest difference occurs in the forward scattering region. Figure 17 illustrates the cross-correlation between the FVTD results from test OG1f, VV polarization, and MoM results. The plot clearly shows the FVTD and MoM results have a high correlation but the phase of the FVTD result is one or two degrees to the left of the MoM results. If the null in Figure 15 occurred at the same bistatic angle, the maximum correlation would occur at 180 degrees. Another representation of the accuracy of the FVTD results is shown in Figure 18 where

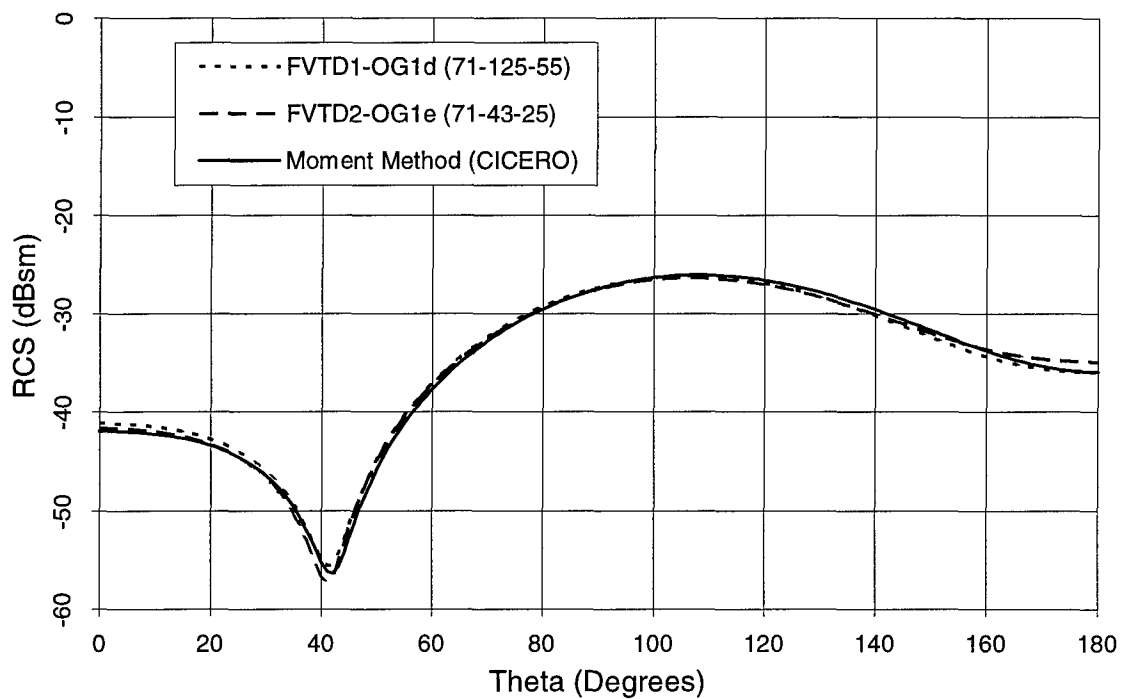


Figure 15: Ogive Bistatic RCS, 1.18 GHz, VV, Fine (71-125-55) vs. Coarse (71-43-25) Grid

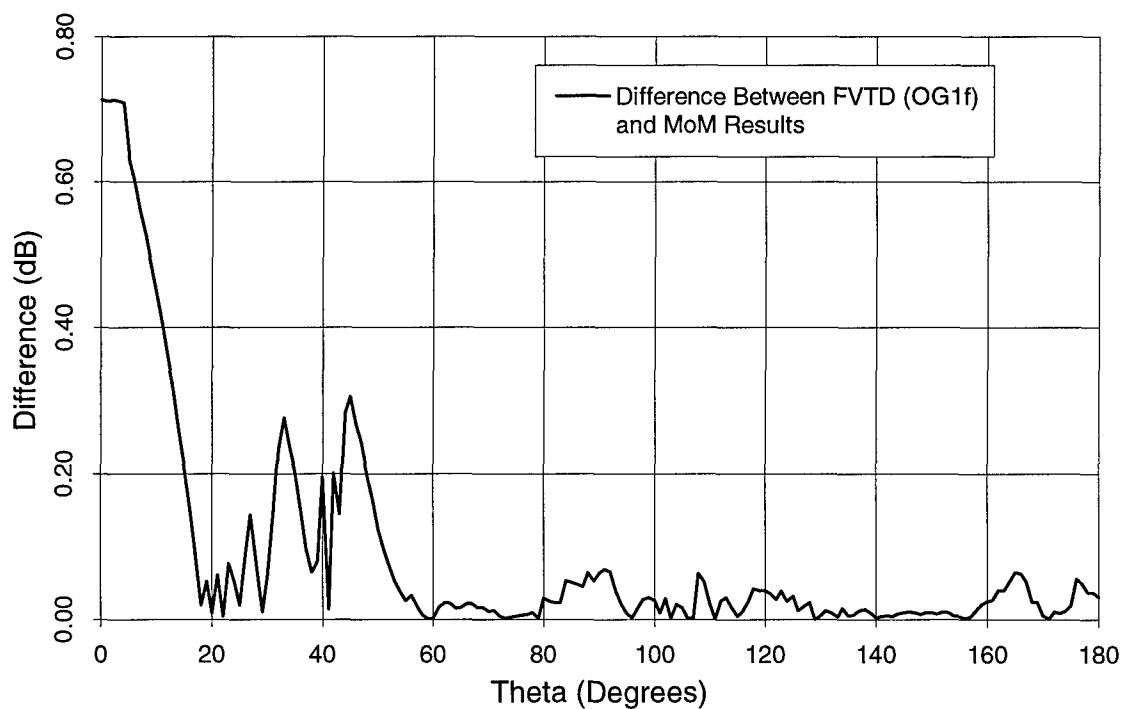


Figure 16: Ogive Bistatic RCS, 1.18 GHz, VV, Difference Between FVTD and MoM RCS

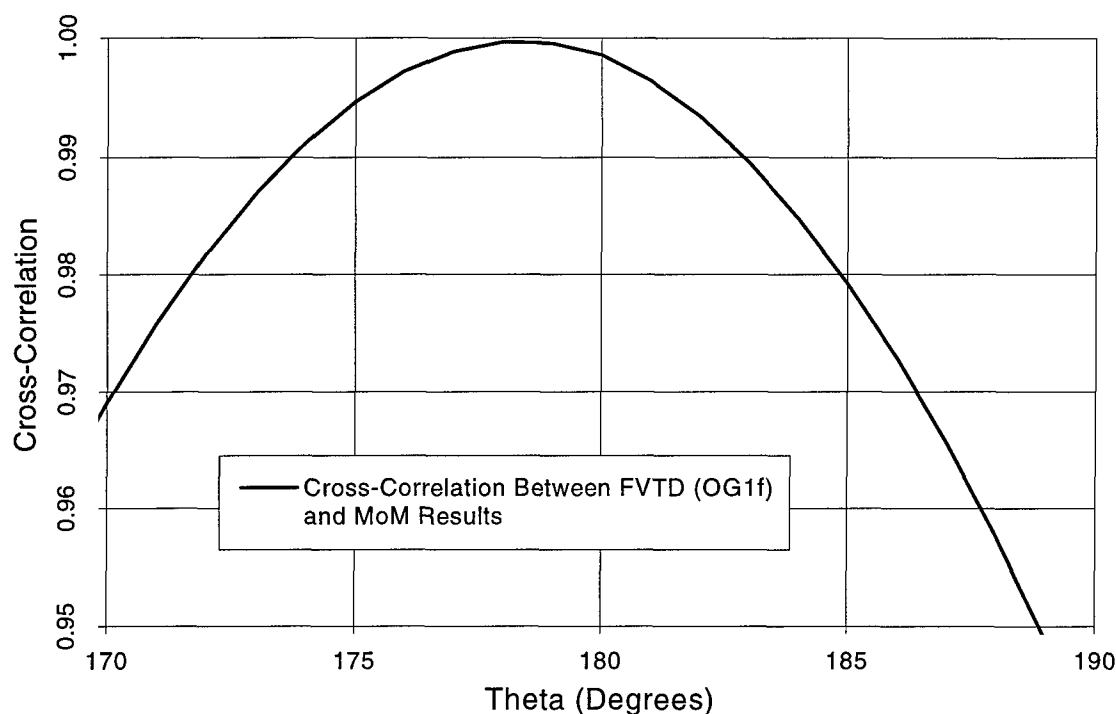


Figure 17: Ogive Bistatic RCS, 1.18 GHz, VV, Cross-Correlation of FVTD and MoM RCS

the Fourier transform of each plot is taken. The x axis has units of 1/degrees which has no physical meaning. The maximum magnitude corresponds to the large 140 degree arc in the bistatic plot. Before the Fourier transform was taken, the data was windowed with a Hamming window. If the FVTD and MoM results are not windowed first, the truncation of the data in the FT sequence produces unwanted oscillations in the curve. The metrics displayed in Figures 15-17 illustrate the small difference and high correlation between the FVTD and MoM RCS results.

The frequency data for tests OG1a to OG1f was taken from the fifth to the seventh periods to calculate the RCS data. Subsequent tests using the RCS convergence check showed the same results could be acquired if the data was taken from the fourth to the fifth periods. These tests revealed that for 1.18 GHz, the transients introduced with the sinusoid incident wave require at least four periods to diminish before frequency data can be taken for the RCS

calculations. Taflove recommends that at least four times the electrical length, in periods, are required [51]. The ogive results show that this approximation is appropriate for this frequency; however, fewer periods can be used for higher frequencies to obtain accurate data.

Similar results were obtained for HH polarization. The same grid sizes were tested and the results were similar. Figure 19 compares the coarse grid (OG1e) to the fine grid (OG1d). Figure 20 is the plot of the accepted result (OG1f) and the MoM results. Again, the results for

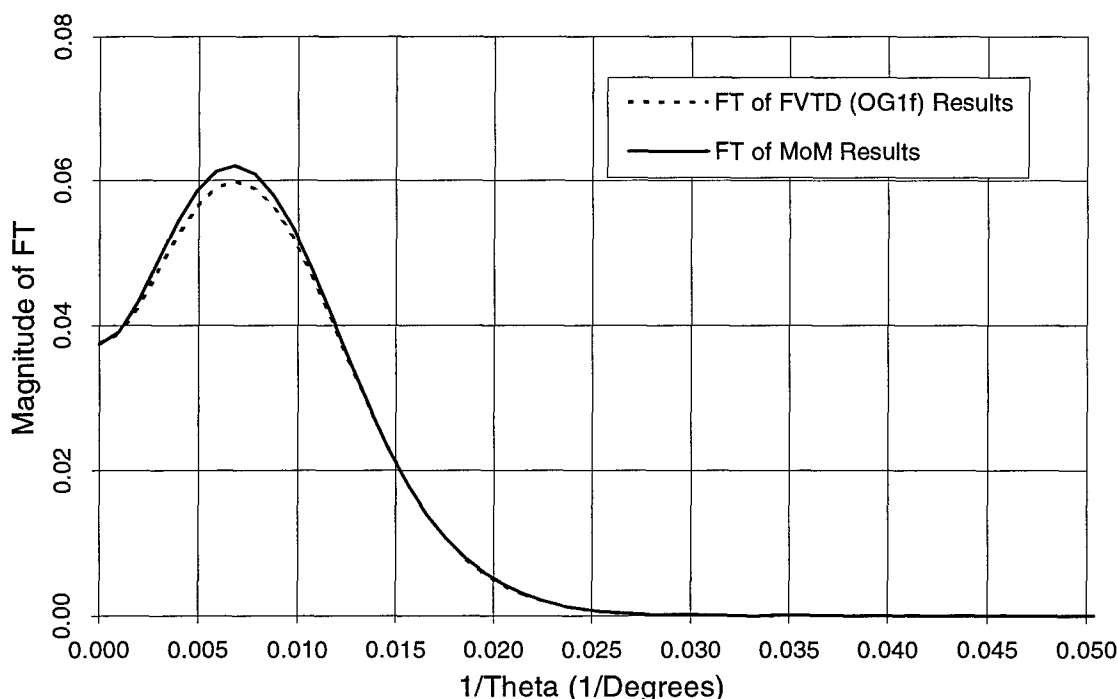


Figure 18: Ogive Bistatic RCS, 1.18 GHz, VV, Fourier Transform of FVTD and MoM RCS

OG1d are accurate within several dB, but for comparison, the slightly more accurate results from test OG1f are used to compare to the MoM results.

Figure 21 is the difference, in dB, between the FVTD and MoM results for HH polarization. The phase shift in the null was accounted for or the difference, in dB, would be much greater if taken point by point. The largest difference of approximately 2.0 dB occurs at

151°. The null in the FVTD solution at that location is not as deep as in the MoM solution. If the nulls are not considered, the greatest difference is approximately 0.7 dB. The cross-correlation was computed for the FVTD and MoM RCS results and the FVTD results were highly correlated with the MoM results, except the shift of the FVTD data was to the right by one or two degrees. This shift of two degrees can be seen visually in Figure 20. The Fourier transforms of the curves were taken and were very similar just as for the VV RCS results.

The FVTD results for the ogive at 1.18 GHz using a sinusoid incident wave were excellent when compared to MoM results. The results illustrated that for electrically small objects, the FVTD algorithm correctly computes diffraction and traveling waves. The small electrical size also allowed a relatively large time step resulting in a reasonable simulation time. For test OG1e, the Cray 90 CPU time was approximately 3200 seconds. For higher frequencies, as shown in Table 2, the computer simulation times are much longer.

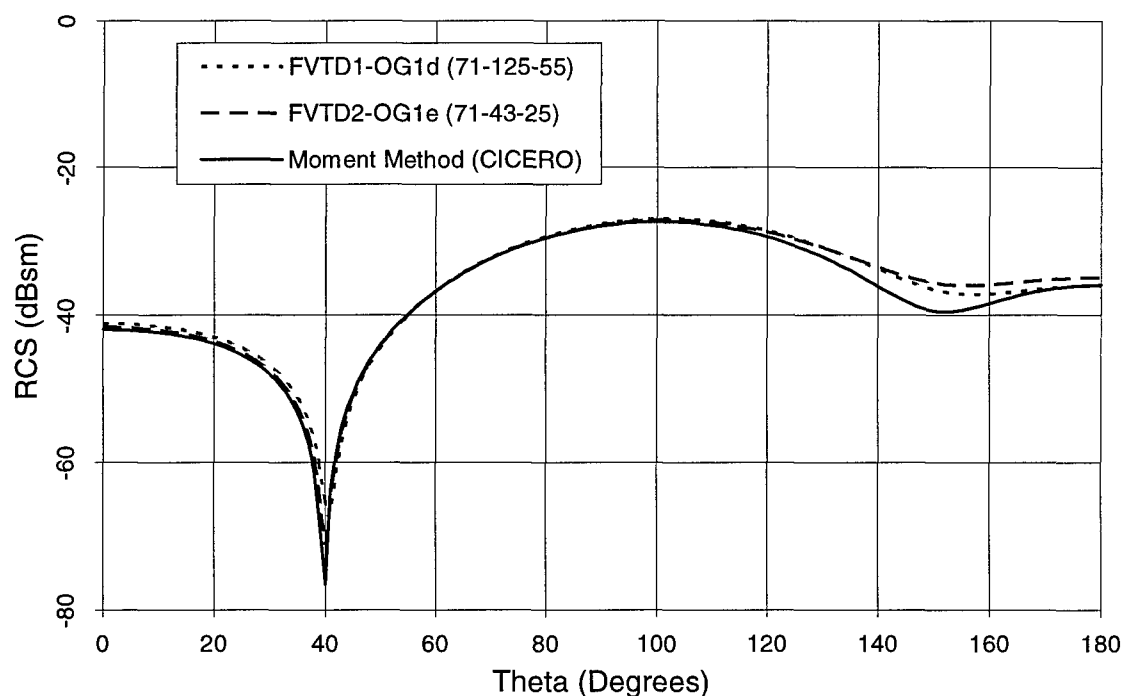


Figure 19: Ogive Bistatic RCS, 1.18 GHz, HH, Fine (71-125-55) vs. Coarse (71-43-25) Grid

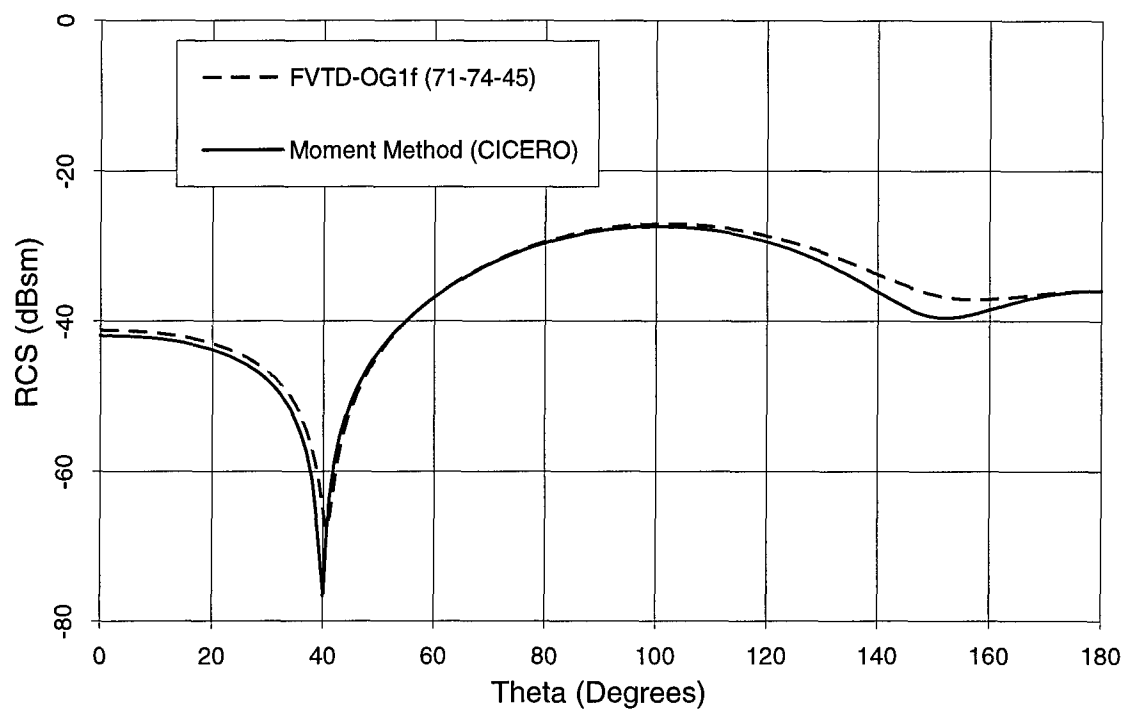


Figure 20: Ogive Bistatic RCS, 1.18 GHz, HH

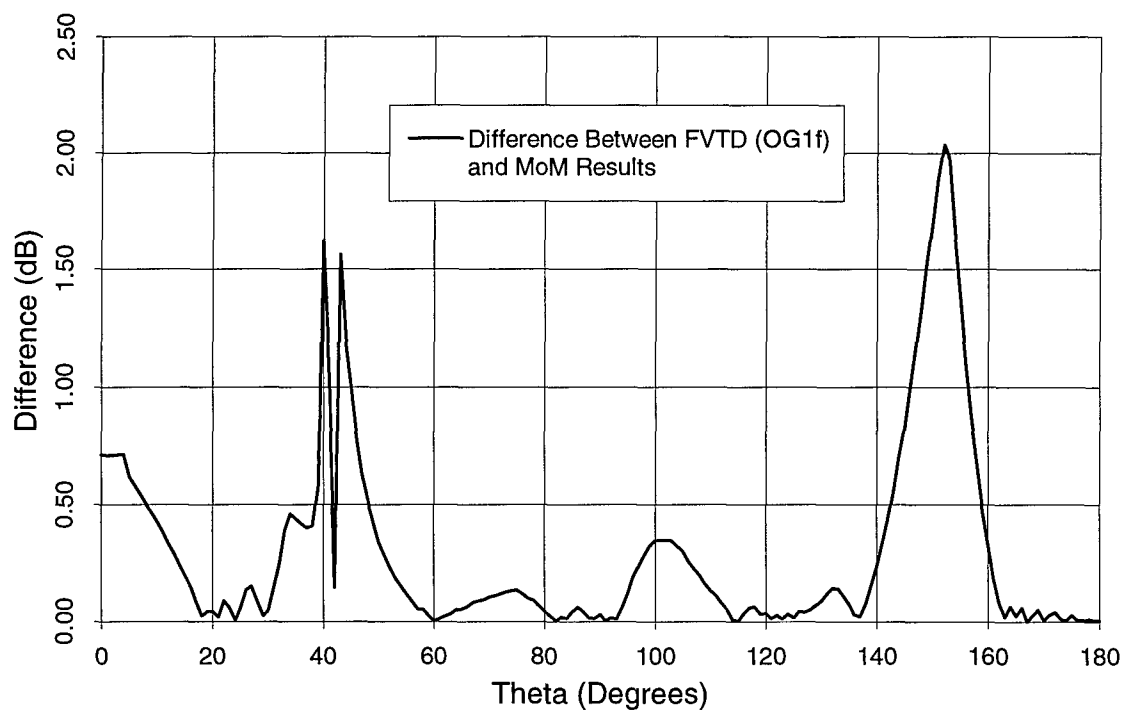


Figure 21: Ogive Bistatic RCS, 1.18 GHz, HH, Difference Between FVTD and MoM RCS

4.2.2 Ogive Bistatic RCS Results for 1.18 GHz, Gaussian Pulse Incident Wave

The accuracy of the Gaussian pulse incident wave is illustrated in Figures 22 and 23. One-third of the bandwidth of the pulse is considered to be adequate to take frequency data. This is illustrated in the plots for tests OG2a and OG2b. Test OG2a placed the frequency of interest, 1.18 GHz, near the center of the pulse bandwidth. A Gaussian pulse with a duration of 0.017831, normalized to c , and a radian frequency delta of 12.35693 rad/s was used to place the frequency near the center of the pulse. The test, OG2b, placed the frequency near the edge of the usable bandwidth by using a Gaussian pulse with a duration of 0.100000 and a radian frequency delta of 2.471386 rad/s. The results are almost identical. Appendix B contains detailed data for specifying the parameters for the Gaussian pulse incident wave.

The vertical polarization case is plotted in Figure 22. The Gaussian pulse RCS results, OG2X, are compared to MoM RCS results. The horizontal polarization case is shown in Figure 23. The Gaussian pulse RCS results, OG2X, match the RCS calculations of test OG1e which also used the coarse grid size of (71-43-25). The results for the grid size of (71-43-25) are nearly as accurate as the results for the grid size of (71-74-45) to permit use of the smaller grid. The savings in computer time also justifies the use of the smaller grid.

The comparison of tests OG1X and OG2X illustrate the accurate results which can be obtained with either a Gaussian pulse or sinusoid incident wave. The computer run times for the Gaussian pulse tests, OG2X, are greater than the times for the sinusoid (approximately 9600 seconds vs. 3200 seconds). This factor of three will not always be the relationship between run times. The electrical length of the object and the grid size will affect the computer run times. The sinusoid incident wave is clearly the correct incident wave to use if the RCS is desired for a single frequency. The Gaussian pulse is used when the simulation time is less than the total time required for the individual sinusoid tests. Test OG5X looks at these trade-offs in more detail.

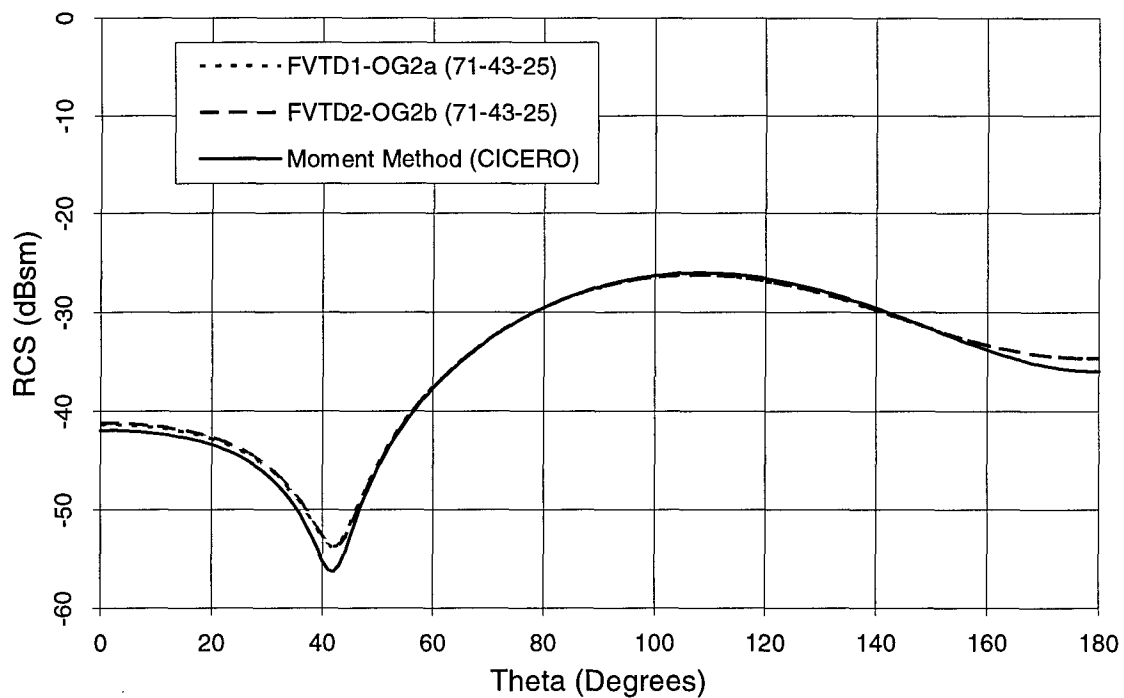


Figure 22: Ogive Bistatic RCS, 1.18 GHz, VV, Gaussian Pulse Incident Wave

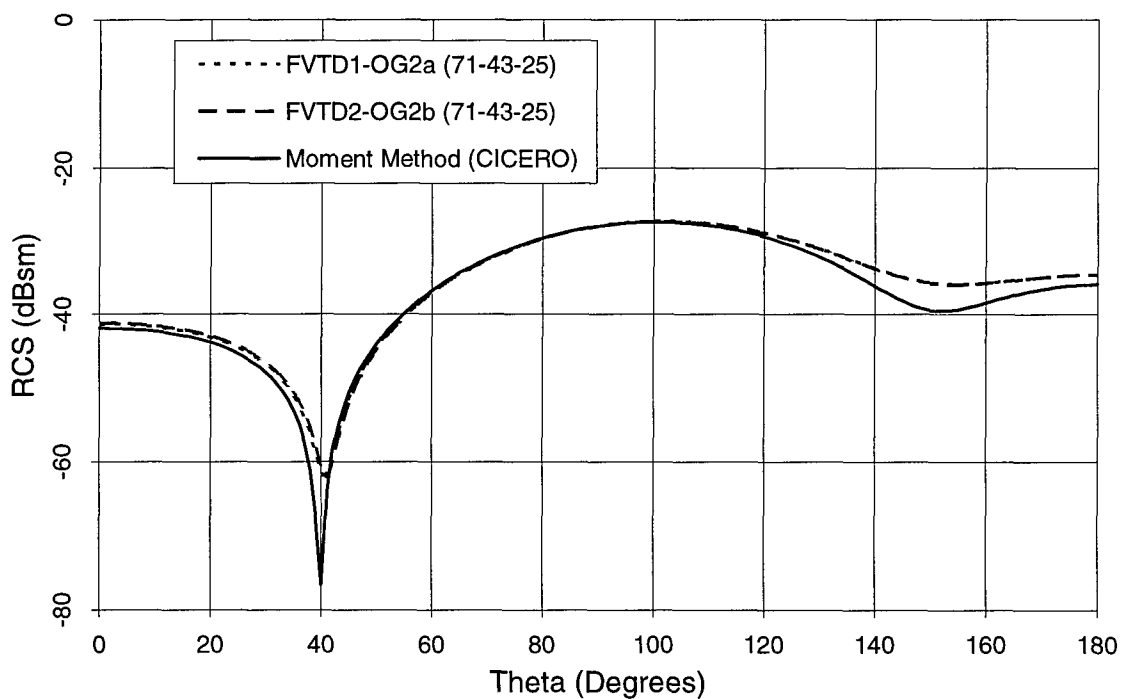


Figure 23: Ogive Bistatic RCS, 1.18 GHz, HH, Gaussian Pulse Incident Wave

4.2.3 Ogive Monostatic RCS Results for 1.18 GHz

In addition to bistatic results, the FVTD code can also obtain monostatic data. Multiple simulations have to be completed to obtain monostatic data for one frequency as compared to one test for bistatic data. One simulation produces a bistatic plot for 0° to 180° . The simulation produces a monostatic result for one angle, the angle of incidence. To obtain a full monostatic sweep, a bistatic-to-monostatic approximation is used (See Chapter 3). The approximation requires tests to be completed every 10° and bistatic data completes the monostatic approximation. Tests OG3X are monostatic calculations for the ogive at 1.18 GHz. A test was completed for an angle of incidence every 10° from 0° to 90° . The ogive is symmetric about the xy plane resulting in a symmetric monostatic plot about $\theta=90^\circ$.

The monostatic approximation for HH polarization is plotted in Figure 24. The HH monostatic test used a grid size of (71-74-45), and frequency data was taken from the fifth to the seventh period. The FVTD results are plotted against MoM RCS results and empirical RCS data. As can be seen in the plot, the MoM and FVTD results are almost identical and differ from the empirical data by nearly the same value. In Figure 25, the difference between the FVTD, MoM, and empirical results is plotted. The FVTD results differ from the MoM results by no more than 2.5 dB. If the large fluctuations are ignored in the empirical data, the FVTD results are within 3.1 dB of the empirical data. The FVTD results differ from the empirical data by 2.8 dB at the tips ($\theta=0^\circ$ and $\theta=180^\circ$) and 2.5 dB at broadside incidence ($\theta=90^\circ$).

The VV polarization results for the monostatic calculations are shown in Figure 26. For this group of tests, a grid size of (71-43-25) was used. Again, the FVTD results are excellent when plotted against MoM and experimental RCS data. The FVTD results, however, do not agree well at the nulls at 30° and 150° . The difference between the FVTD results and the other data, shown in the figure, can be as large as 8-10 dB in the nulls.

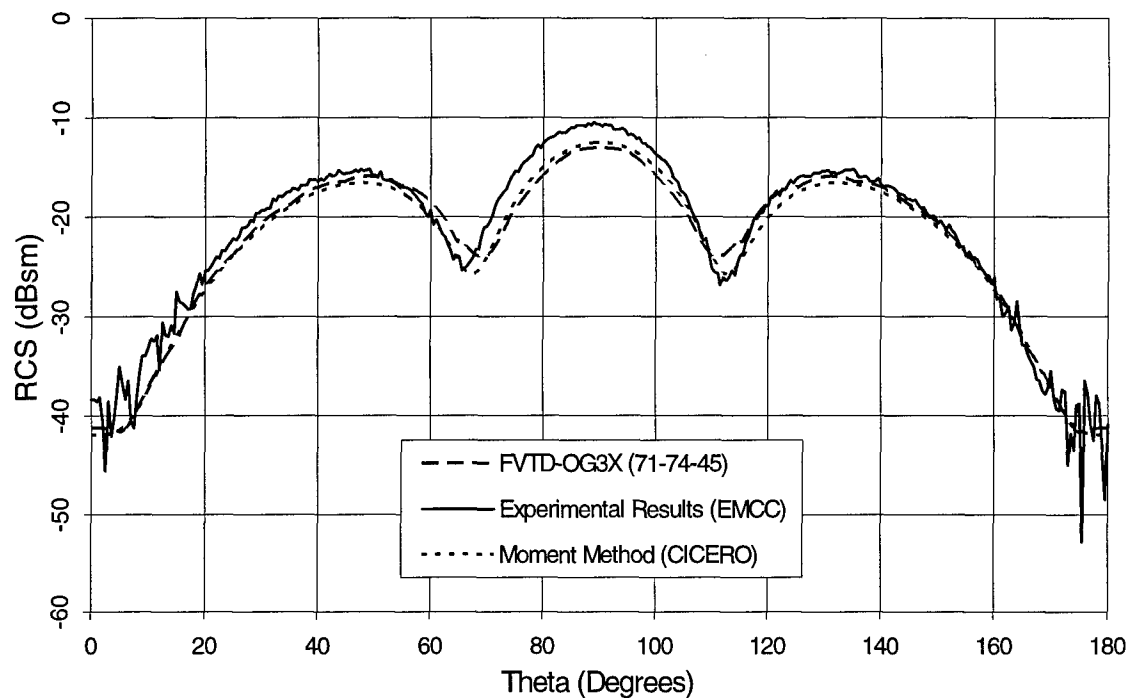


Figure 24: Ogive Monostatic RCS, 1.18 GHz, HH

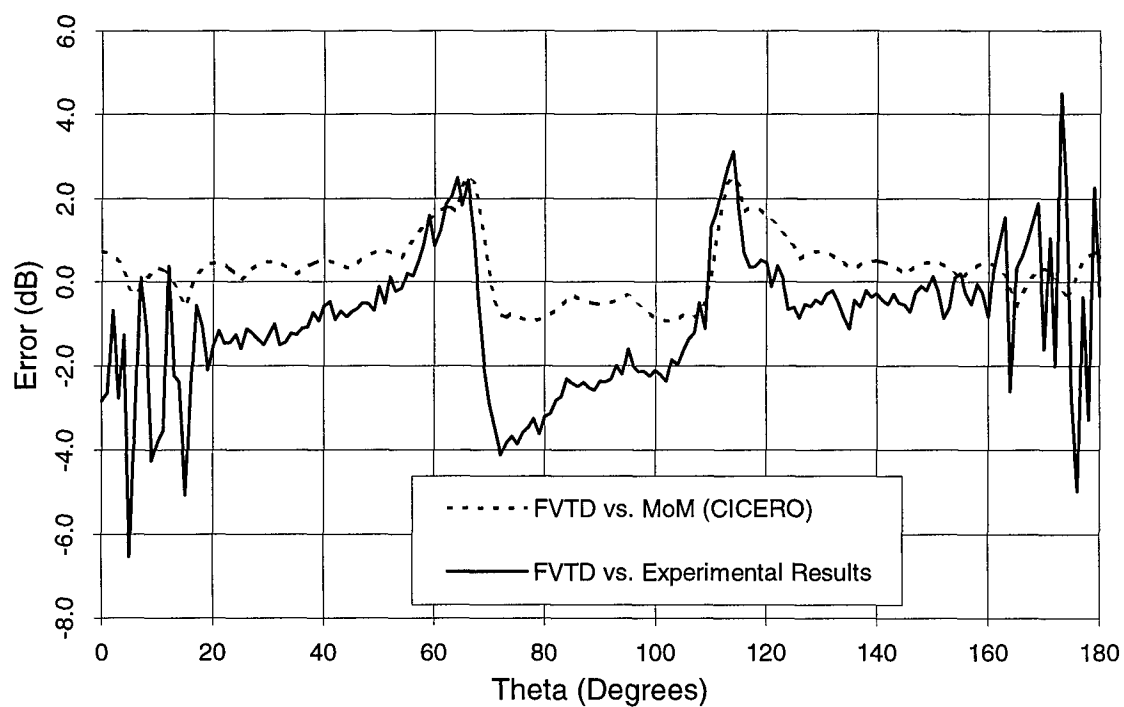


Figure 25: Ogive Monostatic RCS, 1.18 GHz, HH, Error Between RCS Results

The accuracy and limitations of the bistatic-to-monostatic approximation can be determined by close observation of the FVTD monostatic plots. The data at 10° increments, such as 0° , 10° , 20° , etc., are the true monostatic FVTD RCS results and are in agreement with the MoM RCS results. However, the data at the angles 5° , 15° , 25° , 35° , 45° , etc. are at the junction of the approximation data from each monostatic test. Slight discontinuities can be seen at these angles. For example, the monostatic data for 25° - 35° degrees is obtained from the bistatic test

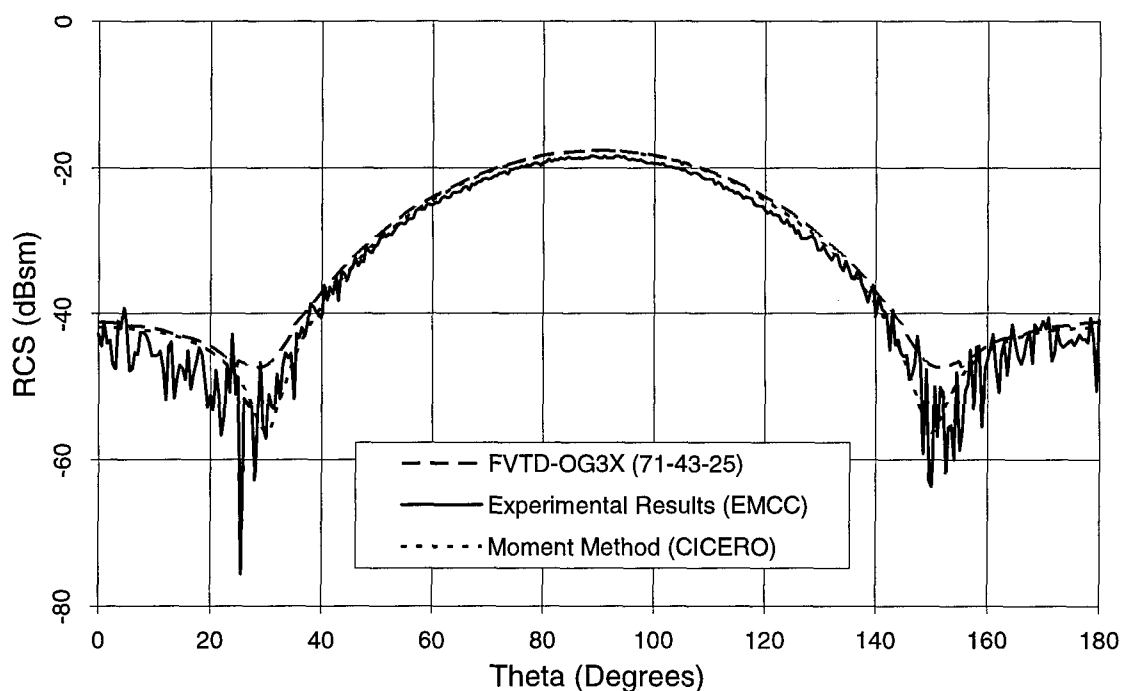


Figure 26: Ogive Monostatic RCS, 1.18 GHz, VV

at 30° . The monostatic data for 35° - 45° is taken from the 40° bistatic test. A small discontinuity can be seen at 35° . The approximation is only good for small angles, 5° or less. If the discontinuity is great, the approximation is not poor, but more monostatic tests have to be made for more angles so the approximation is used for smaller angles. A large number of oscillations in the plot can require a greater number of monostatic tests (i.e. higher frequencies).

4.2.4 Ogive Bistatic RCS Results for 9.0 GHz

The ogive tests completed previously were at one frequency, 1.18 GHz. Further analysis is completed for the ogive using FVTD by running a test, OG4a, for the ogive at 9.0 GHz. The ogive is approximately 7.6 wavelengths long at this frequency. The grid size required for this frequency is much larger along with an increased simulation time. The wavelength is smaller at 9.0 GHz, but the time step is much smaller due to the fine grid resulting in a large simulation time (i.e. 79,922 seconds) as seen in Table 2.

The ogive results for 9.0 GHz, HH polarization, are shown in Figure 27. The FVTD results for 9.0 GHz, VV, are shown in Figure 28. The FVTD results are plotted against MoM RCS data. The results are excellent, except there are small discrepancies for the backscatter and forward scattering regions. The grid densities for these tests are smaller than for 1.18 GHz. The GPDs in the theta and phi directions are 15.2 cells/ λ and 18.8 cells/ λ , respectively. The results for the ogive at 1.18 GHz showed that a GPD of approximately 22-32 cells/ λ gives the best data. These results depict the dependence of the required GPD on the electrical size of the object. The GPD can be smaller, 15-20 cells/ λ , as the electrical length of the object gets larger.

The 9.0 GHz results for the ogive illustrate the dependence of the length of simulation time, in periods, to the length of the object. At 1.18 GHz, the test had to be at least four times, in periods, the length of the object. The same factor would require a simulation time of 30 periods for 9.0 GHz. This is not required because, at 9.0 GHz, the ogive is in the optical region. As a rule of thumb, the optical region is encountered for an object greater than approximately 7λ [27]. At 9.0 GHz, the diffraction and the traveling waves can be considered to be more of a local phenomena than for 1.18 GHz. This reduces the simulation time for the test to approximately three times the length of the object, in periods, instead of four.

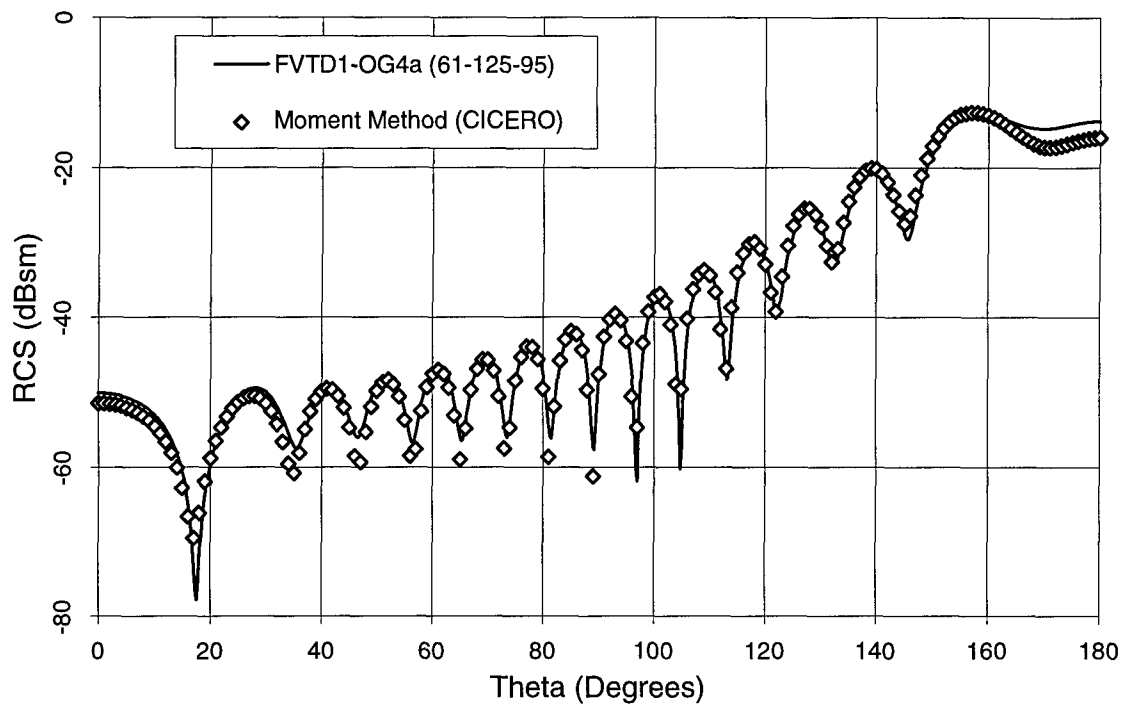


Figure 27: Ogive Bistatic RCS, 9.0 GHz, HH

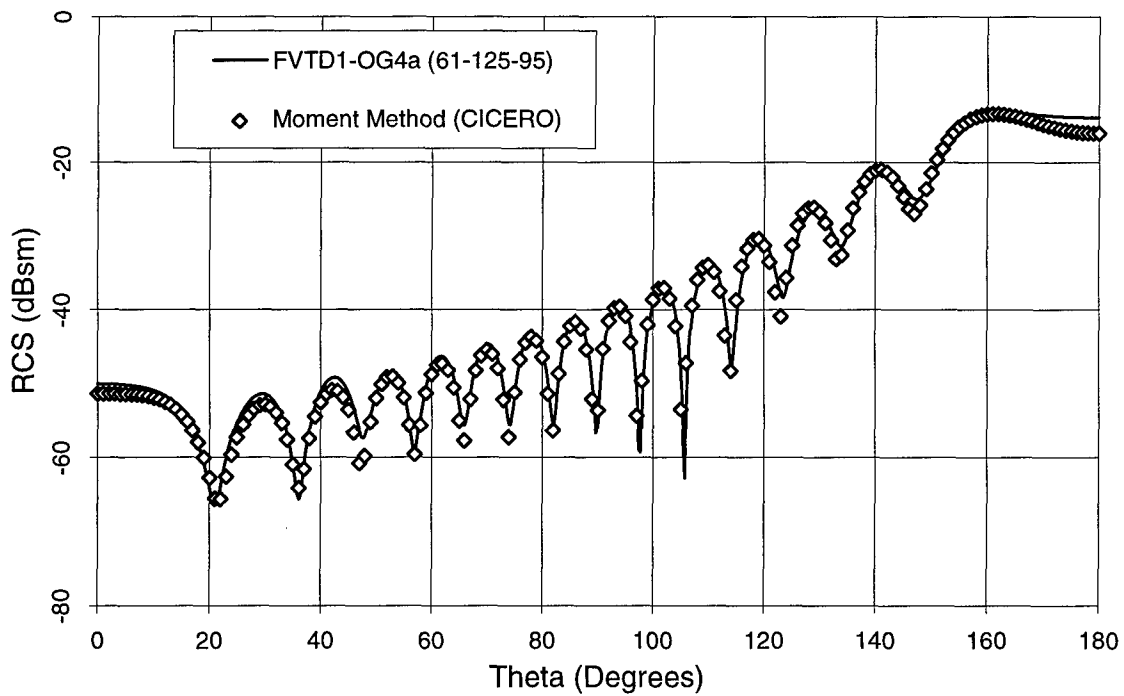


Figure 28: Ogive Bistatic RCS, 9.0 GHz, VV

The results for the ogive at 9.0 GHz begin to show the limitations of the explicit FVTD algorithm and available computing resources. The stability of the explicit time-domain algorithm is related to the cell size which is small for this grid at 9.0 GHz. The grid size is large to meet the GPD requirements and the fineness of the grid at the tips forces the time step to be small. The small time step, the large grid size, and the number of periods required to obtain accurate frequency data results in a long simulation time (i.e. 79,922 seconds). Accuracy in the backscatter and forward scattering regions is sacrificed for a faster run time and smaller grid.

4.2.5 Ogive Bistatic RCS Results for the Gaussian Pulse Incident Wave

The option of specifying either a sinusoid or Gaussian pulse for the incident wave gives the user flexibility in obtaining FVTD RCS data for one frequency or multiple frequencies, respectively, depending on the results desired. The Gaussian pulse provides RCS data for multiple frequencies but normally requires a longer run time (See Table 2); therefore, a sinusoid is ideal for single frequency RCS data. Included in this section are results for several frequencies using a Gaussian pulse. The Gaussian pulse RCS data are compared to sinusoid incident wave RCS data and the results for one frequency, 4.0 GHz, are also compared to MoM RCS results.

The Gaussian pulse used for test OG5a was optimized for 4.0 GHz. The grid used, (76-125-75), was also optimized for that frequency. The bistatic RCS results for frequencies less than 4.0 GHz are excellent and will be shown. The GPDs due to the grid size for frequencies below 4.0 GHz are sufficient to provide excellent results. The Gaussian pulse for test OG5a had a width of 0.0182556 (See Appendix B) with a radian frequency delta of 10.471975 rad/s (0.5 GHz). The Gaussian pulse width had a bandwidth of 21.0 GHz and a usable BW of 7.0 GHz for these parameters. The grid was optimized for 4.0 GHz so results for higher frequencies are not discussed.

The FVTD results for 1.0 GHz using the Gaussian pulse (OG5a) and a sinusoid (OG5b) are shown in Figure 29, HH, and Figure 30, VV. The RCS convergence check was not used for test OG5b. The results are identical except for a negligible small difference in the forward scattering region which could be due to a different grid size, numerical dispersion, or reflections from the outer boundary. Slight differences were seen previously for different grid sizes. The longer run time for the Gaussian pulse test can introduce numerical dispersion which accumulates during the test. Also, the longer simulation for the Gaussian pulse may allow the reflections from the outer boundary to affect the results more than for the sinusoid test.

The Gaussian pulse incident wave also provided RCS data for 2.0 GHz. The HH polarization results are shown in Figure 31. As can be seen in the figure, the data for the Gaussian pulse (OG5a) and sinusoid incident wave (OG5c) are almost identical. A small difference exists between the results in the forward scatter direction. The RCS convergence check was used for test OG5c. The VV polarization result is shown in Figure 32. The results are identical except for a slight difference in the forward scatter region.

The results comparing Gaussian pulse RCS data to sinusoid data reveal several important computational issues requiring attention when obtaining FVTD results. The Gaussian pulse results accurately predict the backscatter and forward scatter regions. Results from a sinusoid incident wave will not if the transients have not diminished. The convergence check for the sinusoid was programmed to take data for one period, sample the RCS values, take data for another period, and sample again. Other FVTD tests showed that more accurate results can be obtained from sampling data over a two to three period span. A convergence check designed to sample every two or three periods would provide a more robust and accurate method of ensuring accurate results from a sinusoid incident wave, especially for higher frequencies. At higher frequencies, the enormous run times require methods which ensure accurate results with one test.

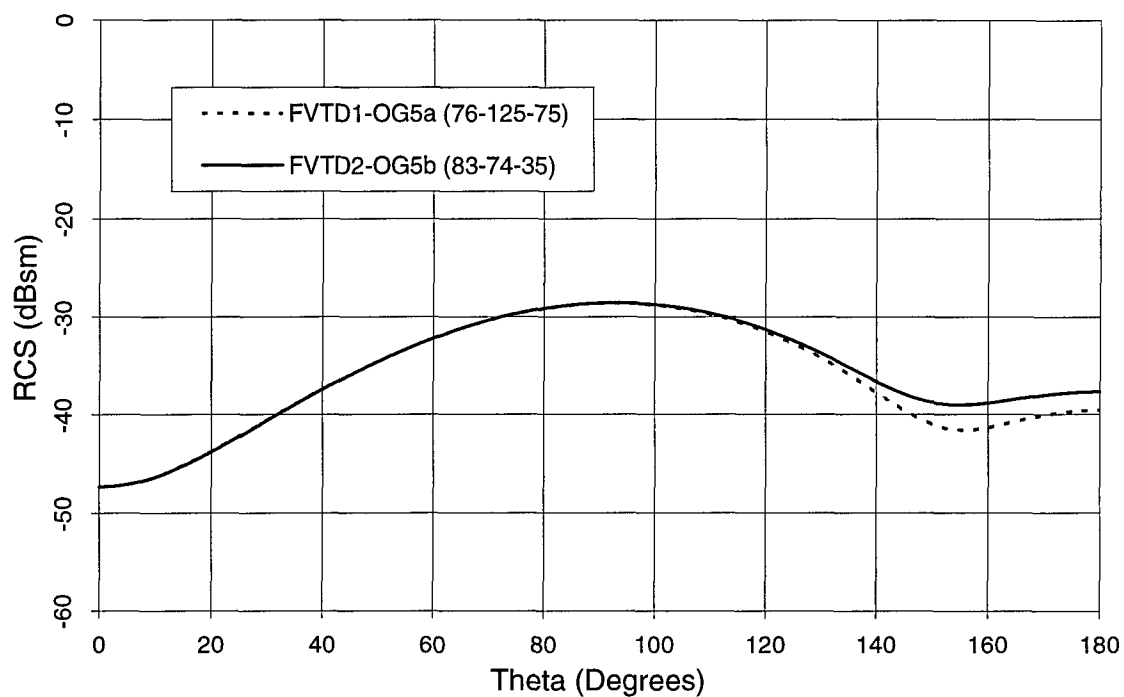


Figure 29: Ogive Bistatic RCS, 1.0 GHz, HH, Gaussian Pulse vs. Sinusoid Incident Wave

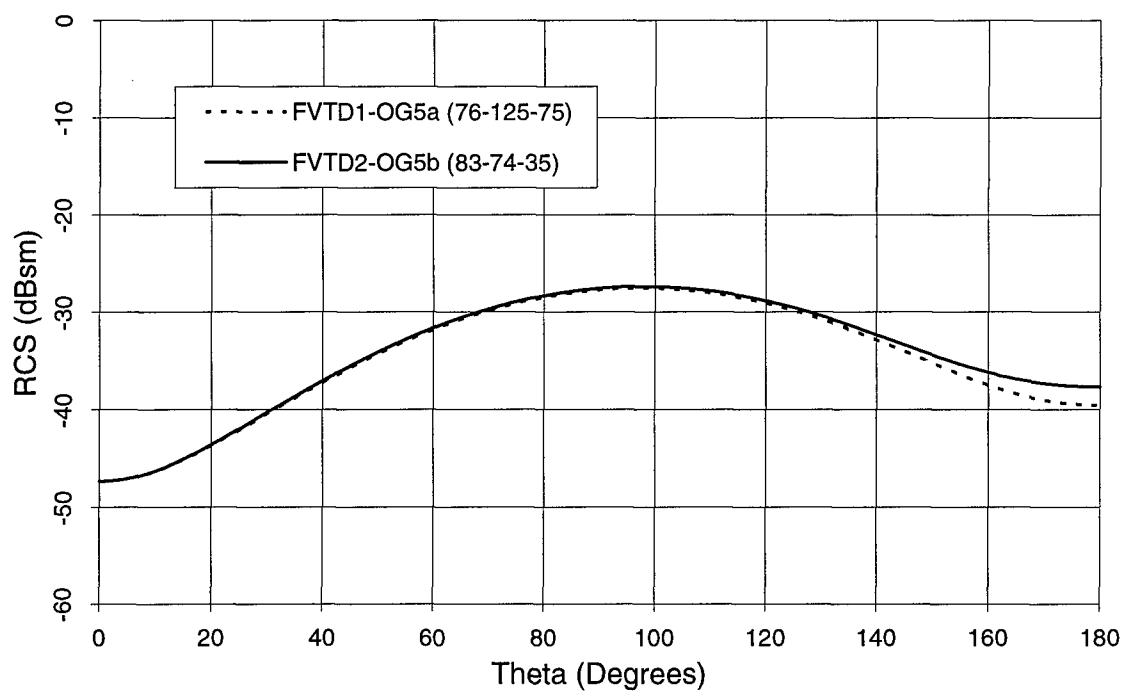


Figure 30: Ogive Bistatic RCS, 1.0 GHz, VV, Gaussian Pulse vs. Sinusoid Incident Wave

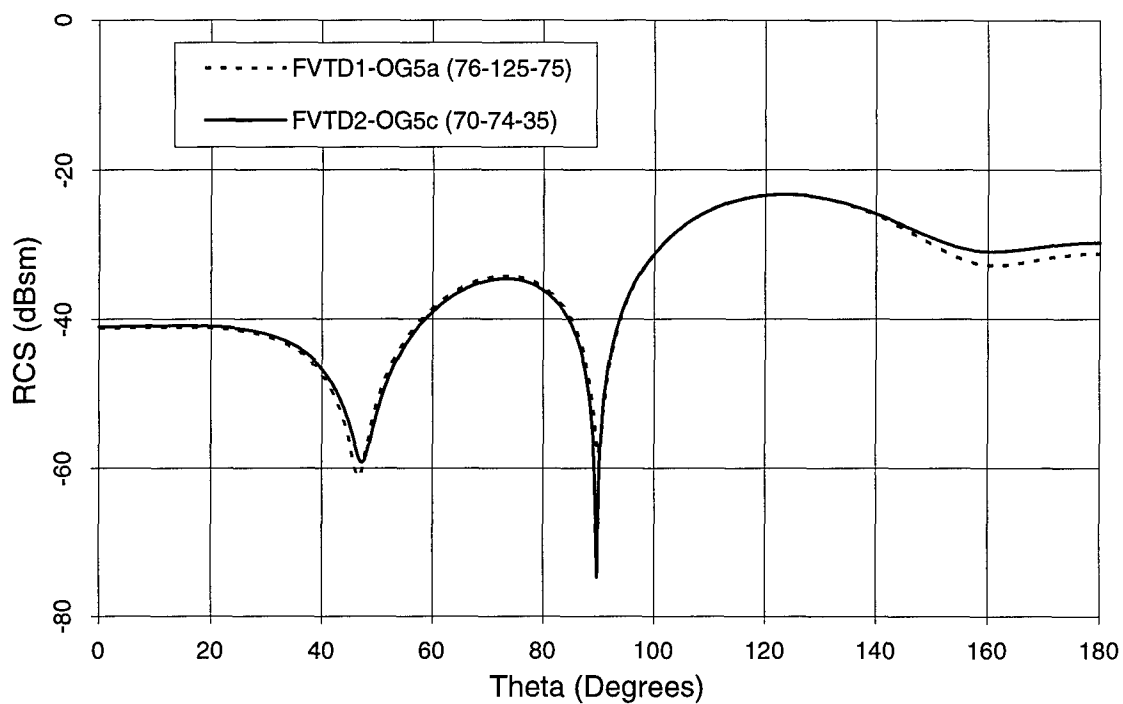


Figure 31: Ogive Bistatic RCS, 2.0 GHz, HH, Gaussian Pulse vs. Sinusoid Incident Wave

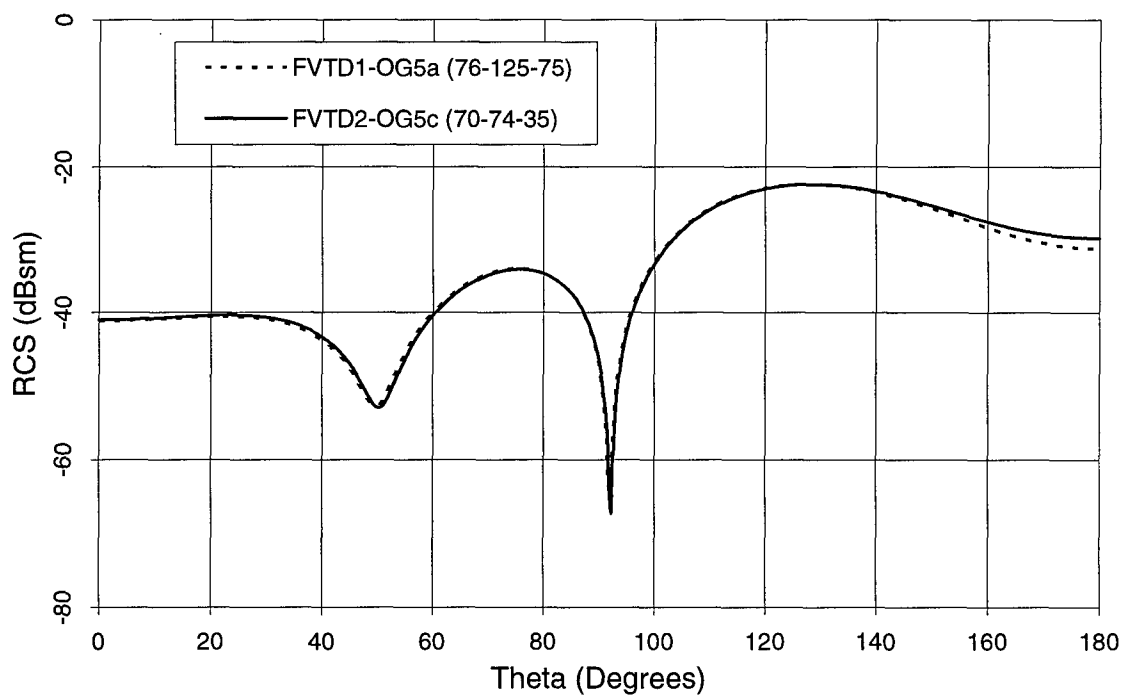


Figure 32: Ogive Bistatic RCS, 2.0 GHz, VV, Gaussian Pulse vs. Sinusoid Incident Wave

Another computational issue which arises with the use of the Gaussian pulse is the location of the outer boundary for each frequency. The grid, when using a Gaussian pulse, is optimized for a specific frequency with the location of the outer boundary three wavelengths from the scatterer. The test gives results for lower frequencies, but the outer boundary for the lower frequencies is less than three wavelengths away from the scatterer surface. For example, the outer edge of the grid for 2.0 GHz in test OG5a is 1.5 wavelengths from the surface of the scatterer. As the frequency decreases, the reflections from the outer boundary will increase the errors for those particular frequencies. The slight errors in the forward scatter regions for 1.0 and 2.0 GHz are most likely due to the reflections from the outer boundary as opposed to numerical dispersion in the Gaussian pulse test.

In Figure 33, the accurate results for 3.0 GHz, HH, is illustrated using a Gaussian pulse (OG5a) and a sinusoid (OG5d). The VV polarization case is shown in Figure 34. The grid sizes for each test are different, but the results are almost identical. No errors in the forward scatter region reveal that numerical reflections are causing the slight errors in the forward scatter area for the lower frequencies of 1.0 and 2.0 GHz.

Test OG1d ran for thirteen periods, although convergence was almost reached at 10 periods (within 0.12 dB as compared to 0.1 dB for the RCS convergence check). At 10 periods, the simulation time is approximately four times the electrical length of the ogive. The electromagnetic phenomena, including diffraction at the tips and traveling waves along the surface of the body, require time to stabilize. These frequencies dictate that the electromagnetic scattering cannot be considered local phenomena. Multiple diffractions from the tips due to traveling waves require time to establish and stabilize. As the electrical size of the object gets larger, as for the case of 9.0 GHz, the multiple diffractions are not as prominent and less time is required to establish the stabilized fields.

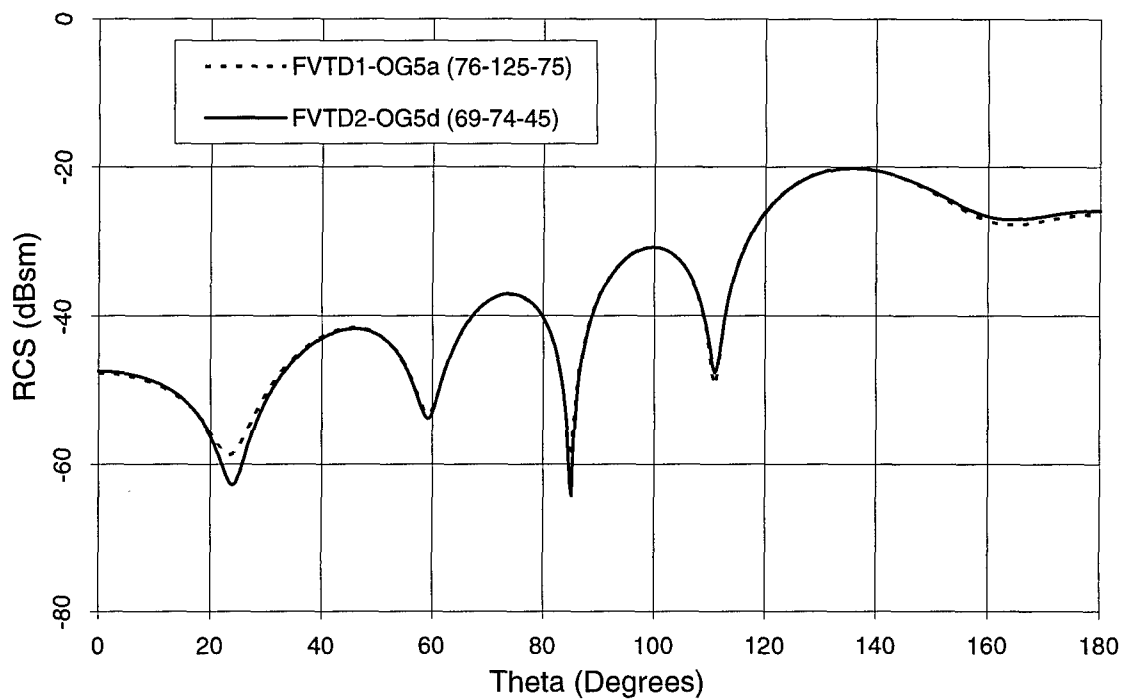


Figure 33: Ogive Bistatic RCS, 3.0 GHz, HH, Gaussian Pulse vs. Sinusoid Incident Wave

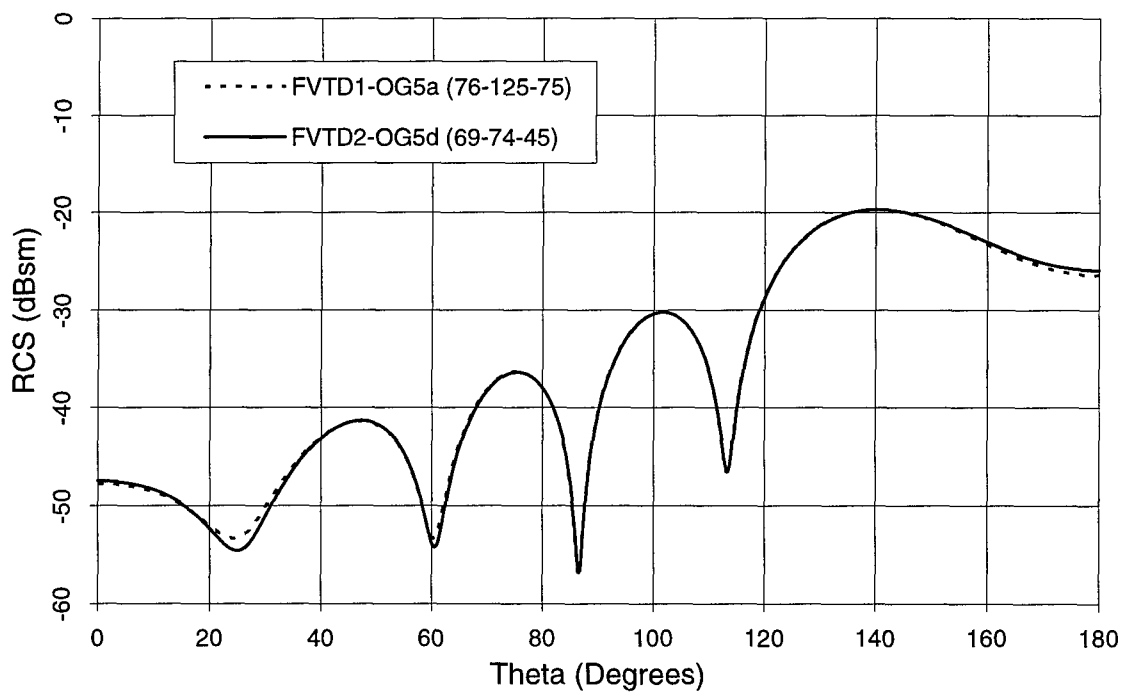


Figure 34: Ogive Bistatic RCS, 3.0 GHz, VV, Gaussian Pulse vs. Sinusoid Incident Wave

To conclude, the excellent results using a Gaussian pulse at 4.0 GHz for the ogive is discussed. Tests OG5a and OG5e were optimized for 4.0 GHz. The ogive is approximately 3.4 wavelengths long at this frequency. The FVTD RCS data using the Gaussian pulse are compared to MoM RCS results in Figure 35. The negligible differences are in the nulls and in the forward and backscatter directions. The greatest difference between the FVTD and MoM RCS results is approximately 1.5 dB as shown in Figure 36. To obtain the excellent results, a GPD for theta and phi are specified at 30.7 cells/ λ and 32.9 cells/ λ , respectively. Figure 37 shows the high correlation between the MoM and FVTD results. The nulls in the bistatic RCS results occur at the exact same angle. The cross-correlation shows the highest correlation at 180°, signifying the best correlation possible.

The VV polarization results for the ogive at 4.0 GHz are shown in Figure 38. The FVTD results are plotted against MoM results and show excellent agreement. The largest difference of 1.7 dB occurs at the monostatic angle of 0° for test OG5a. For the VV results, there is no phase shift which would result in a high cross-correlation just as for the HH results.

To complete the bistatic and monostatic results for the ogive, an example of the visualization of the results achievable from the FVTD time-domain code is shown in Figure 39. The plot is a contour slice of the scattered electric field from the ogive, for 4.0 GHz, in the xy plane. The plot is a gray-shade contour plot of the bistatic field with the angle of incidence at 0° (+z direction). The monostatic angle is 0° and the forward scatter angle is 180° (-z). The darkest areas represent the strongest field and the lightest areas correspond to the weakest fields. The strongest field in the contour plot corresponds to the peak in Figure 38 at approximately 140 degrees. As mentioned previously, the ogive is 3.4 wavelengths long at this frequency. The same number of wavelengths can be seen in the contours along the edge of the ogive.

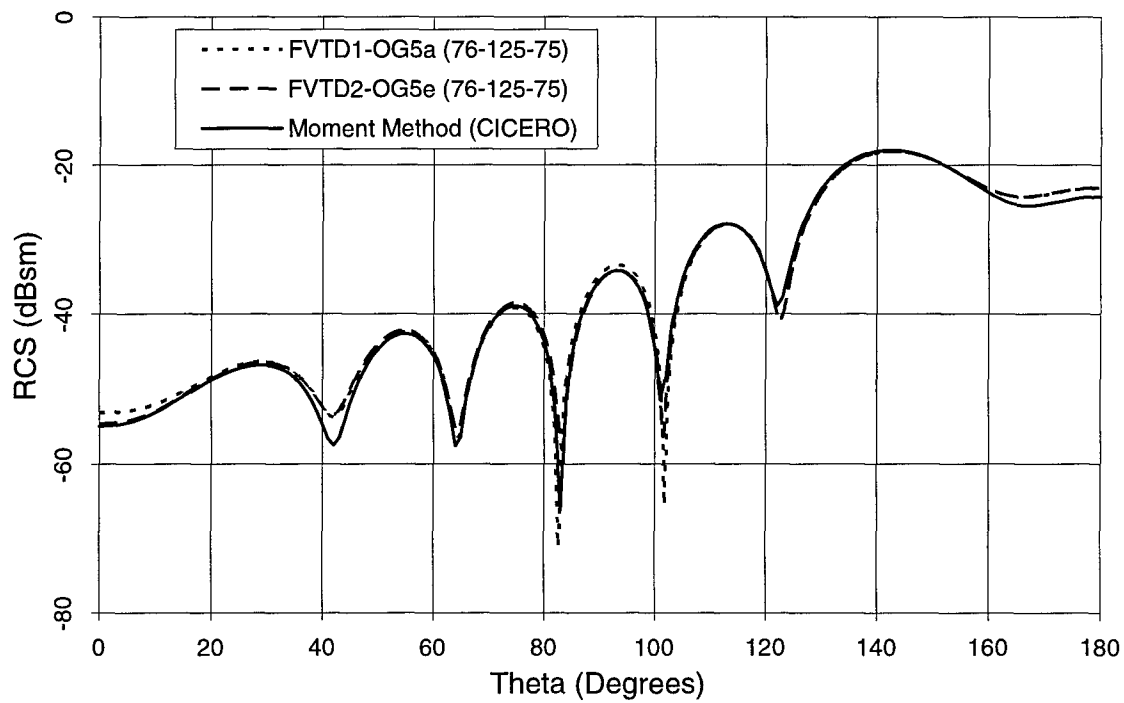


Figure 35: Ogive Bistatic RCS, 4.0 GHz, HH, Gaussian Pulse vs. Sinusoid Incident Wave

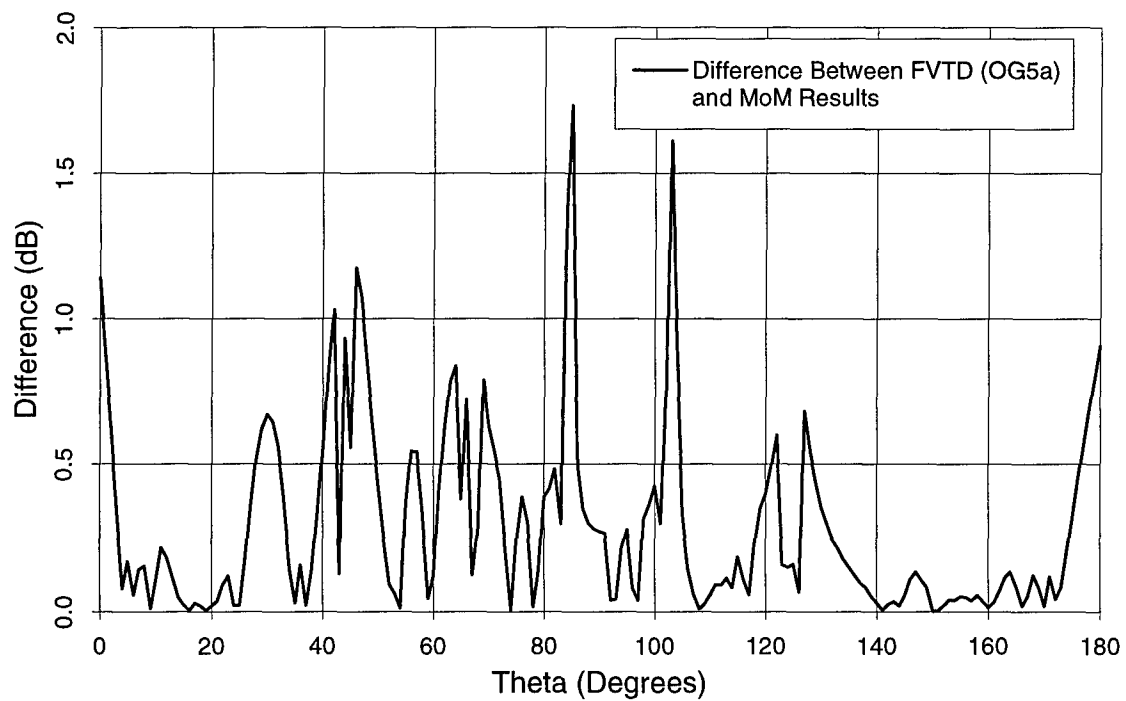


Figure 36: Ogive Bistatic RCS, 4.0 GHz, HH, Difference Between RCS Results

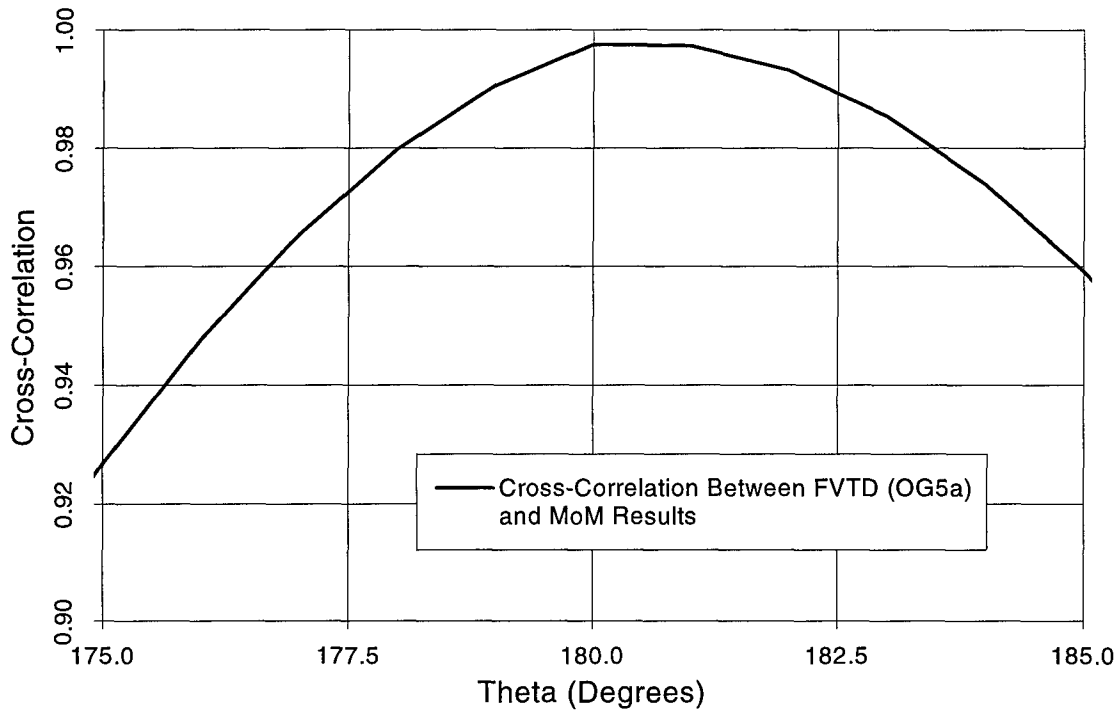


Figure 37: Ogive Bistatic RCS, 4.0 GHz, HH, Cross-Correlation of FVTD and MoM RCS

Several important observations can be obtained from the contour plot of the electric field in Figure 39. The perfect symmetry of the contours about the z axis validates the computational accuracy for the scattered electric field. The fields in each half of the plot about the z axis are calculated separately. Any errors in the code, especially overlap regions in the grid, would create errors in the symmetry of the contour plot. The symmetry confirms the accuracy of the code.

The diffraction of the electromagnetic wave can also be seen at the tips of the ogive. In the backscatter region, 0° , a strong field exists. The grid must be accurately generated for the FVTD algorithm to correctly predict the diffraction at the tip. The incident field and the scattered electric and magnetic fields are implemented at cell centers and not cell faces or cell grid points. The grid points of the cells define the tip of the ogive, but if only the cell centers are viewed, the tip of the ogive appears to have a small blunt tip. This characteristic of the grid and

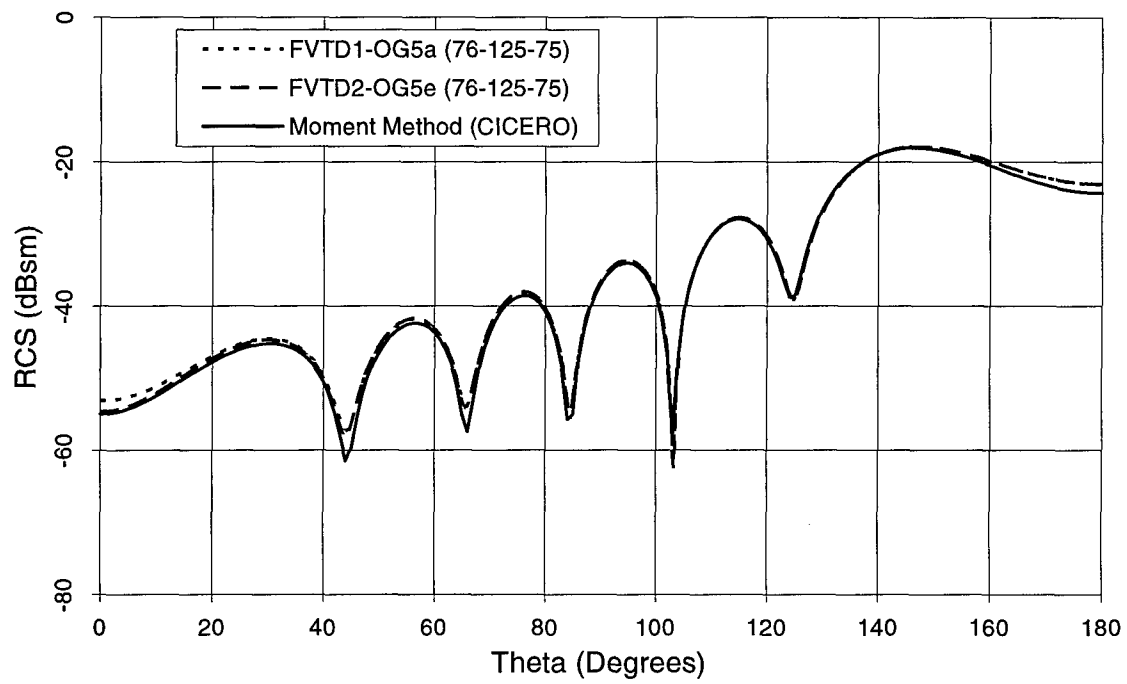


Figure 38: Ogive Bistatic RCS, 4.0 GHz, VV, Gaussian Pulse vs. Sinusoid Incident Wave

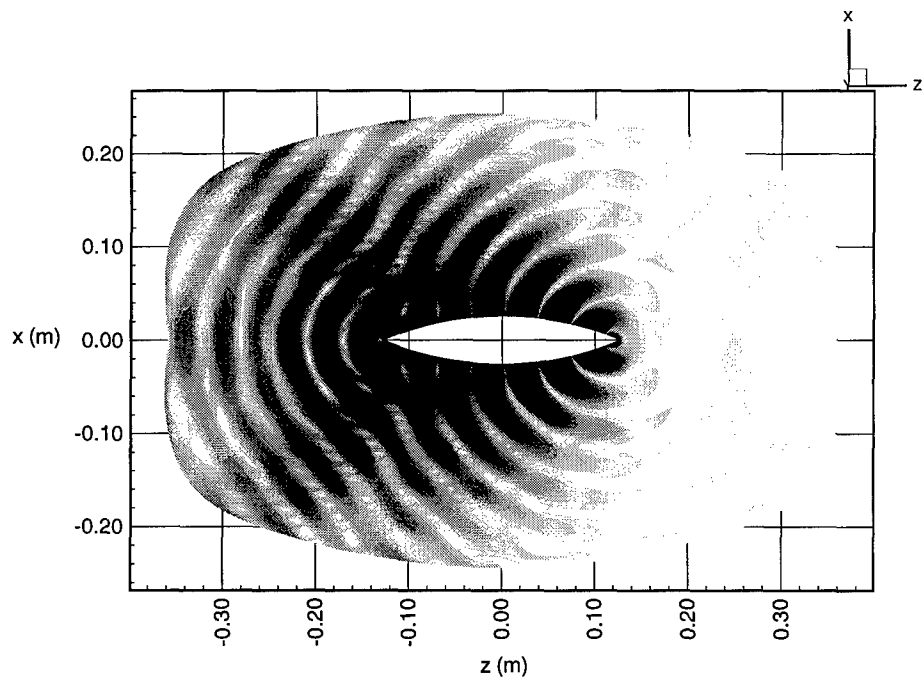


Figure 39: Ogive Bistatic Results, 4.0 GHz, Electric Field Contour Plot

the FVTD formulation demands that the cells at the tips of the ogive be extremely small to accurately represent the geometry and to accurately predict the diffracted fields.

To finish the ogive portion of the validation, two parameters are calculated to analytically represent the excellent RCS results for the scatterer using FVTD. The largest difference, in dB, and the mean-square error (MSE), explained in Chapter 3, provide metrics for establishing the difference and error between FVTD and MoM RCS data. Table 4 lists the largest dB difference and MSE for each polarization of each ogive test.

Table 4: MSE and Comparisons for the Ogive Tests

Test Number	Difference, HH (dB)	MSE, HH	Difference, VV (dB)	MSE, VV
OG1d	2.0	1.80E-9	0.8	5.90E-11
OG1e	3.0	1.79E-9	0.9	5.92E-10
OG1f	2.0	1.64E-9	0.7	7.38E-11
OG2a	3.0	1.82E-9	1.1	4.50E-10
OG2b	2.9	1.76E-9	1.1	4.34E-10
OG3X	2.5	N/A	N/A	N/A
OG4a	2.4	1.08E-5	1.9	8.52E-6
OG5a (4 GHz)	1.4	7.21E-8	1.1	4.74E-8
OG5e	1.4	7.86E-8	1.0	5.30E-8

The largest difference between bistatic and monostatic FVTD and MoM RCS results for the tests is 3.0 dB, HH, and 1.9 dB, VV. In general, the errors for VV are less than the errors for HH due to the additional nulls seen in the HH plots. The results showed that approximately 22-25 cells/ λ were required to obtain accurate results for the electrically small ogive. Test OG4a, the 9.0 GHz test, had a GPD of only 15.2 cells/ λ , illustrating the smaller GPD requirement for electrically larger objects. Test OG4a had the largest MSE and test OG1f, HH, had the smallest MSE. These MSE results are visually confirmed in the RCS plots. The small MSEs for all of the tests depict the excellent results obtained for the ogive using FVTD.

4.3 Cone-Sphere Electromagnetic Scattering Results

The RCS calculations for the cone-sphere provide further validation of the FVTD code and algorithm. The cone-sphere is a common RCS test body but the narrow cone portion and the sphere cap provide a unique body for analysis. At smaller frequencies, the scattering from the cone-sphere is a result of traveling waves along the narrow cone, creeping waves around the sphere cap, and diffraction from the tip. Excellent RCS results for the cone-sphere validate the FVTD code and algorithm for predicting complicated electromagnetic phenomena.

The test matrix for the cone-sphere computer simulations is shown in Table 5. Five tests were completed which include several subtests. The test numbers are constructed in the same method as the ogive test numbers. "CS" is used instead of "OG" to refer to the cone-sphere. The test numbers are used in the discussion of the results to easily reference the tests.

The electromagnetic scattering results for the cone-sphere are compared to MoM RCS results and experimental data for VV and HH polarization. The first cone-sphere tests, CS1X, are bistatic RCS results which analyze several grid sizes at 0.869 GHz using a sinusoid incident wave incident on the sphere section of the cone-sphere. The cone-sphere is two wavelengths long at 0.869 GHz. An incident angle of 0° corresponds to incidence on the cone-sphere along the axis of symmetry directly onto the sphere-cap. Tests CS2X are bistatic tests at 0.869 GHz with a sinusoid incident wave at 180° or tip-on incidence. Tests CS3X are tests for the monostatic calculations at 0.869 GHz. The monostatic RCS is computed every 10° from 0° to 180° and bistatic data completes the monostatic plot. The cone-sphere is not symmetric about the xy plane and therefore monostatic tests cannot be completed for only 0° to 90° as for the ogive. CS4a and CS5a are bistatic simulations for the cone-sphere at 3.0 GHz using a sinusoid incident wave at sphere-cap ($\theta=0^\circ$) and tip-on incidence ($\theta=180^\circ$), respectively.

Table 5: Cone-Sphere Test Matrix

Test Number	Incident Wave Type	Frequency (GHz)	Angle of Incidence	Grid Size
CS1a ¹	Sinusoid	0.869	0.0	50-73-45
CS1b ¹	"	"	"	50-39-35
CS1c	"	"	"	50-73-45
CS1d	"	"	"	50-39-35
CS2a ¹	Sinusoid	0.869	180.0	50-39-35
CS2b	"	"	"	50-39-35
CS3a	Sinusoid	0.869	10.0	50-39-35
CS3b	"	"	20.0	"
CS3c	"	"	30.0	"
CS3d	"	"	40.0	"
CS3e	"	"	50.0	"
CS3f	"	"	60.0	"
CS3g	"	"	70.0	"
CS3h	"	"	80.0	"
CS3i	"	"	90.0	"
CS3j	"	"	100.0	"
CS3k	"	"	110.0	"
CS3l	"	"	120.0	"
CS3m	"	"	130.0	"
CS3n	"	"	140.0	"
CS3o	"	"	150.0	"
CS3p	"	"	160.0	"
CS3q	"	"	170.0	"
CS4a ¹	"	3.0	0.0	73-141-81
CS5a ¹	"	3.0	180.0	73-141-65

¹The grid spacing at the surface (R direction) for these tests is approximately 200 cells/ λ . The surface grid spacing for all other tests is 400 cells/ λ .

The data in Table 6 contains the stability and time data for each cone-sphere test such as the CFL value, time step, number of time steps per period, total number of periods, total number of time steps, and total CPU time. The grid is structured to produce the largest time step as possible. For example, the tip GPD in the theta direction is 22.0 cells/ λ . Greater accuracy could be obtained with a larger GPD, but the trade-off between run time and accuracy justifies the spacing. As will be seen in the discussion, the results are excellent despite the larger spacing at

the tip of the cone-sphere. Due to the larger time step as compared to the ogive, the majority of the tests for the cone-sphere were completed on the DEC Alpha and SP-2 computing machines.

Table 6: Stability and Time Data for the Cone-Sphere Tests

Test Number	CFL	Δt (Seconds(c))	Time Steps/ Period	Total Periods	Total Time Steps	CPU Time ¹ (seconds)
CS1a ²	1.5	1.9553E-4	1766	4	7064	9797
CS1b ²	"	3.9937E-4	864	4	3456	2246
CS1c ²	"	1.7304E-4	3990	4	15960	22900
CS1d ²	"	2.9814E-4	1158	4	4632	3010
CS2a ²	"	3.9937E-4	864	4	3456	2248
CS2b ²	"	2.9814E-4	1158	4	4632	3072
CS3X ²	"	3.3789E-2	1158	4 ³	4632	2697
CS4a ²	"	4.8238E-5	2073	9	18657	126612
CS5a ²	"	5.3004E-5	1887	10	18870	102190

¹Cray 90 CPU time

²The RCS convergence check was used for these FVTD simulations

³Several monostatic tests required five periods to reach convergence

Table 7: Grid Point Densities for the Cone-Sphere Tests

Test Number	GPD: R at Surface	GPD: R at Outer Edge	GPD: θ at Body	GPD: θ at Tip	GPD: ϕ at Body	GPD: ϕ at Tip
CS1a	201	3.67	51.8	45.3	29.6	2367
CS1b	200	3.65	26.0	22.0	22.0	862
CS1c	402	2.64	51.8	45.3	29.6	2367
CS1d	401	2.56	25.9	22.0	22.0	862
CS2a	200	3.65	26.0	22.0	22.0	862
CS2b	401	2.56	25.9	22.0	22.0	862
CS3X	401	2.56	25.9	22.0	22.0	862
CS4a	233	9.3	30.0	26.2	16.3	2605
CS5a	233	9.3	30.0	26.2	14.0	2056

Table 7 shows the grid point densities (GPD) in each direction for each cone-sphere test.

Again, the GPD is defined as the number of finite-volume cells per wavelength, λ , and must be considered when generating a grid for a scatterer. As explained in Chapter 3, the spacing of the

cells in the radial direction increases as the distance from the surface of the scatterer increases. Therefore, the grid point density is much larger at the surface as compared to the outer edge of the grid. As can be seen in the table, the GPD varies from 200 to 401 cells/ λ at the surface and from 2.56 to 9.3 cells/ λ at the outer edge of the grid for the cone-sphere grid. The outer edge of the grid is three wavelengths from the surface of the scatterer for every simulation. The GPD in the θ direction is approximately the same at the sphere/cone junction and the cone tip. The GPD for the tests in the ϕ direction is the smallest at the sphere/cone junction and the largest at the tip, just as for the ogive.

4.3.1 Cone-sphere Bistatic RCS Results for 0.869 GHz, Sphere-Cap Incidence

Two bistatic tests at 0.869 GHz are discussed for the cone-sphere. For the first group of tests, CS1X, the sinusoid incident wave is incident at 0° , or sphere-cap incidence. The second group of tests, CS2X, is for an incident wave tip-on. Two different grids were generated for the cone-sphere. The grid size, (50-73-45), is identical for both grids, but the grid spacing in the radial direction is different at the surface. For the first grid, the spacing is 200 cells/ λ at the surface and for the second grid, the spacing is 400 cells/ λ at the surface.

For the group of tests with sphere-cap incidence, both grids were tested along with two different grid sizes. In Figure 40, the results using a coarse grid with 200 cells/ λ spacing is shown. Figure 40 shows that the forward scattering from the tip is not accurate. This proves that this grid spacing at this frequency is not sufficient. The diffraction from the tip is not correctly computed with this grid spacing. A finer grid in the theta and phi directions also does not improve the results in the forward scattering direction as shown with test CS1a. An increase in the spacing in the radial direction, tests CS1c and CS1d, as shown in Figure 41 greatly improves

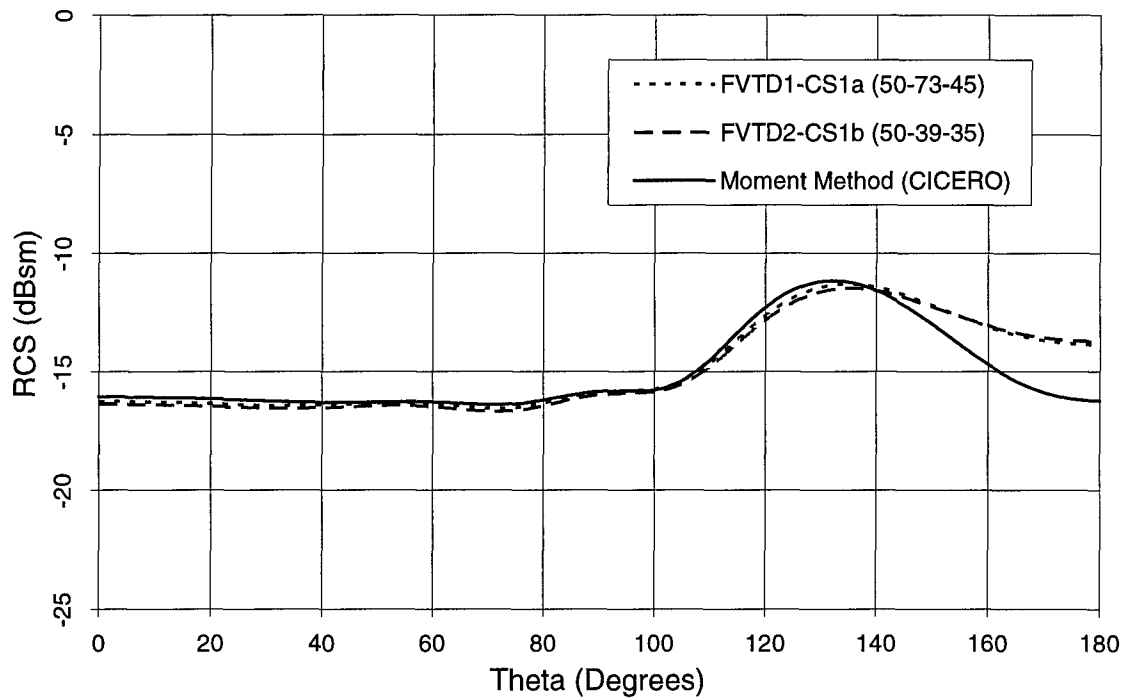


Figure 40: Cone-Sphere Bistatic RCS, 0.869 GHz, VV, Sphere-Cap Incidence, Coarse Grid

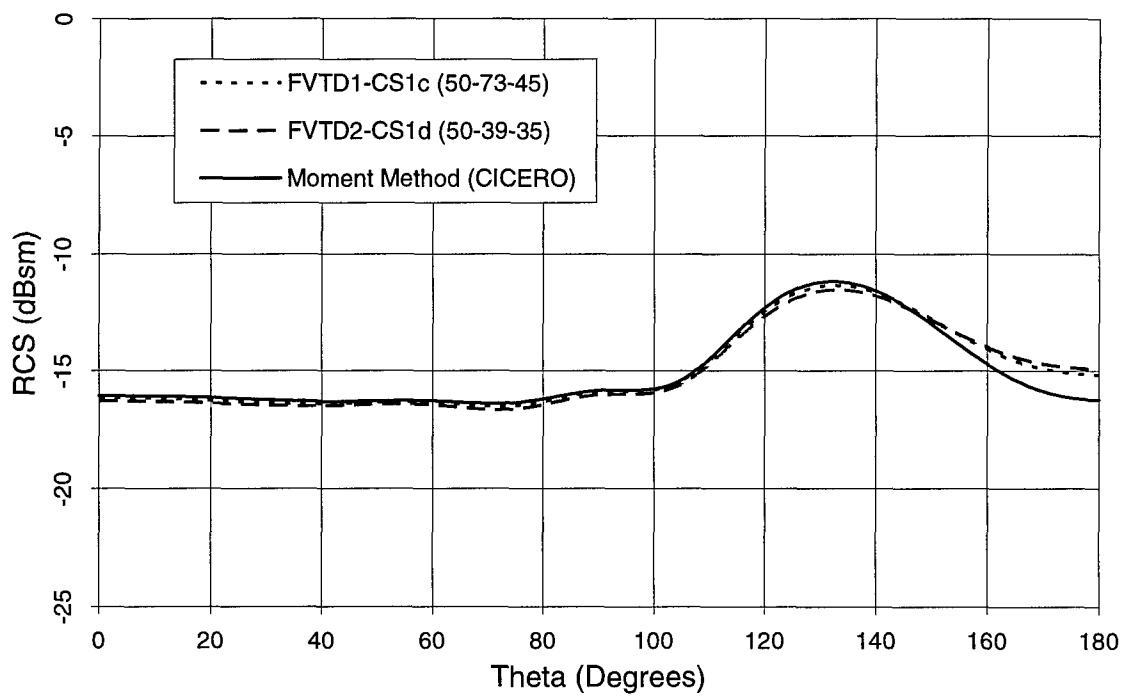


Figure 41: Cone-Sphere Bistatic RCS, 0.869 GHz, VV, Sphere-Cap Incidence, Fine Grid

the forward scattering region. The surface GPD can be decreased to 22.0 cells/ λ , but the GPD at the surface in the radial direction needs to be high at this frequency (400 cells/ λ). The results for test CS1c are slightly closer (<0.5 dB) to the MoM results than the CS1d results. The small difference can be considered negligible; therefore, grid convergence can be assumed for the smaller grid due to the computer run time saved. The computer run time saved with the smaller grid is approximately a factor of seven (22900 seconds (CS1c) vs. 3010 seconds (CS1d)). Due to the time step increase and the lower run time, test CS1d is considered sufficient and provides a very close computation to that obtained with the finer grid and to the MoM RCS results.

In Figure 42, the difference between test CS1c and the MoM RCS results are shown after the phase is taken into account as discussed in Chapter 3. A difference of approximately 0.1 dB is shown for the first 40 degrees in the backscatter direction. This difference is considered negligible in the calculations of RCS data. The phase difference for this bistatic data is not as critical as for the ogive RCS data. No deep nulls, which can provide erroneous error calculations, occur in the results. As can be seen in the plot, no more than 0.98 dB separates the FVTD RCS results from the MoM RCS results. The greatest difference occurs in the forward scatter region from the tip. Again, the tip is the most difficult geometric characteristic of the cone-sphere to accurately compute RCS data. For the ogive, the most significant errors occurred at the tips. The same trend is seen here with the cone-sphere.

The cross-correlation between the FVTD (CS1c) and MoM RCS results is shown in Figure 43. The maximum correlation occurs at 180° which illustrates the excellent correlation between the two sets of data. The steep slope of the cross-correlation curve signifies that no phase shift exists. Phase shifts tend to level the curve at the peak or shift the peak to either side of 180° . The Fourier transforms of both RCS curves illustrate the excellent agreement between the FVTD and MoM RCS results.

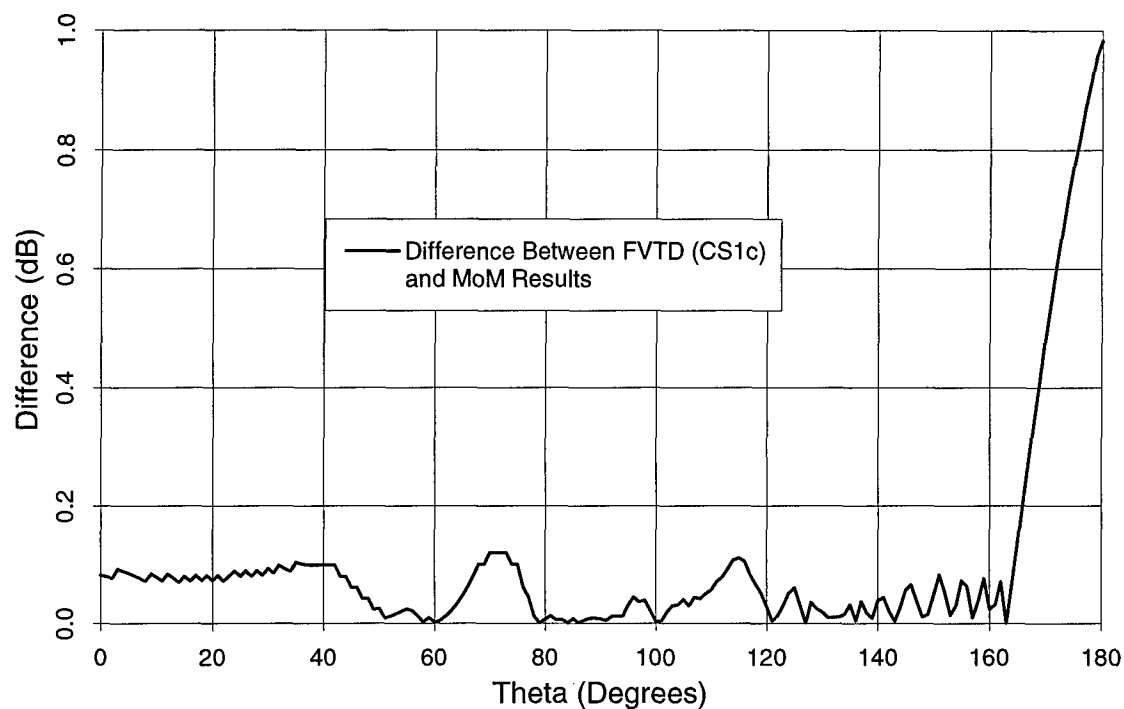


Figure 42: Cone-Sphere Bistatic RCS, 0.869 GHz, VV, Difference Between RCS Results

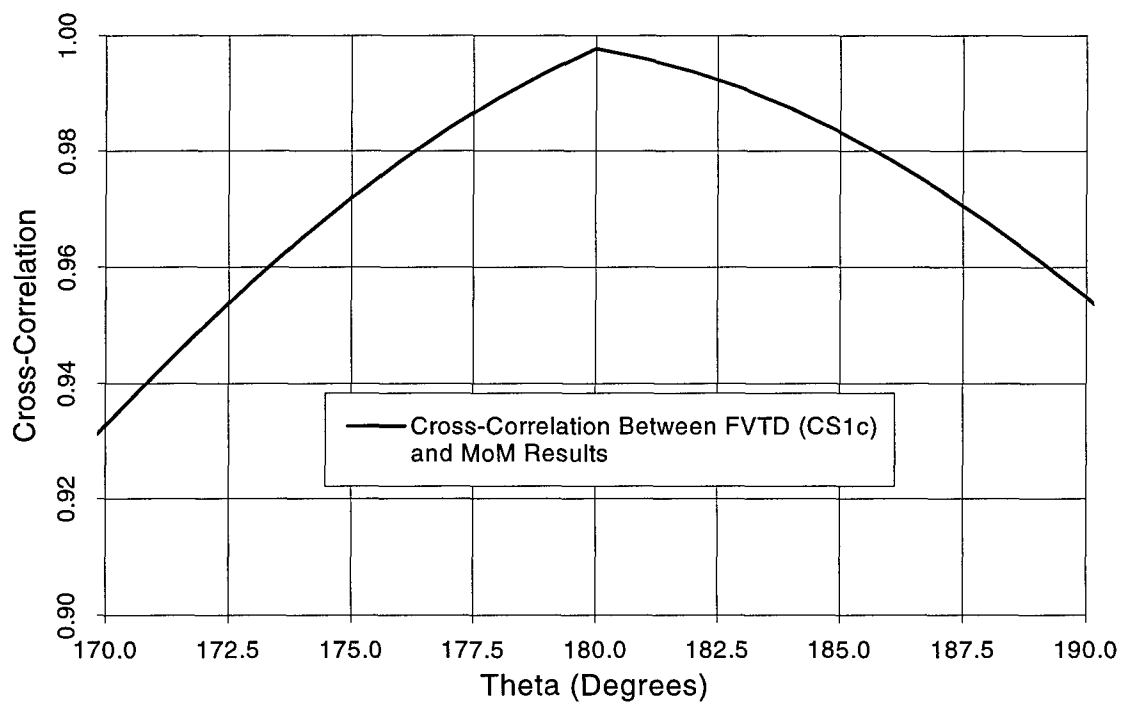


Figure 43: Cone-Sphere Bistatic RCS, 0.869 GHz, VV, Cross-Correlation of RCS Data

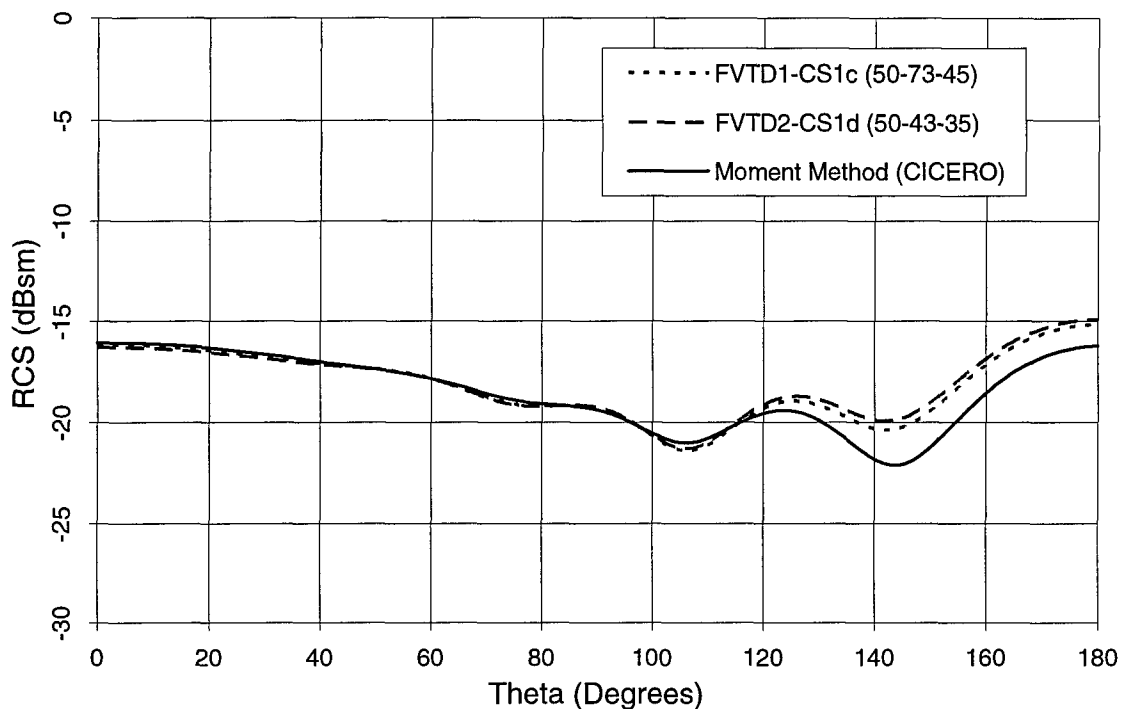


Figure 44: Cone-Sphere Bistatic RCS, 0.869 GHz, HH, Sphere-Cap Incidence, Fine Grid

Similar results were obtained for the cone-sphere for 0.869 GHz for HH polarization. Figure 44 plots the FVTD results for HH against MoM RCS data. The greatest difference of 2.5 dB occurs in the null at 143°. The FVTD results for HH miss the nulls by several dB for some bistatic plots. The same result was seen for the ogive at 1.18 GHz for HH in Figure 19.

4.3.2 Cone-Sphere Bistatic RCS Results for 0.869 GHz, Tip-On Incidence

FVTD RCS data for tip-on incidence were obtained in test OG2X. The incidence wave propagates toward the cone-sphere from 180°. The accuracy of the bistatic results is dependent on the correct calculation of creeping and traveling waves and diffraction at the tip. The creeping waves travel behind the sphere and the creeping waves travel along the smooth surface of the cone. The VV and HH polarization cases are shown in Figures 45 and 46, respectively.

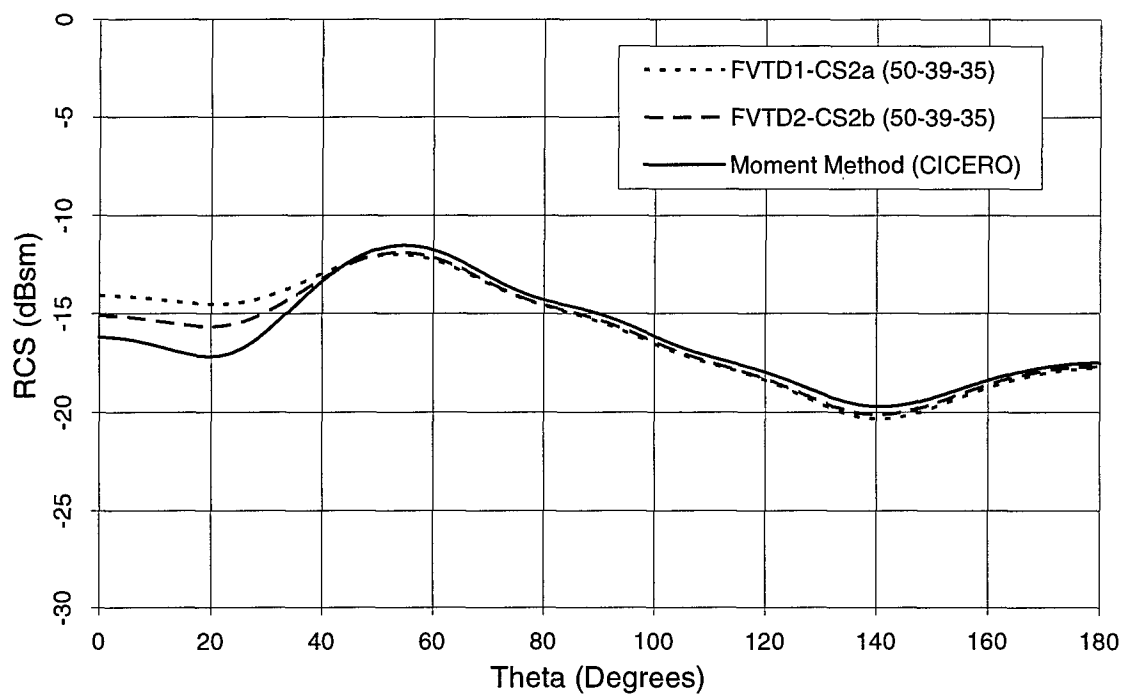


Figure 46: Cone-Sphere Bistatic RCS, 0.869 GHz, HH, Tip-On Incidence

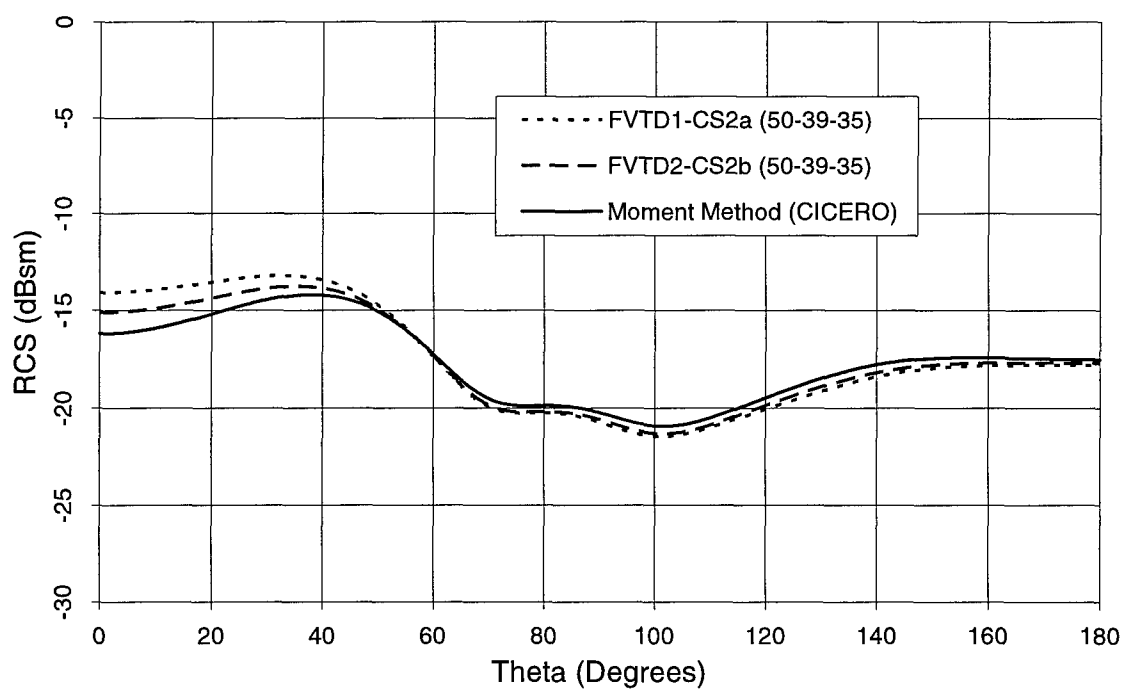


Figure 45: Cone-Sphere Bistatic RCS, 0.869 GHz, VV, Tip-On Incidence

The finer grid, CS2b, produces much better results than the grid with the coarser spacing (CS2a) at the surface. The forward scatter results ($\theta=0^\circ$) are only accurate if the fine grid is used (CS2b). Recall that the fine grid has a spacing of $400 \text{ cells}/\lambda$ at the surface. The forward scatter region is dependent on the accurate calculation of creeping waves as shown in the plot.

4.3.3 Cone-sphere Monostatic RCS Results for 0.869 GHz

The monostatic RCS data for the cone-sphere, HH polarization, is plotted in Figure 47. The FVTD and MoM RCS results match each other much closer than they match the empirical data. The author of reference [55] states that errors exist in the experimental data, especially in the forward scatter area (120° - 180°). The MoM and FVTD results are almost identical for every location except for several of the bistatic-to-monostatic approximation junctions. The agreement between the techniques suggest that the empirical data is not correct from 120° - 180° .

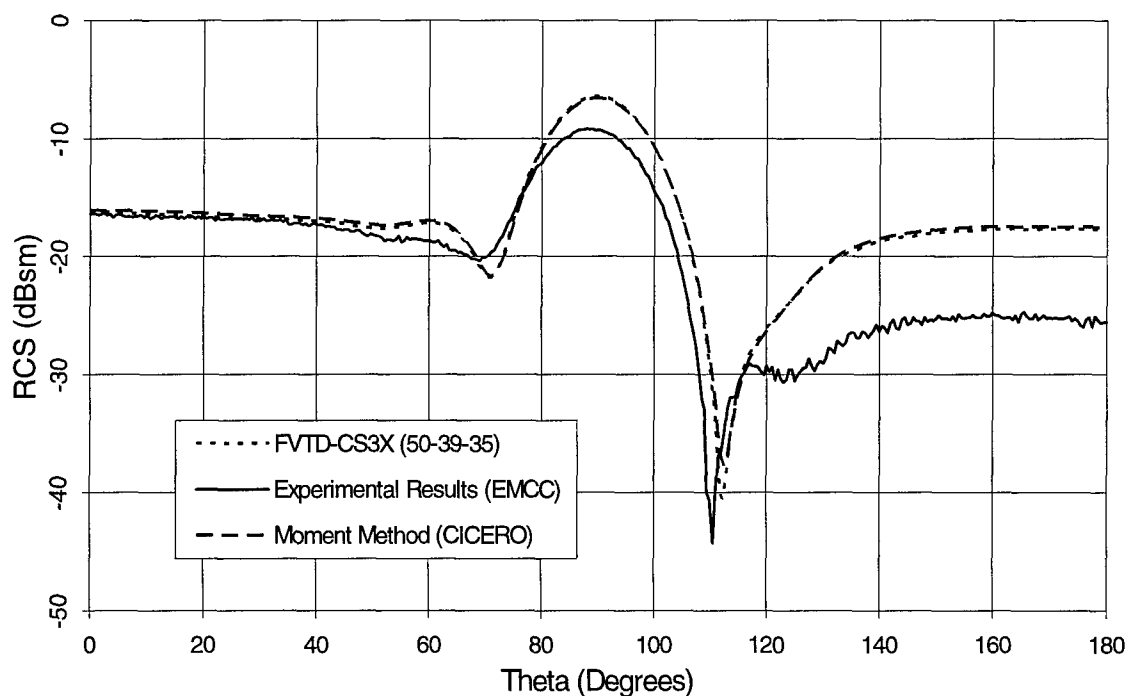


Figure 47: Cone-Sphere Monostatic RCS, 0.869 GHz, HH

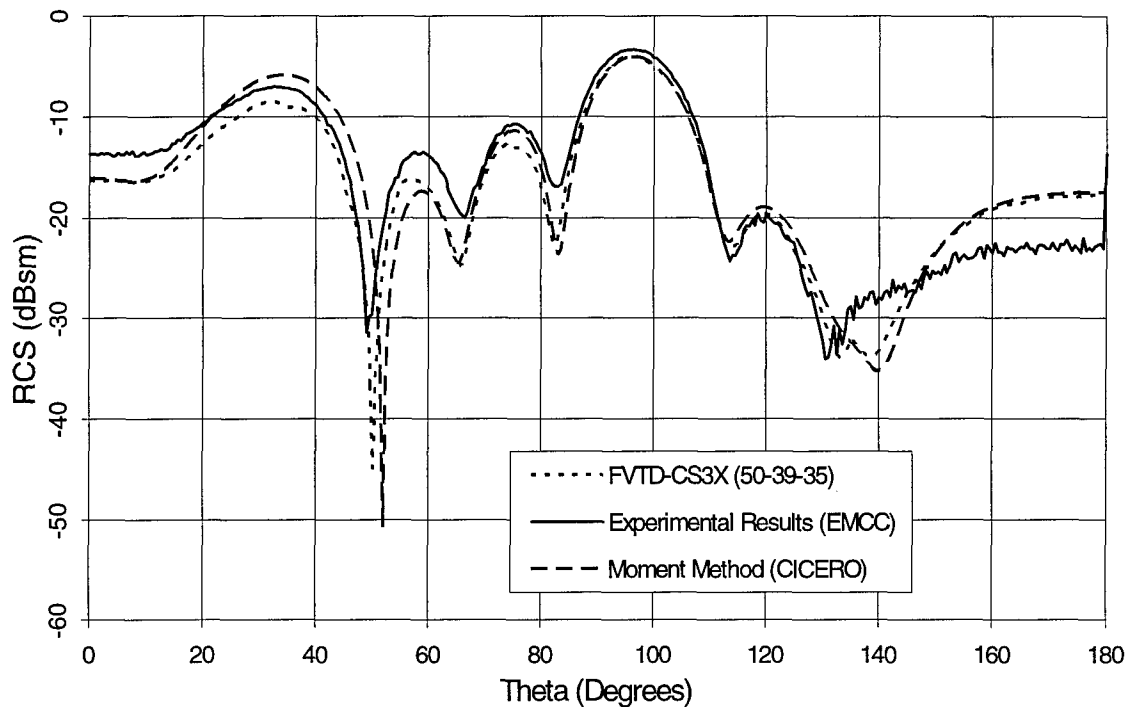


Figure 48: Cone-Sphere Monostatic RCS, 0.869 GHz, VV

Monostatic RCS results for VV polarization for the cone-sphere are shown in Figure 48. The FVTD results closely match the experimental and MoM RCS results. For certain regions, the FVTD results are closer to the MoM results than the experimental results. The small fluctuation in the FVTD curve at 135° shows the limitation of the bistatic-to-monostatic approximation. As the monostatic curve obtains more oscillations, as for higher frequencies, the monostatic simulations every 10° may not be sufficient. The simulations may have to be performed every 5° to accurately obtain the oscillations in the curve.

The FVTD results for the cone-sphere at 0.869 GHz using a sinusoid incident wave were excellent when compared to MoM results. The results illustrate that for electrically small objects, the FVTD algorithm correctly predicts diffraction, creeping waves, and traveling waves. The following results are for a higher frequency, 3.0 GHz.

4.3.4 Cone-sphere Bistatic RCS Results for 3.0 GHz

In this section, the bistatic RCS results for the cone-sphere for 3.0 GHz are presented. Test CS4a and CS5a are the sphere-cap and tip-on incidence tests, respectively. The length of the cone-sphere is 6.9 wavelengths at this specific frequency. The cone-sphere at this frequency is in the optical region, just as the ogive was for 9.0 GHz. The electromagnetic phenomena, such as diffraction, creeping waves, and traveling waves, are local and the test time, in periods, is not as long as for lower frequencies.

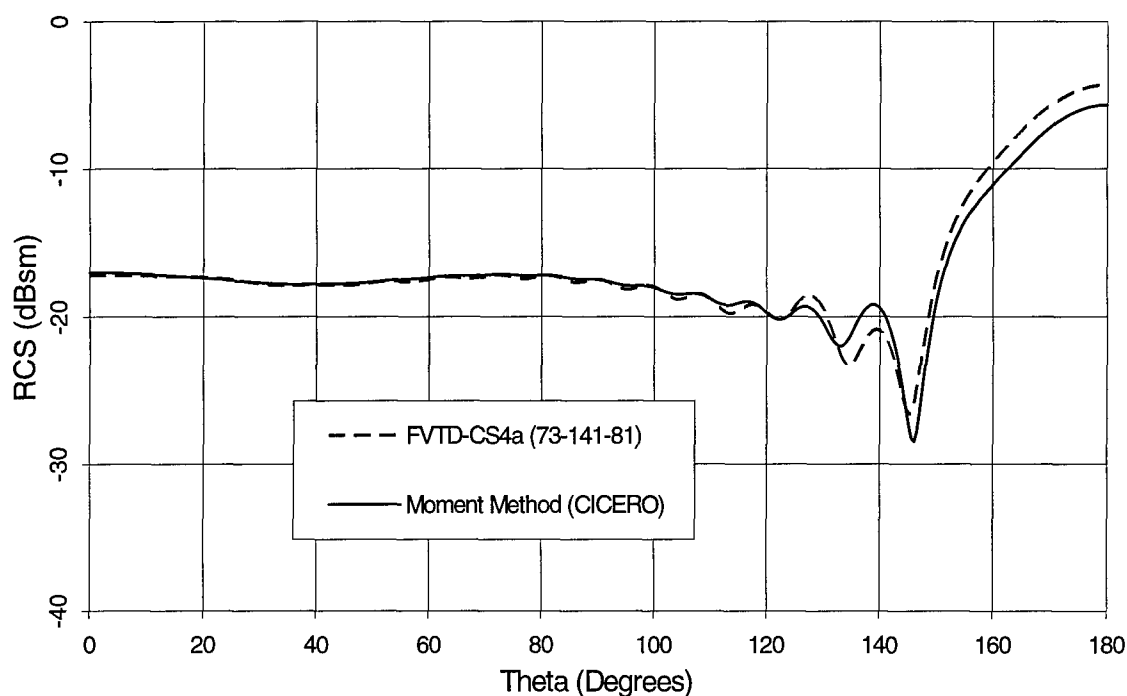


Figure 49: Cone-Sphere Bistatic RCS, 3.0 GHz, HH, Sphere-Cap Incidence

The HH polarization case for test CS4a is shown in Figure 49. The FVTD RCS results are plotted against MoM CICERO data. The accuracy of the VV polarization results was almost identical. The MoM and FVTD RCS data differ by no more than 1.4 dB. The largest difference occurs in the forward scatter direction at the tip ($\theta=180^\circ$) and in the nulls.

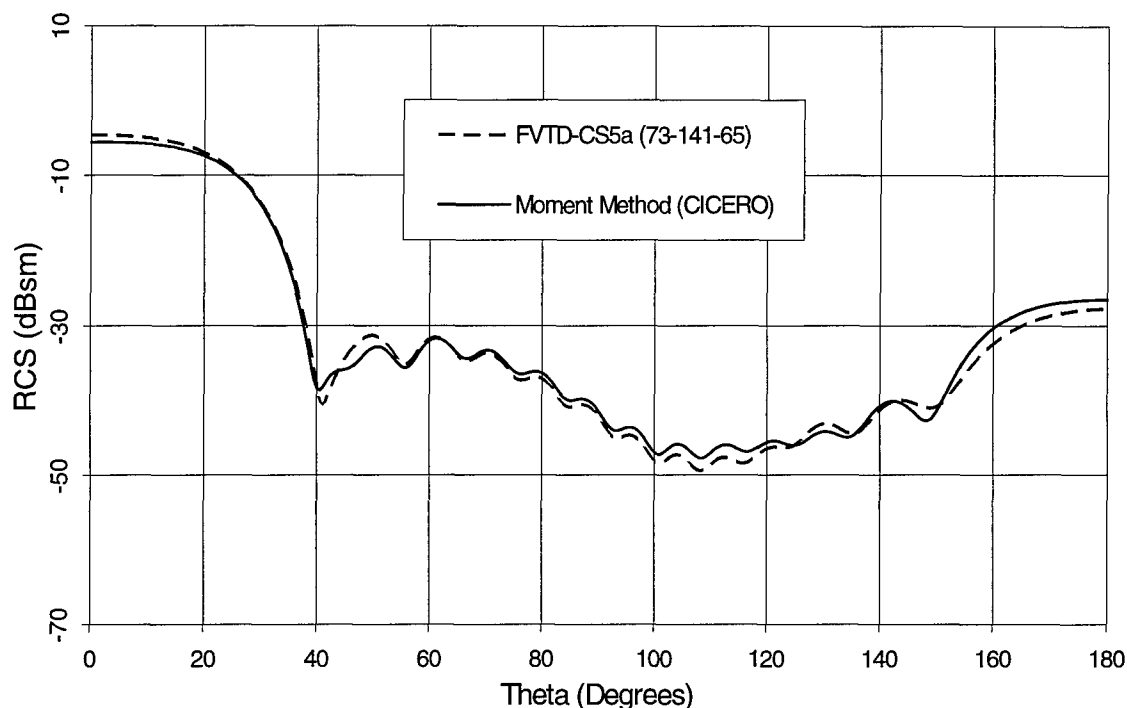


Figure 50: Cone-Sphere Bistatic RCS, 3.0 GHz, VV, Tip-On Incidence

Figure 50 is the VV polarization result for tip-on incidence (CS5a). The FVTD results are almost identical to the MoM RCS results. Small differences of less than 1.2 dB occur in several of the oscillations but are negligible. The FVTD RCS data for the forward scatter region, from the sphere-cap ($\theta=0^\circ$), differ by 1.0 dB from the MoM data. The FVTD data for the backscatter region ($\theta=180^\circ$) from the tip differ by 1.2 dB from the MoM RCS results. As seen with the ogive, errors in the FVTD RCS calculations first occur at the tips. An increase in the GPD will better the RCS results but the computer run time will be longer. The amount of error permissible determines the shortest run time and GPD required for the tip of a scattering object.

To complete the analysis of the cone-sphere, the same metrics are calculated for the cone-sphere as for the ogive to illustrate the excellent RCS results obtained using FVTD. The largest difference, in dB, and the mean-square error (MSE) are metrics for presenting the

difference and error between FVTD and MoM RCS results. Table 8 lists the largest dB difference and MSE for each polarization of each cone-sphere test.

Table 8: MSE and Comparisons for the Cone-Sphere Tests

Test Number	Difference, HH (dB)	MSE, HH	Difference, VV (dB)	MSE, VV
CS1a	3.0	3.11E-5	2.3	2.36E-5
CS1b	3.2	3.77E-5	2.4	2.76E-5
CS1c	1.2	2.80E-6	1.0	2.16E-6
CS1d	1.6	5.54E-6	1.2	4.14E-6
CS2a	2.4	2.99E-5	2.0	3.09E-5
CS2b	1.3	5.27E-5	1.0	4.53E-6
CS3X	0.5	N/A	N/A	N/A
CS4a	1.4	3.54E-4	N/A	N/A
CS5a	N/A	N/A	2.1	2.40E-4

The largest difference, in dB, between bistatic FVTD and MoM results for tests CS1X-CS2X is 3.2 but this was for the grid with the coarse spacing (200 cells/ λ) at the surface. For the results using the finer grid at the surface (400 cells/ λ), the greatest error is 1.6 dB. For the monostatic results, the largest difference for HH is 0.5 dB. The greatest error for the 3.0 GHz tests is 2.1 dB. The errors for VV are less than for HH just as for the ogive RCS results. Test CS1b had the largest MSE and test CS1c had the smallest MSE. Based on the plots, test CS4a visually had the smallest error and the MSE data confirm this observation. The metrics listed in the table illustrate the excellent FVTD results obtained for the cone-sphere.

4.4 Summary

The electromagnetic scattering and RCS results for the EMCC-defined RCS test bodies, ogive and cone-sphere, were presented. Bistatic and monostatic RCS results were compared to

MoM and empirical RCS results. Grid convergent tests were completed which analyzed the variation of the size of the grid in each coordinate direction (R, θ, ϕ). Grid point densities (GPD) were studied to arrive at an optimum GPD in each direction.

For the ogive, the bistatic results at 1.18 GHz required a grid spacing of 510 cells/ λ at the surface in the radial direction. The surface spacing in the theta and phi directions had to be at least 22 cells/ λ . The bistatic-to-monostatic approximation gave monostatic results for the ogive that differed from MoM RCS data by no more than 2.5 dB for HH polarization. The FVTD RCS results for VV were similar when compared to MoM and experimental RCS data.

The ogive bistatic RCS for 9.0 GHz differed by no more than 2.4 dB. The largest differences occurred in the forward and backscatter regions. The electrically larger ogive at this frequency required a lower PEC surface boundary condition GPD of 200 cells/ λ and a surface GPD of 15.2-18.8 cells/ λ . The simulation time was longer but the number of periods required for convergence was less than for lower frequencies.

A Gaussian pulse and sinusoid incident wave produced almost identical results for 1.0, 2.0, 3.0, and 4.0 GHz. Computational issues such as numerical dispersion and the distance of the outer boundary from the scatterer for different frequencies were critical when using the Gaussian pulse incident wave. The Gaussian pulse incident wave provides results for multiple frequencies but the simulation time is longer than for a test using a sinusoid incident wave.

The bistatic and monostatic cone-sphere results confirmed the accuracy and grid requirements for the ogive. For 0.869 GHz, the surface grid spacing required was 22-25 cells/ λ . The spacing in the radial direction had to be 400 cells/ λ to accurately compute diffraction and traveling and creeping waves. The results differed by no more than 1.6 dB from the MoM results and 0.5 dB from the empirical results. The bistatic RCS for 3.0 GHz differed by no more than 2.1 dB from the MoM results.

5 Conclusions and Recommendations

5.1 Conclusions

The objectives of this research were to

- modify the Wright Lab FVTD code to analyze the electromagnetic scattering from PEC three-dimensional objects
- validate the characteristic-based FVTD formulation by using the modified code to analyze the electromagnetic scattering from the three-dimensional objects, ogive and cone-sphere, and compare the FVTD results to MoM results and empirical data published by the EMCC.

Both objectives were met. The original code was modified to analyze scattering from closed-surface perfect electric conductor (PEC) 3-D objects using either a Gaussian pulse or a sinusoid incident wave. The specification of the direction and polarization of the incident wave was added to give monostatic and bistatic results. An RCS convergence check was also programmed, used with a sinusoid, which ends the simulation after the transients diminish and the bistatic RCS values are within 0.1 dB of the RCS values calculated during the previous period. A threshold check used with a Gaussian pulse was programmed to end the simulation once the scattered field is 140 dB below the peak of the Gaussian pulse. A bistatic-to-monostatic RCS approximation saves computer simulation time by a factor of nearly 40 for computing monostatic data.

Using the FVTD algorithm, the bistatic and monostatic RCS were calculated and compared to MoM and empirical results in this research. A meticulous grid study was performed for the ogive to determine the grid parameters required to obtain accurate results. The conclusions drawn from the ogive grid were applied to the generation of the grid for the cone-

sphere to obtain accurate results. The modified code can be used to analyze the scattering from other closed-surface, single-zone, 3-D objects if an appropriate grid is generated.

5.1.1 Ogive RCS Results

The FVTD results for the ogive were excellent when compared to MoM results and empirical data. Several bistatic and monostatic tests were completed for the ogive at 1.18 GHz. The bistatic tests showed that a grid point density (GPD) on the surface of approximately 22-32 cells/ λ produced the best results. Shankar reports a GPD requirement of 30-50 cells/ λ for objects with edges or tips, like the ogive, for his second-order accurate algorithm [42]. The lower GPD requirement for Shang's Wright Lab fourth-order accurate FVTD code is consistent with the order of accuracy of the algorithms. It was critical for the spacing in the radial direction to be close to 400-510 cells/ λ to obtain accurate results for lower frequencies but could be reduced to 200 cells/ λ for higher frequencies (9.0 GHz). The bistatic tests for 1.18 GHz differed from the MoM results by no more than 3.0 dB for HH polarization and 1.1 dB for VV polarization. The FVTD calculations for the monostatic tests were compared to empirical results in addition to MoM results. The FVTD results are within 2.5 dB of the MoM monostatic values and within 3.1 dB of the empirical results.

The ogive is one wavelength long at 1.18 GHz. The small electrical size of the ogive at this frequency dictates that electromagnetic phenomenon such as traveling waves have to be calculated accurately (≤ 3.0 dB). Diffraction from the tip of the ogive also contributes to the RCS. The small spacing in the radial direction (approximately 400-510 cells/ λ) is required to accurately compute the electromagnetic scattering due to these interactions. As the GPD decreases, the errors in the RCS occur first in the backscatter and forward scatter direction as would be expected because of the diffraction at the tips of the ogive.

Two additional tests were completed for the ogive at 1.18 GHz. The Gaussian pulse incident wave used for the two tests placed the frequency of interest near the center of the pulse BW and near the edge of the usable BW of the pulse. Both tests showed that the entire usable BW of the pulse will provide results almost identical to those of the sinusoid incident wave.

The RCS was calculated for the ogive at 9.0 GHz. For the 9.0 GHz test, the surface grid spacing was decreased to 15-19 cells/ λ . The results were excellent and the forward and backscatter RCS values differed from MoM RCS results by no more than 2.4 dB. The grid spacing in the radial direction was 200 cells/ λ . As the electrical size of the object increases, traveling waves and diffraction contribute less to the RCS. These phenomena become local and the spacing does not have to be as large to accurately compute the propagation of the wave.

The relatively large GPD required at the surface in the radial direction as compared to the theta and phi directions is due to the geometry in addition to the calculation of specific electromagnetic phenomena. The curves and the tips of the ogive are defined by the surfaces of the finite-volume cells. For the FVTD formulation, the tangential scattered electric field based on the incident field is implemented at the cell centers and not on the cell faces or cell vertices. The tip of the ogive appears to have a small blunt tip if only the cell centers are viewed. This characteristic of the grid and FVTD formulation requires the cell size at the tips of the ogive to be extremely small to accurately represent the geometry. The geometry must be accurately represented to correctly calculate the diffraction occurring at the tips.

The tests for the ogive at several different frequencies show the length of time required to obtain accurate RCS data for an object using a sinusoid incident wave. Sufficient time, approximately two-four periods times the electrical length of the object, is required for the transients to diminish due to the turn-on of the incident wave. At lower frequencies, such as 1.18 GHz, convergence was not reached until four periods. For a higher frequency, 9.0 GHz, accurate

data was obtained for a length of time, in periods, equal to approximately three times the electrical length of the object.

The RCS of the ogive was obtained using a sinusoid and a Gaussian pulse incident wave. The Gaussian pulse is advantageous if multiple frequencies are desired and the simulation time is less than the total time for the individual sinusoid tests. Excellent results were obtained using the Gaussian pulse for 4.0 GHz and below. Simulation times and grid sizes limited the largest frequency which could be studied using a Gaussian pulse. The range of frequencies is limited for the Gaussian pulse due to the location of the outer edge of the grid for each frequency. Errors were identified for the 1.0 and 2.0 GHz in the forward scatter region due to the location of the outer edge of the grid (0.75λ and 1.5λ for 1.0 GHz and 2.0 GHz, respectively). The outer edge must be 2λ - 3λ to minimize the numerical reflections from the outer edge of the grid.

The metrics established to compare FVTD RCS results to MoM and empirical RCS data revealed excellent correlation. The greatest difference, in dB, between the FVTD and MoM RCS data was 3.0 dB and between empirical and FVTD data, 3.1 dB. The errors for VV were less than for HH due to the additional nulls in the HH curves. High correlation between FVTD and MoM RCS results were computed, but any phase shifts showed up as a shift of one or two degrees in the cross-correlation curve. The low MSEs (i.e. $5.90\text{E-}11$ to $1.08\text{E-}5$) also depicted the excellent results.

5.1.2 Cone-Sphere RCS Results

The cone-sphere results helped to confirm the ogive results. The cone-sphere, two wavelengths long at 0.869 GHz, is electrically small. Accurate results were obtained for a surface grid spacing of 22-26 cells/ λ , but the radial spacing for the PEC surface boundary

condition must be 400 cells/ λ to accurately consider diffraction, traveling waves, and creeping waves.

The bistatic FVTD results do not differ by more than 1.6 dB from the MoM results. The largest errors occurred at the tip of the cone-sphere. The results could be improved slightly with a finer grid, but the time step would be decreased resulting in a longer simulation time. The slight error is acceptable and justifiable if the simulation time is decreased. Excellent monostatic results were obtained using FVTD and differ by no more than 0.5 dB from the MoM results.

The bistatic RCS data was also obtained for the cone-sphere at 3.0 GHz using FVTD. Accurate data was obtained after 9 or 10 periods for the 6.9 wavelength object. The FVTD RCS calculations were within 2.1 dB of the MoM RCS data. Accurate results required a surface grid spacing of 14-26 cells/ λ and a radial spacing of 200 cells/ λ to accurately consider diffraction, traveling waves, and creeping waves. These grid point density requirements confirm the ogive conclusion that a lower grid point density is needed for electrically larger objects since diffraction, traveling waves, and creeping waves contribute less to the RCS.

5.1.3 FVTD Computational Issues

The experience gained using FVTD to solve electromagnetic scattering problems revealed that several important computational issues need to be considered to obtain accurate data. The issues arise because of the FVTD technique and numerical algorithm, boundary conditions, type of incident wave, and the electromagnetic scattering phenomena occurring at the surface of the object.

The numerical algorithm used for the flux evaluation, van Leer's kappa scheme (MUSCL approach), is third-order accurate. The Runge-Kutta technique used for the time integration is fourth-order accurate. These techniques give the code a potential high order of accuracy but the

accuracy is degraded if the grid is poorly constructed. A grid which is highly distorted or incongruent will produce computational errors. The grids incorporated grid stretching, such as hyperbolic tangent stretching, but extreme stretching will degrade the flux calculations. Further work could be done to calculate the minimum number of cells required in the radial direction. For this research, 50-83 cells were used in the radial direction but as few as 15-20 cells may be sufficient if the grid is properly constructed. This improvement would improve simulation times by a factor of two or three.

The grid must be properly constructed to obtain the best results from the first-order surface boundary condition. The radial lines at the surface of the scatterer should be approximately perpendicular to the surface. Several attempts were made to construct grids analytically but the grid lines were not perpendicular to the surface. These attempts produced poor results.

Another computational issue which is critical for the completion of the computer tests is the time step. The stability of the system of differential equations is related to the smallest cell size. The ogive and cone-sphere geometries produce converging grid lines at the tips resulting in extremely small cells. This characteristic for these geometries revealed a limitation of the explicit FVTD algorithm and available computing resources. The small time step, the large grid size, and the number of periods required to obtain accurate frequency data results in a longer simulation time. Accuracy in the backscatter and forward scattering regions must be sacrificed for a faster simulation time and smaller grid. If a large number of periods required for the test is large, such as 20-25 periods, the resulting computer simulation time is large on the Cray (i.e. 25-35 hours).

If the first-order boundary condition was improved, the size of the smallest grid cell could be increased and the resulting simulation time would decrease. The time step is dependent

on the cell size. Any research efforts that will permit larger cells relative to the wavelength will greatly increase the flexibility of the explicit algorithm and potential applications.

The initial transients produced from the sinusoid incident wave require that frequency data cannot be taken for several periods after the beginning of the test. The length of time is dependent on the electrical size of the object. The time required was found to be, in periods, two to four times the electrical length of the object. As the object increases in electrical size, the electromagnetic phenomena becomes more localized and less time, in periods, is required.

The electromagnetic phenomena which occurs from the surfaces of an ogive and cone-sphere provide validation for many computational codes. The smooth curved surfaces, tips, and diffraction points are surface characteristics which can pose difficulties for computing accurate scattering results. Based on the FVTD results for the ogive and cone-sphere, the electrical size of the object is critical when determining grid size and spacing. For a small object, $1-2\lambda$, the grid spacing can be 22-25 cells/ λ on the surface. The spacing in the radial direction must be 400-500 cells/ λ . For an object which is electrically larger ($7\lambda-8\lambda$), the surface grid spacing may be reduced to 15-19 cells/ λ , and the radial grid spacing can be decreased to approximately 200 cells/ λ . These findings are critical for the expansion of the code to studying electrically larger objects such as airfoils and aircraft shaped bodies. A grid must be generated which will incorporate these features for a particular frequency.

5.2 Suggested Areas for Further Research

The application of FVTD to the area of CEM is relatively new. The potential areas of future research are numerous and several areas are briefly discussed below.

5.2.1 Surface Boundary Condition

The first-order accurate boundary condition by Shang necessitates a very dense grid near the surface of the object. The third-order accurate Van Leer's kappa scheme used to calculate the fluxes through the faces of the cells and the fourth-order accurate Runge-Kutta scheme used for the time integration requires a grid density of approximately 15-30 cells/ λ . The first-order accurate surface boundary condition requires a grid density of at least 200 cells/ λ for objects containing tips such as the ogive and cone-sphere. An improvement in the surface boundary condition would greatly decrease the grid density required at the surface of the PEC object.

5.2.2 Radiation Boundary Condition

For the purpose of this thesis research, the compatibility condition implemented by Shang at the outer boundary of the computational domain was considered to be sufficient. The compatibility condition is not exact and the outer boundary must be placed at approximately three wavelengths from the surface of the object to prevent erroneous numerical reflections from significantly affecting the scattered field results. A more accurate radiation boundary condition similar to the perfectly matched layer (PML) boundary condition developed for FDTD would greatly reduce the number of cells in the computational space. The PML developed by Berenger [4] cannot be directly implemented in a characteristic-based FVTD formulation; however, several researchers have developed generalized PML theories which could possibly be implemented in the FVTD formulation [57].

5.2.3 Material Interfaces

For multi-layer dielectric surfaces to be analyzed, the boundary conditions at the interface between the two materials must be enforced. This boundary condition corresponds to a

jump in the characteristic, or eigenvalue, across the interface. Further research needs to be completed in this area.

5.2.4 Dielectric Materials

Dielectric materials are used as radar absorbing materials on wings and the fuselages of aircraft. The code requires further modification to analyze lossy dielectric materials.

5.2.5 Frequency-Dependent and Time-Dependent Materials

As stated in the first chapter, a potential advantage of FVTD is the ability to solve the electromagnetic wave propagation through frequency-dependent or dispersive materials and also time-dependent materials. A low-frequency or high-frequency CEM code cannot analyze these particular types of materials. Future research with these materials would provide an advantage for the FVTD code over other traditional CEM codes and techniques.

5.2.6 Anisotropic Materials

Code modifications for anisotropic materials could also be considered for further research. The constitutive parameters currently can only be specified as scalars. The constitutive parameters for anisotropic materials are tensors and the code requires modification for these types of materials. The generalized PML theories require the use of anisotropic materials in the PML. Development in this area would be a step toward implementing a PML for the radiation boundary condition.

RAM structures, such as honeycomb-filled structures, can exhibit anisotropic behavior [42]. Development work and advancement of the code for these materials would greatly improve the flexibility and capability of the code.

5.2.7 Multi-zoning for Complicated Objects

Objects coated with dielectric materials or frequency-dependent materials would require different grid structures for each material. A zone is required for each material or layer.

Complicated objects may also require multi-zones for the accurate generation of the grid.

Research needs to be conducted to expand the code for multi-zones.

5.2.8 Hybrid Techniques

As discussed previously, the small time step results in large computation time due to the tips of the ogive and cone-sphere. Shankar has considered using high-frequency techniques at edges and tips where the diffraction of the fields can be accurately computed. For electrically large objects, the diffraction can be considered a local phenomenon. Hybrid techniques could be researched to include techniques such as the geometrical theory of diffraction (GTD) or the uniform theory of diffraction (UTD) to compute the diffracted fields at tips and edges [3]. The time step would be increased and the resulting computation time would decrease dramatically.

5.2.9 Multi-discipline Applications

Multi-discipline applications could be studied utilizing the FVTD code after appropriate modifications. As discussed previously, the Euler equations of CFD and the Maxwell equations of CEM are both hyperbolic in nature. The body of the code which calculates the fluxes is practically identical for each application. The difference in the code between the two disciplines lies in the boundary conditions, pre-processing, and post-processing. CFD applications require the calculation of density and pressure values of the flow field around the airfoil and drag and pitching moment coefficient data [8]. With appropriate additions to the code, the aerodynamics

of an airfoil could be analyzed along with the electromagnetic scattering from the airfoil. The trade-offs between the two disciplines could be studied using the FVTD algorithm.

5.2.10 Code Optimization

The code is optimized for a vectorized machine, such as the Cray 90. Simulation times could be decreased if the code was optimized for a parallel machine such as the IBM SP-2 or Cray YMP. At higher frequencies, the grid size required and the multi-zones for dielectric-layered materials will require a parallel code for reasonable simulation times. Research is currently being performed to optimize the code for parallel computing machines [6,7], but further research has yet to be completed.

5.2.11 Summary

In conclusion, the FVTD code modifications completed in this thesis research permitted the FVTD algorithm and code to calculate the RCS of the ogive and cone-sphere. The FVTD code results were excellent as compared to RCS data obtained from the Moment Method (MoM) code, CICERO, and empirical results published by the Electromagnetic Code Consortium (EMCC). The comparisons validate the characteristic-based FVTD formulation and code for electromagnetic scattering problems.

Appendix A: FVTD Formulation and Numerical Algorithm

The finite-volume time-domain method is relatively new to computational electromagnetics (CEM). As discussed in the literature review, Shang and Shankar have performed the majority of the finite-volume time-domain (FVTD) effort in CEM. Included in this appendix is a summary of the characteristic-based FVTD formulation and numerical algorithm implemented by Shang in the FORTRAN code used for this thesis research. The FVTD formulation is a generic finite-volume scheme; however, the numerical technique is one of many schemes. The references by Shang and Shankar include numerous other numerical techniques, used with the generic finite-volume algorithm, to solve the Maxwell equations in the time domain. This summary is intended to aide the reader, without referencing numerous papers, in understanding the FVTD formulation and one specific numerical technique and how they are implemented to solve the Maxwell equations. It will also be helpful to others who desire to perform subsequent FVTD efforts with application to CEM. Several equations and paragraphs from Chapter 2 are repeated for convenience and readability.

A.1 Maxwell's Equations

The time-domain Maxwell equations, in differential form, are shown below and will be used in the development of the electromagnetic FVTD equations:

$$\text{Faraday's Law:} \quad \nabla \times \mathbf{E} = -\frac{\partial \mathbf{B}}{\partial t} \quad (A.1)$$

$$\text{Ampere's Law:} \quad \nabla \times \mathbf{H} = \frac{\partial \mathbf{D}}{\partial t} + \mathbf{J} \quad (A.2)$$

$$\text{Gauss's Electric Law:} \quad \nabla \cdot \mathbf{D} = \rho \quad (A.3)$$

$$\text{Conservation of Magnetic Charge:} \quad \nabla \cdot \mathbf{B} = 0 \quad (A.4)$$

where E : Electric field strength vector (V/m)
 D : Electric flux density vector (C/m²)
 H : Magnetic field strength vector (A/m)
 B : Magnetic flux density vector (Wb/m² or Tesla)
 J : Electric current density vector (A/m²)
 ρ : Electric charge density (C/m³)

The field strength vectors and the flux density vectors are related by the constitutive parameters. The constitutive parameters, the electric permittivity and magnetic permeability, are normally expressed as tensors. However, if the material is linear and isotropic the constitutive parameters are scalars and the constitutive relations become

$$\mathbf{D} = \epsilon \mathbf{E} \text{ and } \mathbf{B} = \mu \mathbf{H} \quad (A.5)$$

where ϵ : Electric permittivity (F/m)

μ : Magnetic permeability (H/m)

The four Maxwell equations are not independent of each other. The two divergence equations can be derived from the two curl equations using the conservation of charge relationship $\nabla \cdot \mathbf{J} = -\partial \rho / \partial t$ assuming that the material is linear and isotropic. The two divergence equations are not used in the FVTD calculations but can be used as a check on the predicted field response [18].

A.2 Maxwell's Equations in Conservation Form

For use in FVTD, the two curl Maxwell equations are cast in conservation form [37]. The conservation form is not required for the Maxwell equations but is required for the Euler equations of fluid dynamics. For the Euler equations, the conservation form conserves physical properties such as energy, mass, and momentum [8]. To take advantage of the same

computational tool, the Maxwell equations are also cast in conservation form. To place the two curl Maxwell equations in conservation form, the curl operations are carried out, the constitutive relations are implemented, and the result is given by [37]

$$\frac{\partial \mathbf{U}}{\partial t} + \frac{\partial \mathbf{F}}{\partial x} + \frac{\partial \mathbf{G}}{\partial y} + \frac{\partial \mathbf{H}}{\partial z} = -\mathbf{J} \quad (\text{A.6})$$

where

$$\mathbf{U} = \begin{bmatrix} B_x \\ B_y \\ B_z \\ D_x \\ D_y \\ D_z \end{bmatrix} \quad \mathbf{F} = \begin{bmatrix} 0 \\ -D_z / \epsilon \\ D_y / \epsilon \\ 0 \\ B_z / \mu \\ -B_y / \mu \end{bmatrix} \quad \mathbf{G} = \begin{bmatrix} D_z / \epsilon \\ 0 \\ -D_x / \epsilon \\ -B_z / \mu \\ 0 \\ B_x / \mu \end{bmatrix} \quad \mathbf{H} = \begin{bmatrix} -D_y / \epsilon \\ D_x / \epsilon \\ 0 \\ B_y / \mu \\ -B_x / \mu \\ 0 \end{bmatrix} \quad \mathbf{J} = \begin{bmatrix} 0 \\ 0 \\ 0 \\ J_x \\ J_y \\ J_z \end{bmatrix}$$

Equation (A.6) is a system of six linear equations with six unknowns (\mathbf{U} vector). The equations are linearly dependent; therefore, a characteristic-based scheme is developed to uncouple the six equations. The system constitutes a hyperbolic system of partial differential equations and an initial value problem [34]. The hyperbolic system possesses real eigenvalues and independent eigenvectors.

A.3 Coordinate Transformation

To analyze the scattering of various shapes including the ogive and cone-sphere analyzed in this thesis, a curvilinear coordinate transformation is required [37]. The transformation defines a one-to-one relationship between two sets of temporal and spatially dependent variables. The variables ξ , η , and ζ are used and are all functions of x , y , and z . Equation (A.6) after a coordinate transformation becomes [37, 38]

$$\frac{\partial \hat{\mathbf{U}}}{\partial t} + \frac{\partial \hat{\mathbf{F}}}{\partial \xi} + \frac{\partial \hat{\mathbf{G}}}{\partial \eta} + \frac{\partial \hat{\mathbf{H}}}{\partial \zeta} = -\hat{\mathbf{J}} \quad (\text{A.7})$$

where $\hat{U} = \frac{U}{V}$

$$\hat{J} = \frac{J}{V}$$

$$\hat{F} = \left(\frac{\partial \xi}{\partial x} F + \frac{\partial \xi}{\partial y} G + \frac{\partial \xi}{\partial z} H \right) \frac{1}{V}$$

$$\hat{G} = \left(\frac{\partial \eta}{\partial x} F + \frac{\partial \eta}{\partial y} G + \frac{\partial \eta}{\partial z} H \right) \frac{1}{V}$$

$$\hat{H} = \left(\frac{\partial \zeta}{\partial x} F + \frac{\partial \zeta}{\partial y} G + \frac{\partial \zeta}{\partial z} H \right) \frac{1}{V}$$

V is the Jacobian of the coordinate transformation and is given by [34]

$$V = \begin{vmatrix} \frac{\partial \xi}{\partial x} & \frac{\partial \xi}{\partial y} & \frac{\partial \xi}{\partial z} \\ \frac{\partial \eta}{\partial x} & \frac{\partial \eta}{\partial y} & \frac{\partial \eta}{\partial z} \\ \frac{\partial \zeta}{\partial x} & \frac{\partial \zeta}{\partial y} & \frac{\partial \zeta}{\partial z} \end{vmatrix} = \begin{vmatrix} \frac{\partial \xi}{\partial x} & \frac{\partial \eta}{\partial x} & \frac{\partial \zeta}{\partial x} \\ \frac{\partial \xi}{\partial y} & \frac{\partial \eta}{\partial y} & \frac{\partial \zeta}{\partial y} \\ \frac{\partial \xi}{\partial z} & \frac{\partial \eta}{\partial z} & \frac{\partial \zeta}{\partial z} \end{vmatrix} \quad (A.8)$$

For example, F is transformed to \hat{F} and is equal to [34]

$$\hat{F} = \begin{bmatrix} 0 & 0 & 0 & 0 & -\frac{1}{\epsilon V} \frac{\partial \xi}{\partial z} & \frac{1}{\epsilon V} \frac{\partial \xi}{\partial y} \\ 0 & 0 & 0 & \frac{1}{\epsilon V} \frac{\partial \xi}{\partial z} & 0 & -\frac{1}{\epsilon V} \frac{\partial \xi}{\partial x} \\ 0 & 0 & 0 & -\frac{1}{\epsilon V} \frac{\partial \xi}{\partial y} & \frac{1}{\epsilon V} \frac{\partial \xi}{\partial x} & 0 \\ 0 & \frac{1}{\mu V} \frac{\partial \xi}{\partial z} & -\frac{1}{\mu V} \frac{\partial \xi}{\partial y} & 0 & 0 & 0 \\ -\frac{1}{\mu V} \frac{\partial \xi}{\partial z} & 0 & \frac{1}{\mu V} \frac{\partial \xi}{\partial x} & 0 & 0 & 0 \\ \frac{1}{\mu V} \frac{\partial \xi}{\partial y} & -\frac{1}{\mu V} \frac{\partial \xi}{\partial x} & 0 & 0 & 0 & 0 \end{bmatrix} \begin{bmatrix} B_x \\ B_y \\ B_z \\ D_x \\ D_y \\ D_z \end{bmatrix} \quad (A.9)$$

\hat{G} and \hat{H} are the same as \hat{F} , except ξ is replaced with η and ζ , respectively. \hat{F} , \hat{G} , and \hat{H} are the flux vectors and represent the electric and magnetic flux densities at the faces of each finite-

volume cell of the discretized space in transformed curvilinear coordinates. The finite-volume formulation of Equation (A.7) and the calculation of the flux at each cell face will be discussed next.

A.4 Finite-Volume Formulation

Equation (A.7) is applied to every finite-volume cell in the grid. An integration is performed over each finite-volume cell:

$$\iiint_V \frac{\partial \hat{U}}{\partial t} dV + \iiint_V \left(\frac{\partial \hat{F}}{\partial \xi} + \frac{\partial \hat{G}}{\partial \eta} + \frac{\partial \hat{H}}{\partial \zeta} \right) dV = - \iiint_V \hat{J} dV \quad (A.10)$$

The divergence theorem is then applied to the second integral:

$$\iiint_V \frac{\partial \hat{U}}{\partial t} dV + \oint_S (\hat{F} + \hat{G} + \hat{H}) \cdot \mathbf{n} dS = - \iiint_V \hat{J} dV \quad (A.11)$$

where \mathbf{n} : Unit vector normal to the surface (ξ , η , and ζ for \hat{F} , \hat{G} , and \hat{H} , respectively)

S : Closed surface bounding the finite volume (m^2)

If the size of the cell is invariant with time and a finite-volume discretization is applied to the closed surface integral, then Equation (A.11) becomes [7]

$$\frac{\partial \hat{U}}{\partial t} V + \sum_{m=1}^6 (\hat{F}_{m\xi} + \hat{G}_{m\eta} + \hat{H}_{m\zeta}) = -J V \quad (A.12)$$

where $\hat{F}_{m\xi}$: Magnitude of the \hat{F} flux vector through face m in the ξ direction

$\hat{G}_{m\eta}$: Magnitude of the \hat{G} flux vector through face m in the η direction

$\hat{H}_{m\zeta}$: Magnitude of the \hat{H} flux vector through face m in the ζ direction

m : Index for the sides of the cell

V : Volume of cell, equal to the Jacobian of the coordinate transformation

Equation (A.12) is applied to every volumetric cell in the grid. The equation is the generic FVTD formulation. The components of \mathbf{U} are physically located at the center of the cell. The fluxes, \hat{F} , \hat{G} , and \hat{H} , are located on the surfaces of the cell and represent the tangential components of the electric and magnetic fields [8].

To evaluate the magnitude of the flux components through each face, the magnitude of the flux density in each coordinate direction is multiplied by the area of the face. The area of each face is evaluated by taking the dot product of the normal and the surface area vector, essentially the magnitude of the surface area vector [8]:

$$\hat{F}_{m\xi} = \hat{F}(\mathbf{ndS}_m \cdot \xi) \quad (A.13)$$

$$\hat{G}_{m\eta} = \hat{G}(\mathbf{ndS}_m \cdot \eta) \quad (A.14)$$

$$\hat{H}_{m\zeta} = \hat{H}(\mathbf{ndS}_m \cdot \zeta) \quad (A.15)$$

A representation of a finite-volume cell is shown in Figure A.1. The surface area vectors required in Equations (A.13-A.15) to calculate the magnitude of the fluxes through each face are calculated as follows, using face 2 as an example:

$$\mathbf{ndS}_2 = \eta dS_2 = \frac{1}{2}(\mathbf{R}_{63} \times \mathbf{R}_{72}) \quad (A.16)$$

where η : Unit vector normal to face 2

\mathbf{R}_{63} : Vector joining cell vertices 6 and 3

\mathbf{R}_{72} : Vector joining cell vertices 7 and 2

\mathbf{R}_{63} and \mathbf{R}_{72} are found using the vertices of face 2:

$$\mathbf{R}_{63} = (x_6 - x_3)\mathbf{i} + (y_6 - y_3)\mathbf{j} + (z_6 - z_3)\mathbf{k} \quad (A.17)$$

$$\mathbf{R}_{72} = (x_7 - x_2)\mathbf{i} + (y_7 - y_2)\mathbf{j} + (z_7 - z_2)\mathbf{k} \quad (A.18)$$

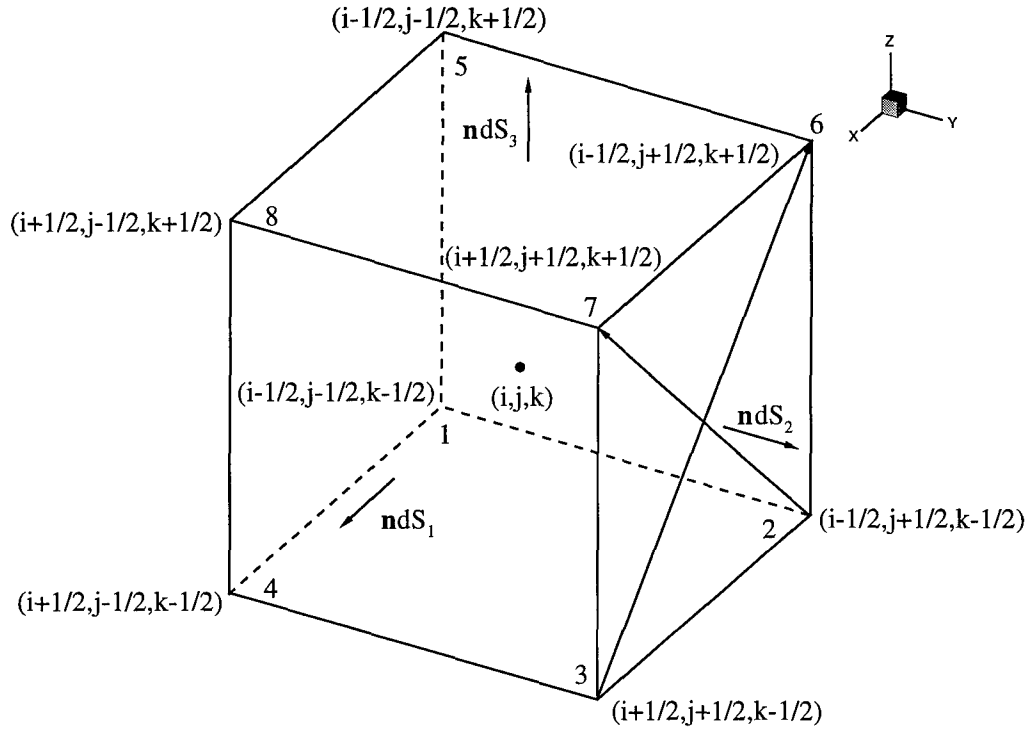


Figure A.1: Finite-Volume Cell

The magnitudes of each flux component in Equations (A.13)-(A.15) are calculated using a flux-splitting method. The split fluxes correspond to the magnitude of the flux associated with the positive and negative eigenvalues. The magnitude of the flux is the sum of the individual split fluxes. The details for the flux-splitting will be discussed in Section A.6.

Equation (A.12) is a generic finite-volume formulation. One of numerous techniques can be used to calculate the fluxes and to perform the time integration. Shang uses a Monotone Upstream-Centered Scheme for Conservation Laws (MUSCL) to calculate the fluxes on the surfaces of the cells and a multi-stage Runge-Kutta method to solve it in the temporal domain [37]. The methods used to solve it are characteristic-based; therefore, a brief review of applicable linear algebra will be given to provide a foundation for the discussion of the characteristic-based scheme.

A.5 Eigenvalues and Eigenvectors

As review, a system of linear equations can be solved using linear algebra. The Maxwell equations in conservation form are a complete set of six linear equations. The system of equations can be solved using eigenvalue and eigenvector, or characteristic, analysis. The eigenvalues and eigenvectors of a linear system of equations satisfy the equation [49]

$$(\mathbf{D}-\lambda\mathbf{I})\mathbf{x} = 0 \quad (\text{A.19})$$

where \mathbf{D} : Coefficient matrix

λ : Eigenvalue

\mathbf{I} : Identity matrix

\mathbf{x} : Eigenvector corresponding to an eigenvalue

The eigenvalues and eigenvectors of the coefficient matrices in transformed coordinates is not required for the present FVTD formulation [37]. Only the eigenvalues and eigenvectors of the coefficient matrices of \mathbf{F} , \mathbf{G} , and \mathbf{H} in Cartesian coordinates are required because of the local orthogonal coordinate system developed and discussed later. The flux vectors \mathbf{F} , \mathbf{G} , and \mathbf{H} , can be represented as $\mathbf{F}=\mathbf{A}\mathbf{U}$, $\mathbf{G}=\mathbf{B}\mathbf{U}$, and $\mathbf{H}=\mathbf{C}\mathbf{U}$, respectively, if the constitutive parameters are scalars. \mathbf{U} is the same vector as used in Equation (A.6). The coefficient matrices \mathbf{A} , \mathbf{B} , and \mathbf{C} are shown below [29]:

$$\mathbf{A} = \begin{bmatrix} 0 & 0 & 0 & 0 & 0 & 0 \\ 0 & 0 & 0 & 0 & 0 & \frac{1}{\epsilon} \\ 0 & 0 & 0 & 0 & -\frac{1}{\epsilon} & 0 \\ 0 & 0 & 0 & 0 & 0 & 0 \\ 0 & 0 & -\frac{1}{\mu} & 0 & 0 & 0 \\ 0 & \frac{1}{\mu} & 0 & 0 & 0 & 0 \end{bmatrix} \quad (\text{A.20})$$

$$\mathbf{B} = \begin{bmatrix} 0 & 0 & 0 & 0 & 0 & -\frac{1}{\epsilon} \\ 0 & 0 & 0 & 0 & 0 & 0 \\ 0 & 0 & 0 & \frac{1}{\epsilon} & 0 & 0 \\ 0 & 0 & \frac{1}{\mu} & 0 & 0 & 0 \\ 0 & 0 & 0 & 0 & 0 & 0 \\ -\frac{1}{\mu} & 0 & 0 & 0 & 0 & 0 \end{bmatrix} \quad (\text{A.21})$$

$$\mathbf{C} = \begin{bmatrix} 0 & 0 & 0 & 0 & \frac{1}{\epsilon} & 0 \\ 0 & 0 & 0 & -\frac{1}{\epsilon} & 0 & 0 \\ 0 & 0 & 0 & 0 & 0 & 0 \\ 0 & -\frac{1}{\mu} & 0 & 0 & 0 & 0 \\ \frac{1}{\mu} & 0 & 0 & 0 & 0 & 0 \\ 0 & 0 & 0 & 0 & 0 & 0 \end{bmatrix} \quad (\text{A.22})$$

The eigenvalues of \mathbf{A} , \mathbf{B} , and \mathbf{C} are [29]

$$\Lambda = \text{Diagonal} \left\{ \frac{1}{\sqrt{\epsilon\mu}}, \frac{1}{\sqrt{\epsilon\mu}}, -\frac{1}{\sqrt{\epsilon\mu}}, -\frac{1}{\sqrt{\epsilon\mu}}, 0, 0 \right\} \quad (\text{A.23})$$

The eigenvalues are equal to the speed of the electromagnetic wave in the medium. In free space, the eigenvalues are equal to the speed of light. The signs indicate the direction of propagation of the wave. The eigenvalues are repeated and contain multiplicities, but linearly independent eigenvectors can still be found [34].

The coefficient matrices \mathbf{A} , \mathbf{B} , and \mathbf{C} can be transformed using similarity matrices. The transformation uncouples the six equations in the system of linear equations, Equation (A.6), so that each can be solved independently. The transformation has the form [49]

$$\Lambda = \mathbf{S}^{-1} \mathbf{D} \mathbf{S} \quad (\text{A.24})$$

where Λ : Diagonal matrix containing the eigenvalues of \mathbf{D} along the diagonal

For the FVTD formulation, split fluxes are calculated [37]. The flux-splitting procedure splits the fluxes according to the direction of propagation [34]. The split fluxes are calculated using the similarity matrices and the corresponding positive or negative eigenvalue. Forward differencing is used for the negative eigenvalue and backward differencing is used for the positive eigenvalue [30]. The calculation of the split fluxes is facilitated with the use of a local orthogonal system.

A.6 Flux Evaluation using a Local Orthogonal Coordinate System

In Cartesian coordinates, the split flux vectors can be calculated by [37]

$$\mathbf{F}_{i+\frac{1}{2}}^+ = \mathbf{S}\mathbf{\Lambda}^+\mathbf{S}^{-1}\mathbf{U}_{i+\frac{1}{2}}^+ \quad (\text{A.28})$$

$$\mathbf{F}_{i+\frac{1}{2}}^- = \mathbf{S}\mathbf{\Lambda}^-\mathbf{S}^{-1}\mathbf{U}_{i+\frac{1}{2}}^- \quad (\text{A.29})$$

where $\mathbf{\Lambda}^+$: Diagonal matrix containing the positive eigenvalues which correspond to the flux flowing in the positive direction through the face with index $i+1/2$

$\mathbf{\Lambda}^-$: Diagonal matrix containing the negative eigenvalues which correspond to the flux flowing in the negative direction through the face with index $i+1/2$

The calculation of the flux in the characteristic-based FVTD formulation in transformed coordinates is greatly facilitated with the use of a local orthogonal system in the transformed space (i.e. ξ , η , and ζ space). The local orthogonal system is established for each face of a cell and includes the normal to the face and two unit vectors lying in the face. Diagonalization of the coefficient matrices in the curvilinear coordinate system is not required [37]. The transformation between two orthogonal systems is well known and permits easy calculation of the fluxes:

$$\hat{\mathbf{F}}^\pm = \mathbf{M}^{-1}\hat{\mathbf{M}}\hat{\mathbf{F}}^\pm = \mathbf{M}^{-1}\tilde{\mathbf{F}}^\pm \quad (\text{A.30})$$

$$\hat{F}_{i+\frac{1}{2}} = \mathbf{M}^{-1}(\tilde{\mathbf{S}}^{-1}\Lambda^+\tilde{\mathbf{S}}\mathbf{U}_{i+\frac{1}{2}}^+ + \tilde{\mathbf{S}}^{-1}\Lambda^-\tilde{\mathbf{S}}\mathbf{U}_{i+\frac{1}{2}}^-) = \hat{F}_{i+\frac{1}{2}}^+ + \hat{F}_{i+\frac{1}{2}}^- \quad (\text{A.31})$$

- where \mathbf{M}^T : Transpose of the matrix containing the metrics of the coordinate transformation
- \mathbf{M} : Matrix containing the metrics of the coordinate transformation between the Cartesian coordinate system and the local orthogonal coordinate system
- $\hat{\mathbf{M}}$: Matrix containing the metrics of the coordinate transformation between the Cartesian coordinate system and the curvilinear coordinate system
- \tilde{F}^\pm : Positive and negative split flux through the face where the local orthogonal system has been established
- \hat{F}^\pm : Positive and negative flux through a face, expressed in curvilinear coordinates
- $\hat{F}_{i+\frac{1}{2}}^+$: Positive split flux expressed in curvilinear coordinates through the (i+1/2) face
- $\hat{F}_{i+\frac{1}{2}}^-$: Negative split flux expressed in curvilinear coordinates through the (i+1/2) face
- $\hat{F}_{i+\frac{1}{2}}$: Sum of the positive and negative flux expressed in curvilinear coordinates through the (i+1/2) face
- $\tilde{\mathbf{S}}$: Matrix containing the eigenvectors of the local orthogonal system, same as \mathbf{S}_A in Equation (A.26)

The flux which is evaluated using Equation (A.31) is used in Equation (A.13). Note that the flux is evaluated at the face and the values of the \mathbf{U} vector on the face must be calculated from the cell centers. The numerical accuracy of the numerical algorithm is dependent on the extrapolation procedure used to calculate the fluxes from the values of the fields at the cell centers. The accuracy is also dependent on the metrics of the cells (i.e. surface area vector) [34]. The same flux-splitting procedure is used to calculate the $\hat{\mathbf{G}}$ and $\hat{\mathbf{H}}$ flux vectors.

The values of the U vector on the cell interfaces are calculated using a high-order accurate extrapolation scheme developed by van Leer [53]. The Monotone Upstream-Centered Scheme for Conservation Laws (MUSCL) is used to create a third-order accurate solution for the Maxwell's equations. The fluxes in Equation (A.32) and the \hat{G} and \hat{H} fluxes are calculated based on piece-wise data from the centers of adjacent cells (U vector) from the previous time step. Values of the U vector are required at the cell face to calculate the split-flux vectors. The fields for one side of the cell, such as $i = 1/2$, are

$$U_{i+\frac{1}{2}}^+ = U_i + \frac{\phi}{4} [(1-\kappa)(U_i - U_{i-1}) + (1+\kappa)(U_{i+1} - U_i)] \quad (A.32)$$

$$U_{i+\frac{1}{2}}^- = U_{i+1} - \frac{\phi}{4} [(1+\kappa)(U_{i+1} - U_i) + (1-\kappa)(U_{i+2} - U_{i+1})] \quad (A.33)$$

where κ and ϕ are parameters which control the accuracy of the approximation. To obtain third-order accuracy from van Leer's kappa scheme, $\kappa = 1/3$ and $\phi = 1$. The subscripts correspond to the cell center locations referenced to the current cell.

A.7 Time Integration

For the time integration of Equation (A.12), a multi-stage Runge-Kutta scheme is used [38]. A fourth-order, four-stage scheme is calculated as follows:

$$U^0 = U^0(t, U^n) \quad (A.34)$$

$$U^1 = U^1(t + \Delta t / 2, U^n + \Delta t / 2 \cdot U^0) \quad (A.35)$$

$$U^2 = U^2(t + \Delta t / 2, U^n + \Delta t / 2 \cdot U^1) \quad (A.36)$$

$$U^3 = U^3(t + \Delta t, U^n + \Delta t \cdot U^2) \quad (A.37)$$

$$U^{n+1} = U^n + \Delta t / 6 \cdot (U^0 + 2U^1 + 2U^2 + U^3) \quad (A.38)$$

where U^m : Value of the electric and magnetic flux densities at the cell centers at stage m

For other orders of accuracy, refer to [26]. The intermediate steps between U_n and U_{n+1} have no physical meaning. The values of U are physically located at the cell center. U is found by adding the split fluxes and dividing by the cell volume as in Equation (A.12).

A.8 Incident Wave

To obtain the scattered field from an object, an incident field must be generated in the computational grid. Various waveforms can be used to analyze the scattering from an object. A sinusoid, $\sin(\omega t)$, can be used to analyze the scattering for a single frequency. However, an advantage of the time-domain analysis is that multiple frequencies can be analyzed simultaneously with one computer simulation. A Gaussian pulse is ideal to use as an incident wave for multiple-frequency analysis. The Gaussian pulse contains multiple frequencies and has the form [18]

$$g(t) = \exp \left[- \left(\frac{t - t_0}{T} \right)^2 \right] \quad (A.39)$$

where $g(t)$: Gaussian pulse with an amplitude of unity

t_0 : Center of Gaussian pulse

T : Period/duration of the Gaussian pulse

The Gaussian pulse and the parameters for the incident wave are described in detail in Chapter 3. A trade-off exists between a sinusoid incident wave and a Gaussian pulse. A Gaussian pulse will give results for multiple frequencies, but the duration of the simulation can be several times longer than the test with the sinusoid incident wave. The particular incident wave can be selected depending on the results desired.

A.9 Boundary Conditions

A.9.1 Scatterer Surface Boundary Conditions

For perfect electric conductor (PEC) objects, surface boundary conditions state that the tangential components of the total electric field are equal to zero and the normal components of the total magnetic flux density are zero:

$$\mathbf{n} \times \mathbf{E} = 0 \quad (A.40)$$

$$\mathbf{n} \cdot \mathbf{B} = 0 \quad (A.41)$$

In the FVTD formulation, the electric and magnetic fields are both calculated on the surface of the scatterer. Therefore, extrapolated boundary conditions are needed to solve for the unknowns. The extrapolated boundary conditions which are introduced to solve for the total fields at the surface of the scatterer are given by [38]

$$\mathbf{n} \cdot \nabla (\mathbf{n} \times (\mathbf{H}_1 - \mathbf{H}_2)) = 0 \quad (A.42)$$

$$\mathbf{n} \cdot \nabla (\mathbf{n} \cdot (\mathbf{D}_1 - \mathbf{D}_2)) = 0 \quad (A.43)$$

where $\mathbf{n} \times (\mathbf{H}_1 - \mathbf{H}_2)$: \mathbf{J}_s - electric current density with finite jump of constant value [38]

$\mathbf{n} \cdot (\mathbf{D}_1 - \mathbf{D}_2)$: ρ - electric charge density with finite jump of constant value [38]

The current and charge densities are assumed to be finite jumps and piece-wise continuous.

A.9.2 Radiation Boundary Condition

In a computational space, the truncated space will produce erroneous errors. The truncated space produces reflections which propagate through the grid. Shang uses a compatibility condition which sets the incoming flux component equal to zero at the outer edge of the computational grid.

Ideally, the one-dimensional characteristic boundary condition is exact for wave motion in one coordinate direction. For multiple dimensions, the boundary condition reduces to first-order accuracy depending on the wave direction. Because of the low order of accuracy, the outer edge of the grid must be placed two to three wavelengths from the scatterer surface to minimize the reflections which contaminate the scattering computations.

A.10 Fourier Transform

A Fourier Transform (FT) can be used to obtain frequency data from the time-domain scattered field results. The FT takes the following form [23]:

$$X(\omega) = \frac{1}{N} \sum_{n=0}^{N-1} x(n) e^{-j\omega n \Delta t} \quad (A.44)$$

where n : Index for time increments

N : Maximum time increment for the FT

ω : Radian frequency

$x(n)$: Total field component calculated at time n

$X(\omega)$: Amplitude of the scattered electric or magnetic field for radian frequency ω

The FT results are used in the near-to-far field transformation. The transformation requires sinusoidal or phasor values for the total fields. The summation in Equation (A.45) is performed for each frequency at the end of each time step as an accumulating sum.

A.11 Near-to-Far Field Transformation

To obtain far-field parameters, such as the radar cross section (RCS), a near-field to far-field transformation is required. The transformation requires equivalent electric and magnetic currents and charges on a virtual surface surrounding the object of interest. A review of the

surface equivalence theorem will be given, and then the near-field to far-field transformation will be discussed in detail.

A.11.1 Surface Equivalence Theorem

The surface equivalence theorem, or Huygen's principle, places a virtual surface around an object or sources and replaces the electric and magnetic fields on the boundary of the virtual surface with equivalent electric or magnetic currents and charges which satisfy the boundary conditions [3]. The currents are selected so that the fields inside the surface are zero and the fields outside are equivalent to the fields produced by the sources on the surface or equivalent to the scattered fields. The currents are calculated from the tangential fields over the virtual surface and the equivalent charges are calculated from the normal fields at the surface [51]:

$$\mathbf{J}_s = \mathbf{n} \times \mathbf{H} \quad (A.45)$$

$$\mathbf{M}_s = -\mathbf{n} \times \mathbf{E} \quad (A.46)$$

$$\rho_{es} = \mathbf{n} \cdot \mathbf{H} \quad (A.47)$$

$$\rho_{ms} = \mathbf{n} \cdot \mathbf{E} \quad (A.48)$$

where \mathbf{n} : Outward normal of the virtual surface

\mathbf{E}, \mathbf{H} : Phasor representations of the total electric and magnetic fields

\mathbf{J}_s : Equivalent electric current density tangential to virtual surface

\mathbf{M}_s : Equivalent magnetic current density tangential to virtual surface

ρ_{es} : Equivalent electric charge on the virtual surface

ρ_{ms} : Equivalent magnetic charge on the virtual surface

The equivalent currents and charges are used in the near-field to far-field transformation.

A.11.2 Transformation

The equivalent currents and charges are used to find the far fields; however, the transformation requires time-harmonic quantities. The equivalent phasor currents and charges are calculated from the scattered fields by using a FT and the equivalence theorem as discussed in the previous section [51]. Once the currents and charges are found, the following transformation computes the far-field quantities [12] for the scattered field:

$$\mathbf{E}^s = \frac{\exp(jk\mathbf{R})}{\mathbf{R}} \cdot \frac{jk}{4\pi} \oint\oint_{S'} \left[\left(\frac{\mu}{\epsilon} \right)^{\frac{1}{2}} (\mathbf{n} \times \mathbf{H}) - (\mathbf{n} \times \mathbf{E}) \times \mathbf{r} - (\mathbf{n} \cdot \mathbf{E}) \mathbf{r} \right] \exp(-jk\mathbf{r} \cdot \mathbf{R}') dS' \quad (A.49)$$

$$\mathbf{H}^s = \frac{\exp(jk\mathbf{R})}{\mathbf{R}} \cdot -\frac{jk}{4\pi} \oint\oint_{S'} \left[\left(\frac{\epsilon}{\mu} \right)^{\frac{1}{2}} (\mathbf{n} \times \mathbf{E}) + (\mathbf{n} \times \mathbf{H}) \times \mathbf{r} + (\mathbf{n} \cdot \mathbf{H}) \mathbf{r} \right] \exp(-jk\mathbf{r} \cdot \mathbf{R}') dS' \quad (A.50)$$

where $\mathbf{E}^s, \mathbf{H}^s$: Far-field scattered electric and magnetic fields

k : Wave number

\mathbf{n} : Unit vector normal to the virtual surface

\mathbf{r} : Unit vector in the direction of the far-field observation point

\mathbf{R} : Vector from the origin to the observation point

\mathbf{R}' : Vector from the origin to a point on the virtual surface

S' : Closed virtual surface over which the equivalent surface charges and currents are integrated

The primed coordinates refer to an integration over the virtual surface or a point on the virtual surface as shown in Figure A.2. The observation point is in the far field and the various vectors describing the location of the scatterer and observation point are shown in the illustration.

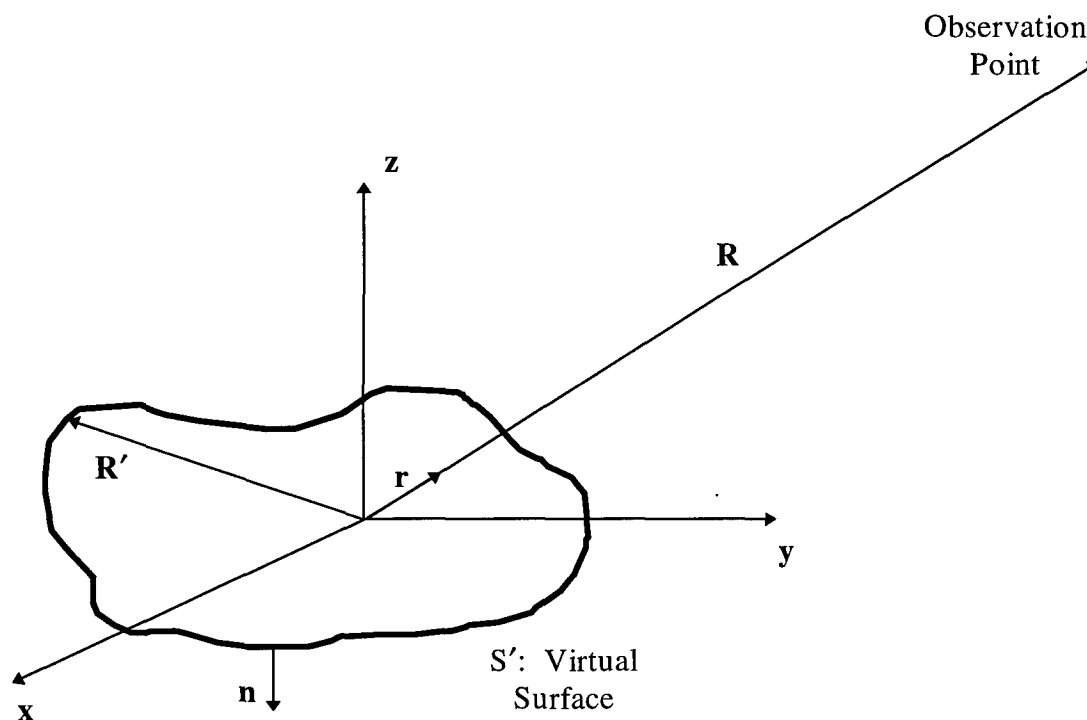


Figure A.2: Virtual Surface and Far-Field Sketch

A.12 RCS Calculations

The RCS can be obtained for the backscatter direction or the bistatic direction. The RCS is calculated by using

$$\sigma_{3-D} = \lim_{R \rightarrow \infty} 4\pi R^2 \frac{|\mathbf{E}^s|^2}{|\mathbf{E}^i|^2} \quad (A.51)$$

where \mathbf{E}^i : Incident electric field (sinusoid or Gaussian pulse)

\mathbf{E}^s : Scattered electric field

R: Distance to the observation point (Magnitude of \mathbf{R} in Equation (A.50))

The magnitude of the scattered electric field is calculated using Equation (A.50). The RCS can also be determined from the scattered magnetic field in the same way using Equation (A.51) and the equivalent equation of (A.52) for the magnetic field.

A.13 Summary

The FVTD formulation calculates the scattering and the RCS from PEC objects using a scattered-field formulation of the time-dependent Maxwell equations. A characteristic-based FVTD formulation is used to solve the Maxwell equations. The FVTD formulation uses a van Leer's kappa scheme for the flux evaluation and a Runge-Kutta multi-stage scheme for the time integration. The far-field scattering results such as the RCS are obtained from the electromagnetic fields subsequent to a Fourier transform and a near-to-far field transformation.

Appendix B: Finite-Volume Time-Domain FORTRAN Code

This appendix contains the code listings and descriptions of the FORTRAN finite-volume time-domain (FVTD) code modifications. Also included in this appendix is a MATLAB code for comparing FVTD results to Moment Method results and a MATLAB code for generating a movie of contour slices of the scattered electric field from a cone-sphere.

B.1 FVTD FORTRAN Code Outline

The basic structure of the FORTRAN 77 code is shown in Figure B.1. The code closely follows the outline in Appendix A which describes the procedures required to solve an electromagnetic scattering problem using FVTD. Apart from the time loop and the loops required to calculate the fluxes, the code follows a sequential process to solve for the RCS of a 3-D object.

At the beginning of the code, the input data and the grid data are read. Initial parameters for the incident wave and metrics of the finite-volume cells are computed. The time loop is then entered and for each time step, the \mathbf{F} , \mathbf{G} , and \mathbf{H} flux vectors are calculated in separate subroutines. Boundary conditions are implemented at the beginning of each time step. The fluxes are computed for the faces of the finite-volume cells as described in Appendix A. The \mathbf{U} vector, physically located at the center of the cells, is computed from the fluxes at the end of each time step. Once the time loop is completed, the Fourier transform and near-to far field transformation are calculated, and the RCS values are computed from the field data.

As shown in Figure B.1, the Runge-Kutta loop is completed four times for every time step. The fourth-order accurate code requires the fluxes (electric and magnetic fields) to be computed four times for every time step to obtain the fourth-order accuracy. The extra

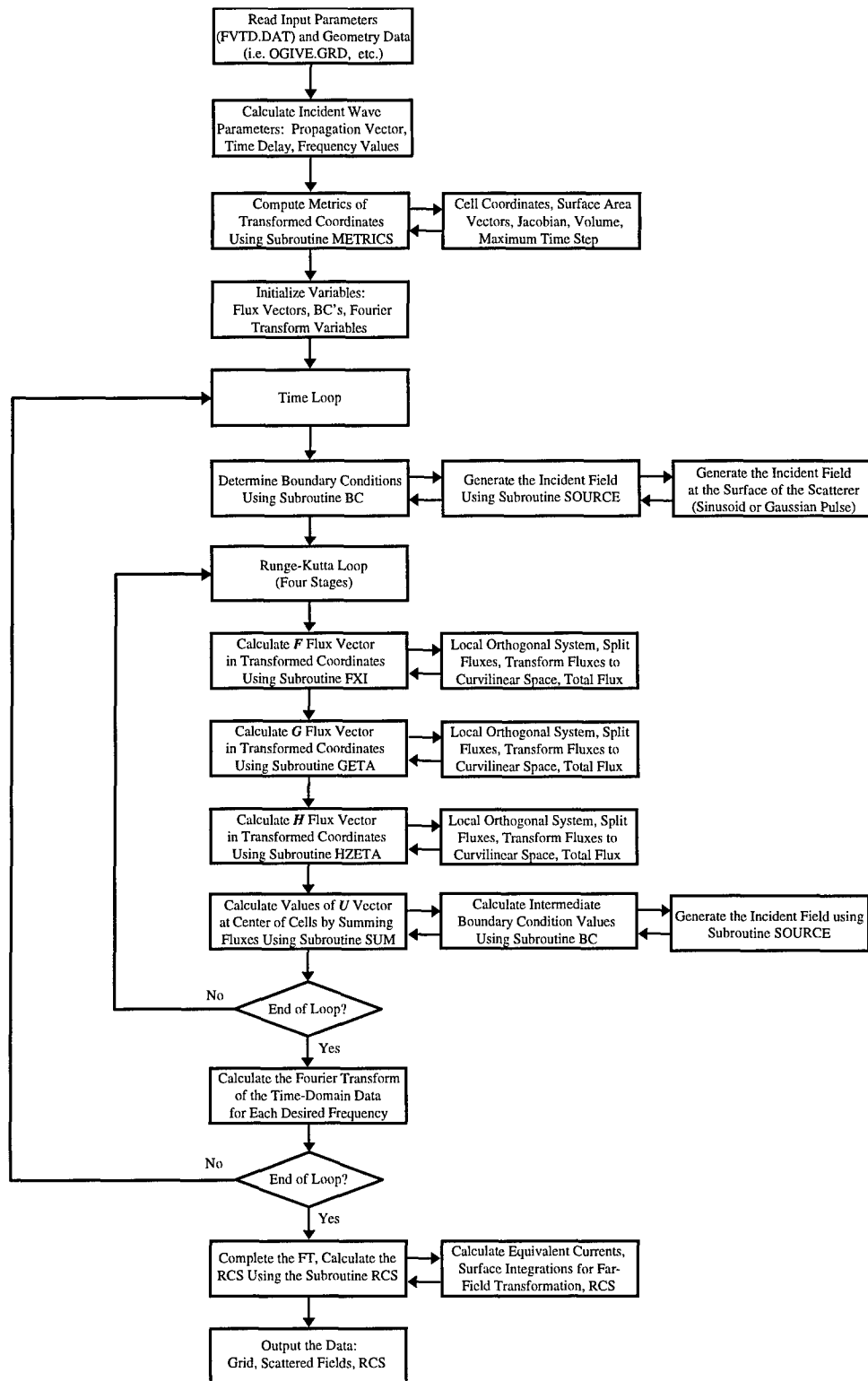


Figure B.1: FVTD.F Flowchart

computational time required would be excessive except the higher-order accurate code permits a much larger CFL value resulting in a larger time step as compared to a lower-order accurate code.

B.2 FVTD Code Listings of Modifications

The original code contained approximately 1450 lines of code and the modified code contains approximately 2350 lines of code. The modifications include the following subtopics:

- input file (FVTD.DAT) for specifying grid size, geometry type, incident wave type, material parameters, stability parameters, and Fourier transform variables
- input grid file with the option to add or delete grid points depending on the frequency of the incident wave and the desired accuracy
- incident wave type, polarization, and direction
- RCS convergence check and threshold check used in conjunction with a sinusoid and Gaussian pulse incident wave, respectively
- bistatic-to-monostatic approximation to obtain monostatic values from bistatic calculations

The code modifications are described and listed below.

B.2.1 Input File

The input file, FVTD.DAT, for the FVTD.F code is listed below. The input parameters are described in the file. Parameters for the grid size, geometry, incident wave, material, stability, and Fourier transform can be specified in the input file. Most of the variables are self-explanatory but several clarifications are required.

***** FVTD.DAT: INPUT FILE FOR FVTD.F *****

INPUT VARIABLES:

GRID VARIABLES:

IL: MAX X/XI INDEX, CORRESPONDS TO NUMBER OF GRID POINTS
 JL: MAX Y/ETA INDEX, CORRESPONDS TO NUMBER OF GRID POINTS
 KL: MAX Z/ZETA INDEX, CORRESPONDS TO NUMBER OF GRID POINTS

GEOMETRY VARIABLES

IGEO: INDICATOR FOR TYPE OF GEOMETRY
 "0": SPHERE (GRID GENERATED IN FVTD CODE)
 "1": OGIVE (GRID FILE, OGIVE.GRD, REQUIRED)
 "2": CONE-SPHERE (GRID FILE, CONESPH.GRD, REQUIRED)
 "3": MISCELLANEOUS GEOMETRY (GRID FILE REQUIRED)

RO: DISTANCE OF OUTER BOUNDARY BEYOND SCATTERER SURFACE
 (IN TERMS OF WAVELENGTHS)

NGPD: TIP GRID POINT DENSITY IF REQUIRED (POINTS/WAVELENGTH)

INCIDENT WAVE VARIABLES:

AMP: PEAK AMPLITUDE OF THE INCIDENT WAVE
 PHI: PHI DIRECTION OF INCIDENT WAVE (SPHERICAL COORDINATES)
 THI: THETA DIRECTION OF INCIDENT WAVE (SPHERICAL COORDINATES)
 EPHI: E FIELD COMPONENT (POLARIZATION) IN THE PHI DIRECTION
 ETHI: E FIELD COMPONENT (POLARIZATION) IN THE THETA DIRECTION
 NOTE: $\sqrt{EPHI^2 + ETHI^2}$ SHOULD BE EQUAL TO ONE
 ISRC: INDICATOR FOR TYPE OF INCIDENT WAVE
 "0": SINUSOID (SPECIFY W)
 "1": GAUSSIAN PULSE (SPECIFY GPT, GPD, AND WD)
 W: SINUSOID RADIAN FREQUENCY
 GPT: GAUSSIAN PULSE PERIOD (NORMALIZED: $(T \cdot C)$)
 GPD: GAUSSIAN PULSE TIME DELAY (CENTER OF PULSE, IN TERMS OF GPT)
 WD: GAUSSIAN PULSE RADIAN FREQUENCY DELTA (FREQUENCY INCREMENT)

MATERIAL VARIABLES:

REP: RELATIVE EPSILON, ELECTRIC PERMITTIVITY
 RMU: RELATIVE MU, MAGNETIC PERMEABILITY

STABILITY VARIABLES:

CFL: COURANT-FRIEDRICHS-LEWY NUMBER, CONTROLS STABILITY

FOURIER TRANSFORM VARIABLES:

ICON: CONVERGENCE INDICATOR FOR SINUSOID INCIDENT WAVE
 "0": DO NOT USE CONVERGENCE CHECK
 "1": USE CONVERGENCE CHECK (NBS,NES,AND NEND ARE NOT USED)
 NBS: TIME BEGINNING POINT FOR THE FT (NUMBER OF PERIODS)
 NES: TIME ENDPOINT FOR THE FT (NUMBER OF PERIODS)
 NEND: TIME ENDPOINT FOR THE FVTD CODE (NUMBER OF PERIODS)

INPUT PARAMETERS:

 IL 71
 JL 74
 KL 45
 IGEO 1
 RO 3.0
 NGPD 30
 AMP 1.0
 PHI 0.0
 THI 0.0
 EPHI 0.0
 ETHI 1.0
 ISRC 0
 W 24.17386
 GPT 0.0182556
 GPD 4.0
 WD 10.4719755

REP	1.0
RMU	1.0
CFL	1.5
ICON	0
NBS	5
NES	7
NEND	7

Miscellaneous closed-surface 3-D geometries can be read in under the option of "3" for the variable "IGEO". This will permit easy expansion of the code for analyzing other closed-surface, single-zone PEC geometries other than a sphere, ogive, and cone-sphere. Possible geometries include the EMCC-defined double ogive, cone-sphere with gap, or almond. The grid generated for the geometry must incorporate several important features. First, the value for "KL" must be odd. Several sections of the code assume that KL is odd to correctly generate grid overlap areas and to fill in voids in the calculation of the fluxes. The values of "IL" and "KL" can be odd or even. Second, the code assumes that the PEC surface of the geometry is the first cell in the radial direction (spherical coordinates). The PEC surface boundary conditions are imposed at the first cell in the radial direction. Third, the FVTD code assumes the z axis is the line of singularity, or rotation (ϕ), for the grid. For example, the tips of the ogive in the ogive grid are located on the line of singularity. The geometry doesn't necessarily have to be a body-of-revolution (BOR) for an appropriate grid to be generated correctly for the code. A grid could be generated for the NASA almond which is not a BOR [55]. If the z axis is not the line of singularity, the grid coordinates must be rotated. These three grid requirements are necessary for the correct use of the FVTD code.

The constitutive parameters, REP and RMU, can be specified only for real values. Currently the code cannot incorporate complex values for the permittivity and permeability although this would be a relatively simple modification.

The specification of the Fourier transform variables require clarification. For use with a sinusoid incident wave without the RCS convergence check, the "NBS" and "NES" variables specify the value of the periods in which the Fourier data will be taken which is usually for two to three periods after the transients diminish. If a sinusoid incident wave is used with the RCS convergence check, the variables "NBS" and "NES" are specified in the same way except the Fourier transform data is taken for only one period. "NBS" can begin after one or two periods and the simulation will not end until convergence has been reached. "NES" and "NEND" can be used to "override" the convergence check and end the simulation. For a Gaussian pulse, "NBS" is not used since the Fourier transform data is taken beginning with the first time step. "NES" and "NEND" are specified to "override" the threshold check. The simulation ends if the amplitude of the scattered field is less than 140 dB below the peak of the incident field; however, if the "NES" value is reached before this point, the simulation ends. The override gives the user a method to end the test and obtain data without running out of computer queue time.

If a Gaussian pulse is used for the incident wave, several parameters must be specified. Table B.1 is included as a reference for specifying the Gaussian pulse parameters. First, the bandwidth of the pulse is required. Typically, only one-third of the bandwidth of the pulse is used [18]. Therefore, a pulse must be specified which has three times the bandwidth of the desired bandwidth. For example, if the RCS values are required for 6 GHz, the parameters for a pulse with a bandwidth of 18 GHz (f) must be specified. The code was modified to incorporate up to 15 different frequencies; therefore, "WD" must be specified accordingly as to not exceed the limit of 15 frequencies within the specified bandwidth. "GPD" is always specified as 4.0 so the Gaussian pulse is truncated at 140 dB down from the peak. "GPD" refers to the Gaussian pulse delay and should not be confused with GPD used in Chapter 4. The transients produced at this truncation level are negligible. The value of t_0 , computed in the code, will be the value as

shown in the table.. The value of “W” should be specified for the frequency in which the grid is optimized. The values in the table are normalized to the velocity of a wave in the medium and are specified in the same way in the input file. The parameters in the FVTD code are also normalized to the velocity of the medium (i.e. velocity of an electromagnetic wave in free space).

Table B.1: Gaussian Pulse Parameters for a Specified Bandwidth

f (GHz)	f (Normalized)	W (Normalized)	GPT (Normalized)	t ₀ (Normalized)
0.1	0.333333	2.0943953	3.833790719	15.33516288
0.2	0.666666	4.1887906	1.916835138	7.667340554
0.3	1.000000	6.2831860	1.277890092	5.111560369
0.4	1.333333	8.3775813	0.958417569	3.833670277
0.5	1.666666	10.4719766	0.766734055	3.066936221
0.6	2.000000	12.5663720	0.638945046	2.555780185
0.7	2.333333	14.6607673	0.547667182	2.190668730
0.8	2.666666	16.7551626	0.479208785	1.916835138
0.9	3.000000	18.8495580	0.425963364	1.703853456
1.0	3.333333	20.9439533	0.383367028	1.533468111
1.5	5.000000	31.4159300	0.255578018	1.022312074
2.0	6.666666	41.8879066	0.191683514	0.766734055
2.5	8.333333	52.3598833	0.153346811	0.613387244
3.0	10.000000	62.8318600	0.127789009	0.511156037
3.5	11.666666	73.3038366	0.109533436	0.438133746
4.0	13.333333	83.7758133	0.095841757	0.383367028
4.5	15.000000	94.2477900	0.085192673	0.340770691
5.0	16.666666	104.7197667	0.076673406	0.306693622
5.5	18.333333	115.1917433	0.069703096	0.278812384
6.0	20.000000	125.6637200	0.063894505	0.255578018
6.5	21.666666	136.1356967	0.058979543	0.235918171
7.0	23.333333	146.6076733	0.054766718	0.219066873
7.5	25.000000	157.0796500	0.051115604	0.204462415
8.0	26.666666	167.5516267	0.047920878	0.191683514
8.5	28.333333	178.0236033	0.045102003	0.180408013
9.0	30.000000	188.4955800	0.042596336	0.170385346
9.5	31.666666	198.9675567	0.040354424	0.161417696
10.0	33.333333	209.4395333	0.038336703	0.153346811
10.5	35.000000	219.9115100	0.036511145	0.146044582
11.0	36.666666	230.3834867	0.034851548	0.139406192
11.5	38.333333	240.8554633	0.033336263	0.133345053
12.0	40.000000	251.3274400	0.031947252	0.127789009
12.5	41.666666	261.7994167	0.030669362	0.122677449
13.0	43.333333	272.2713933	0.029489771	0.117959085
13.5	45.000000	282.7433700	0.028397558	0.113590230
14.0	46.666666	293.2153467	0.027383359	0.109533436
14.5	48.333333	303.6873233	0.026439105	0.105756421
15.0	50.000000	314.1593000	0.025557802	0.102231207

f (GHz)	f (Normalized)	W (Normalized)	GPT (Normalized)	t _n (Normalized)
15.5	51.666666	324.6312767	0.024733357	0.098933426
16.0	53.333333	335.1032533	0.023960439	0.095841757
16.5	55.000000	345.5752300	0.023234365	0.092937461
17.0	56.666666	356.0472067	0.022551002	0.090204007
17.5	58.333333	366.5191833	0.021906687	0.087626749
18.0	60.000000	376.9911600	0.021298168	0.085192673
18.5	61.666666	387.4631367	0.020722542	0.082890168
19.0	63.333333	397.9351133	0.020177212	0.080708848
19.5	65.000000	408.4070900	0.019659848	0.078639390
20.0	66.666666	418.8790667	0.019168351	0.076673406
20.5	68.333333	429.3510433	0.018700831	0.074803322
21.0	70.000000	439.8230200	0.018255573	0.073022291
21.5	71.666666	450.2949967	0.017831025	0.071324098
22.0	73.333333	460.7669733	0.017425774	0.069703096
22.5	75.000000	471.2389500	0.017038535	0.068154138
23.0	76.666666	481.7109267	0.016668132	0.066672527
23.5	78.333333	492.1829033	0.016313491	0.065253962
24.0	80.000000	502.6548800	0.015973626	0.063894505
24.5	81.666666	513.1268567	0.015647634	0.062590535
25.0	83.333333	523.5988333	0.015334681	0.061338724
25.5	85.000000	534.0708100	0.015034001	0.060136004
26.0	86.666666	544.5427867	0.014744886	0.058979543
26.5	88.333333	555.0147633	0.014466680	0.057866721
27.0	90.000000	565.4867400	0.014198779	0.056795115
27.5	91.666666	575.9587167	0.013940619	0.055762477
28.0	93.333333	586.4306933	0.013691680	0.054766718
28.5	95.000000	596.9026700	0.013451475	0.053805899
29.0	96.666666	607.3746467	0.013219553	0.052878211
29.5	98.333333	617.8466233	0.012995492	0.051981970
30.0	100.00000	628.3186000	0.012778901	0.051115604
30.5	101.66666	638.7905767	0.012569411	0.050277643
31.0	103.33333	649.2625533	0.012366678	0.049466713
31.5	105.00000	659.7345300	0.012170382	0.048681527
32.0	106.66666	670.2065067	0.011980220	0.047920878
32.5	108.33333	680.6784833	0.011795909	0.047183634
33.0	110.00000	691.1504600	0.011617183	0.046468731
33.5	111.66666	701.6224367	0.011443792	0.045775167
34.0	113.33333	712.0944133	0.011275501	0.045102003
34.5	115.00000	722.5663900	0.011112088	0.044448351
35.0	116.66666	733.0383667	0.010953344	0.043813375
35.5	118.33333	743.5103433	0.010799071	0.043196285
36.0	120.00000	753.9823200	0.010649084	0.042596336
36.5	121.66666	764.4542967	0.010503206	0.042012825
37.0	123.33333	774.9262733	0.010361271	0.041445084
37.5	125.00000	785.3982500	0.010223121	0.040892483
38.0	126.66666	795.8702267	0.010088606	0.040354424
38.5	128.33333	806.3422033	0.009957585	0.039830341
39.0	130.00000	816.8141800	0.009829924	0.039319695
39.5	131.66666	827.2861567	0.009705494	0.038821977
40.0	133.33333	837.7581333	0.009584176	0.038336703
40.5	135.00000	848.2301100	0.009465853	0.037863410

f (GHz)	f (Normalized)	W (Normalized)	GPT (Normalized)	t _o (Normalized)
41.0	136.66666	858.7020867	0.009350415	0.037401661
41.5	138.33333	869.1740633	0.009237760	0.036951039
42.0	140.00000	879.6460400	0.009127786	0.036511145
42.5	141.66666	890.1180167	0.009020401	0.036081603
43.0	143.33333	900.5899933	0.008915512	0.035662049
43.5	145.00000	911.0619700	0.008813035	0.035252140
44.0	146.66666	921.5339467	0.008712887	0.034851548
44.5	148.33333	932.0059233	0.008614989	0.034459958
45.0	150.00000	942.4779000	0.008519267	0.034077069
45.5	151.66666	952.9498767	0.008425649	0.033702596
46.0	153.33333	963.4218533	0.008334066	0.033336263
46.5	155.00000	973.8938300	0.008244452	0.032977809
47.0	156.66666	984.3658067	0.008156745	0.032626981
47.5	158.33333	994.8377833	0.008070885	0.032283539
48.0	160.00000	1005.3097600	0.007986813	0.031947252
48.5	161.66666	1015.7817370	0.007904475	0.031617899
49.0	163.33333	1026.2537130	0.007823817	0.031295268
49.5	165.00000	1036.7256900	0.007744788	0.030979154
50.0	166.66666	1047.1976670	0.007667341	0.030669362

B.2.2 Ogive Grid Modifications

The majority of the simulations were performed for the ogive. A detailed grid resolution study was performed. Addition and deletion of grid points increases the accuracy and the ability to obtain grid resolution requirements for the tips of the ogive. The subroutine for the ogive grid is listed below. A similar but shorter subroutine was used for the cone-sphere grid.

```

C *****
C SUBROUTINE OGIVE(NGPD)
C   PARAMETER(ID=75,JD=125,KD=45,KF=15,PI=3.14159265359)
C   COMMON /CO/ SXI(ID,JD,KD,3),SET(ID,JD,KD,3),SZT(ID,JD,KD,3),
1     V(ID,JD,KD),X(ID,JD,KD),Y(ID,JD,KD),Z(ID,JD,KD)
C   COMMON /IN/ AMPX,AMPY,AMPZ,DEL,GPD,GPT,ISRC,W,WG(KF),XDIS,YDIS,
1     ZDIS,XK,YK,ZK
C   COMMON /PR/ AMP,CFL,DT,EPS,IB,IL,JL,KL,ILM,JLM,KLM,KWM,REP,RMU,
1     RK,RO,RP,SS,T
C   DIMENSION XG(ID,JD,KD),YG(ID,JD,KD),ZG(ID,JD,KD)
C   CHARACTER *72 HEADER
C
C   VARIABLES USED ONLY IN THE OGIVE SUBROUTINE:
C   DJ:      DISTANCE IN THE J DIRECTION
C   DPH:     ANGLE INCREMENT IN THE PHI DIRECTION
C   GPD'S:   GRID POINT DENSITIES IN EACH DIRECTION
C   I,J,KG:  SIZE OF ORIGINAL GRID
C   IRI:     FACTOR TO INCREASE NUMBER OF POINTS IN RADIAL DIRECTION

```

```

C      I1,J1:      I AND J INDICES DURING AN INTERMEDIATE CALCULATION
C      JTD:        THETA INDEX TO WHICH TIP DENSITY WILL BE INCREASED
C      JTHD:       FACTOR TO DECREASE NUMBER OF POINTS IN THETA DIRECTION
C      JTHI:       FACTOR TO INCREASE NUMBER OF POINTS IN THETA DIRECTION
C      NGPD:       NUMBER OF POINTS REQUIRED FOR OGIVE TIPS
C      NR:         EXTRA NUMBER OF GRID POINTS ADDED IN RADIAL DIRECTION
C      R,D:        DISTANCE TO A GRID POINT OR BETWEEN GRID POINTS
C      ROE:        EXTENSION OF OUTER BOUNDARY IN THE RADIAL DIRECTION
C      WL:         WAVELENGTH
C      X,Y,ZG:     GRID POINTS AT AN INTERMEDIATE CALCULATION
C
C      SPECIFY VARIOUS FORMATS FOR FILES
100    FORMAT(E13.6,1X,E13.6,1X,E13.6)
101    FORMAT(A72)
102    FORMAT(E11.4,1X,E11.4,1X,E11.4)
C
      IG=10
      JG=121
      KG=30
      WL=2.0*PI/W
      RO=RO*WL
      ROE=RO-0.08
      JL4=JL-4
      KL4=KL-4
      DPH=2.0*PI/FLOAT(KL-5)
C
C      INPUT THE OGIVE GRID (UNITS ARE IN METERS)
      OPEN(UNIT=2,FILE='ogive.grd',STATUS='OLD')
      READ(2,101) HEADER
      READ(2,101) HEADER
      READ(2,101) HEADER
      DO 1 K=1,KG
        DO 1 J=1,JG
          DO 1 I=1,IG
            READ(2,100) X(I,J,K),Y(I,J,K),Z(I,J,K)
1      CONTINUE
      CLOSE(2)
C
C      ADJUST GRID TO DESIRED DIMENSIONS
C      CHANGE NUMBER OF PHI GRID POINTS (K)
      DO 2 I=1,IG
        DO 2 J=1,JG
          R=0.0
          D=0.0
          DO 2 K=1,KG
            R=R+SQRT(X(I,J,K)**2+Y(I,J,K)**2)
            D=D+Z(I,J,K)
            IF(K.EQ.KG) THEN
              R=R/FLOAT(KG)
              D=D/FLOAT(KG)
              DO 3 KOG=1,KL4
                PH=FLOAT(KOG-1)*DPH
                XG(I,J,KOG)=R*COS(PH)
                YG(I,J,KOG)=R*SIN(PH)
                ZG(I,J,KOG)=D
3              CONTINUE
            END IF
          2      CONTINUE
        C
C      CHANGE NUMBER OF R GRID POINTS (I)

```

```

NR=NINT(ROE/(ZG(IG,1,1)-ZG((IG-1),1,1)))
IF(NR.GT.0) THEN
  DO 5 K=1,KL4
    DO 5 J=1,JG
      DX=XG(IG,J,K)-XG((IG-1),J,K)
      DY=YG(IG,J,K)-YG((IG-1),J,K)
      DZ=ZG(IG,J,K)-ZG((IG-1),J,K)
      DO 5 I=1,NR
        XG((IG+I),J,K)=FLOAT(I)*DX+XG(IG,J,K)
        YG((IG+I),J,K)=FLOAT(I)*DY+YG(IG,J,K)
        ZG((IG+I),J,K)=FLOAT(I)*DZ+ZG(IG,J,K)
5      CONTINUE
    END IF
C
    IRI=NINT(FLOAT(IL)/FLOAT(IG+NR))
    IF(IRI.EQ.0) IRI=1
    IL=((IG-1)+NR)*IRI+1
    DO 6 K=1,KL4
      DO 6 J=1,JG
        DO 6 I=1,IL
          C1=FLOAT(MOD((I-1),IRI))/FLOAT(IRI)
          I1=(I-1)/IRI
          X(I,J,K)=C1*(XG((I1+2),J,K)-XG((I1+1),J,K))+XG((I1+1),J,K)
          Y(I,J,K)=C1*(YG((I1+2),J,K)-YG((I1+1),J,K))+YG((I1+1),J,K)
          Z(I,J,K)=C1*(ZG((I1+2),J,K)-ZG((I1+1),J,K))+ZG((I1+1),J,K)
6        CONTINUE
      C
    C CHANGE NUMBER OF THETA GRID POINTS (J)
      IF(JL4.LT.JG) THEN
        JTHD=NINT(FLOAT(JG)/FLOAT(JL4))
        JTHI=0
        JL=((JG-18)/JTHD)+23
        JL4=JL-4
        DO 10 K=1,KL4
          DO 10 J=1,JL4
            DO 10 I=1,IL
              IF(J.LE.10) THEN
                XG(I,J,K)=X(I,J,K)
                YG(I,J,K)=Y(I,J,K)
                ZG(I,J,K)=Z(I,J,K)
              ELSE IF(J.GE.(JL4-9)) THEN
                J1=JG-(JL4-J)
                XG(I,J,K)=X(I,J1,K)
                YG(I,J,K)=Y(I,J1,K)
                ZG(I,J,K)=Z(I,J1,K)
              ELSE
                XG(I,J,K)=X(I,((J-9)*JTHD+9-(JTHD-1)),K)
                YG(I,J,K)=Y(I,((J-9)*JTHD+9-(JTHD-1)),K)
                ZG(I,J,K)=Z(I,((J-9)*JTHD+9-(JTHD-1)),K)
              END IF
10          CONTINUE
        END IF
      C
      IF(JL4.EQ.JG) THEN
        DO 11 K=1,KL4
          DO 11 J=1,JL4
            DO 11 I=1,IL
              XG(I,J,K)=X(I,J,K)
              YG(I,J,K)=Y(I,J,K)
              ZG(I,J,K)=Z(I,J,K)

```



```

11  CONTINUE
    END IF
C
    IF (JL4.GT.JG) THEN
        JTHD=0
        JTHI=NINT(FLOAT(JL4)/FLOAT(JG))
        JL=(JG*JTHI)-(JTHI-1)+4
        JL4=JL-4
        DO 12 K=1,KL4
            DO 12 J=1,JL4
                C1=FLOAT(MOD((J-1),JTHI))/FLOAT(JTHI)
                J1=(J-1)/JTHI
                DO 12 I=1,IL
                    XG(I,J,K)=C1*(X(I,(J1+2),K)-X(I,(J1+1),K))+X(I,(J1+1),K)
                    YG(I,J,K)=C1*(Y(I,(J1+2),K)-Y(I,(J1+1),K))+Y(I,(J1+1),K)
                    ZG(I,J,K)=C1*(Z(I,(J1+2),K)-Z(I,(J1+1),K))+Z(I,(J1+1),K)
12          CONTINUE
            END IF
C
C  INCREASE GRID POINT DENSITY AT TIPS OF OGIVE
        JTD=10
C
        D=SQRT((XG(1,2,1)-XG(1,1,1))**2+(YG(1,2,1)-YG(1,1,1))**2
1      +(ZG(1,2,1)-ZG(1,1,1))**2)
        NGPD=NINT(FLOAT(NGPD)*D/WL)
        IF (NGPD.EQ.0) NGPD=1
        JL=JL+2*(NGPD-1)*(JTD-1)
        JL4=JL-4
        DO 16 J=1,((JTD-1)*NGPD+1)
            C1=FLOAT(MOD((J-1),NGPD))/FLOAT(NGPD)
            J1=(J-1)/NGPD
            DO 16 K=1,KL
                DO 16 I=1,IL
                    X(I,J,K)=C1*(XG(I,(J1+2),K)-XG(I,(J1+1),K))+XG(I,(J1+1),K)
                    Y(I,J,K)=C1*(YG(I,(J1+2),K)-YG(I,(J1+1),K))+YG(I,(J1+1),K)
                    Z(I,J,K)=C1*(ZG(I,(J1+2),K)-ZG(I,(J1+1),K))+ZG(I,(J1+1),K)
16          CONTINUE
C
        DO 17 J=((JTD-1)*NGPD+2),(JL4-((JTD-1)*NGPD+1))
            J1=J-(JTD-1)*(NGPD-1)
            DO 17 K=1,KL
                DO 17 I=1,IL
                    X(I,J,K)=XG(I,J1,K)
                    Y(I,J,K)=YG(I,J1,K)
                    Z(I,J,K)=ZG(I,J1,K)
17          CONTINUE
C
        J2=JL4-((JTD-1)*NGPD)
        DO 18 J=J2,JL4
            C1=FLOAT(MOD((J-J2),NGPD))/FLOAT(NGPD)
            J1=(J-J2)/NGPD+(J2-(JTD-1)*(NGPD-1))
            DO 18 K=1,KL
                DO 18 I=1,IL
                    X(I,J,K)=C1*(XG(I,(J1+1),K)-XG(I,J1,K))+XG(I,J1,K)
                    Y(I,J,K)=C1*(YG(I,(J1+1),K)-YG(I,J1,K))+YG(I,J1,K)
                    Z(I,J,K)=C1*(ZG(I,(J1+1),K)-ZG(I,J1,K))+ZG(I,J1,K)
18          CONTINUE
C
C  OUTPUT THE GRID FOR PLOTTING
        OPEN(UNIT=3,FILE='ogive.plt',STATUS='UNKNOWN')

```

```

WRITE(3,*) 'TITLE=OGIVE'
WRITE(3,*) 'VARIABLES=X,Y,Z'
WRITE(3,*) 'ZONE T="GRID", I=',IL,', J=',JL4,', K=',KL4
DO 20 K=1,KL4
  DO 20 J=1,JL4
    DO 20 I=1,IL
      WRITE(3,102) X(I,J,K),Y(I,J,K),Z(I,J,K)
20  CONTINUE
CLOSE(3)
C
C CALCULATE GRID POINT DENSITIES
  J=JL/2+1
  KL5=KL-5
  GPKB=KL5/(W*X(1,J,1))
  GPKT=KL5/(W*X(1,2,1))
C
  GPDII=WL/(X(2,(JL/2+1),1)-X(1,(JL/2+1),1))
  GPDIO=WL/(X(IL,(JL/2+1),1)-X(IL-1,(JL/2+1),1))
C
  D=0.0
  DO 30 J=((JTD-1)*NGPD+2),(JL4-(JTD-1)*NGPD)
    D=SQRT((X(1,J,1)-X(1,(J-1),1))**2+(Z(1,J,1)-Z(1,(J-1),1))**2)+D
30  CONTINUE
  GPDJB=WL*FLOAT((JL4-(JTD-1)*NGPD)-((JTD-1)*NGPD+2))/D
C
  D=0.0
  DO 31 J=2,((JTD-1)*NGPD+1)
    D=SQRT((X(1,J,1)-X(1,(J-1),1))**2+(Z(1,J,1)-Z(1,(J-1),1))**2)+D
31  CONTINUE
  GPDJT=WL*FLOAT((JTD-1)*NGPD-1)/AMAX1(D,SS)
C
C CALCULATE SURFACE LENGTH IN J DIRECTION
  DJ=0.0
  DO 32 J=2,JL4
    J1=J-1
    DJ=SQRT((X(1,J,1)-X(1,J1,1))**2+(Z(1,J,1)-Z(1,J1,1))**2)+DJ
32  CONTINUE
C
  PRINT *, 'OGIVE:  RO,ROE,NR,IRI,IL ',RO,ROE,NR,IRI,IL
  PRINT *, 'OGIVE:  JTHD,JTHI,JTD,NGPD,JL ',JTHD,JTHI,JTD,NGPD,JL
  PRINT *, 'OGIVE:  GPD=KB,KT,II,IO,JB,JT ', GPKB,GPKT,GPDII,
1  GPDIO,GPDJB,GPDJT
  PRINT *, 'L,RX,DJ ',Z(1,1,1)-Z(1,JL4,1),X(1,(JL/2+1),1),DJ
C
  RETURN
END
C *****

```

B.2.3 Incident Field

The initial parameters for the incident field are calculated prior to the time loop. The components of the E field vector, displacement vector, and the propagation unit vector are

calculated from the input parameters. The frequencies are also calculated if the Gaussian pulse incident wave is specified. If a Gaussian pulse is used, a delay is introduced so the truncated edge of the pulse is initially located at the point on the surface of the object farthest away from the origin in the direction of the incident wave. The origin is located inside of the PEC scatterer. The section of the code which calculates the initial incident field parameters is shown below.

```

C  CALCULATE INCIDENT FIELD PARAMETERS
C  CONVERT ANGLES FROM DEGREES TO RADIANS
      COSPH=COS(PHI*PI/180.0)
      SINPH=SIN(PHI*PI/180.0)
      COSTH=COS(THI*PI/180.0)
      SINTH=SIN(THI*PI/180.0)
C
C  FIND THE COMPONENTS OF THE E FIELD VECTOR
      AMPX=AMP*(ETHI*COSTH*COSPH-EPHI*SINPH)
      AMPY=AMP*(ETHI*COSTH*SINPH+EPHI*COSPH)
      AMPZ=AMP*(-ETHI*SINTH)
C
C  FIND THE COMPONENTS OF THE DISPLACEMENT UNIT VECTOR FOR DELAY
      XDIS=SINTH*COSPH
      YDIS=SINTH*SINPH
      ZDIS=COSTH
C
C  CALCULATE THE ANGLES AND COMPONENTS OF K (PROPAGATION) UNIT VECTOR
      PHK=PHI-180.0
      THK=-THI+180.0
      XK=SIN(THK*PI/180.0)*COS(PHK*PI/180.0)
      YK=SIN(THK*PI/180.0)*SIN(PHK*PI/180.0)
      ZK=COS(THK*PI/180.0)
C
C  INITIALIZE THE FREQUENCIES
      DO 4 KW=1,KF
        WG(KW)=0.0
4      CONTINUE
C
C  ASSIGN THE FREQUENCY OF THE SINUSOID
      KWM=1
      WG(1)=W
C
C  CALCULATE THE PARAMETERS/FREQUENCIES FOR THE GAUSSIAN PULSE
      IF (ISRC.EQ.1) THEN
        GTH=1.0E-8
        WM=2*PI*(1.0/3.0)*(1/(PI*GPT))*SQRT(-LOG(1.0E-7))
        KWM=INT(1.0/WD*WM)+1
        PRINT *, 'W,WD,KWM ARE: ',W,WD,KWM
        DO 5 KW=1,KWM
          WG(KW)=FLOAT(KW-1)*WD
5      CONTINUE
      END IF
C
C  CALCULATE DELAY SO INCIDENT WAVE, IF GAUSSIAN, PROPAGATES CORRECTLY
      DEL=0.0

```

```

      IF (ISRC.EQ.1) THEN
        DO 6 K=1,KLM
          DO 6 J=1,JLM
            D=XC1(J,K)*XDIS+YC1(J,K)*YDIS+ZC1(J,K)*ZDIS
            IF (D.GT.0.0) THEN
              DEL=AMAX1(DEL,D)
            END IF
6      CONTINUE
      END IF

```

The values of the incident field, either from a sinusoid or Gaussian pulse incident wave, at the surface of the scatterer are calculated in the subroutine SOURCE. The code listing for the SOURCE subroutine is shown below.

```

C *****
C      SUBROUTINE SOURCE(BIX1,BIX2,BIY1,BIY2,BIZ1,BIZ2,DIX1,DIX2,DIY1,
1      DIY2,DIZ1,DIZ2,J,K,TF)
C      PARAMETER(ID=75,JD=125,KD=45,KF=15)
C      COMMON /CC/ XC1(JD,KD),XC2(JD,KD),YC1(JD,KD),YC2(JD,KD),
1      ZC1(JD,KD),ZC2(JD,KD)
C      COMMON /IN/ AMPX,AMPY,AMPZ,DEL,GPD,GPT,ISRC,W,WG(KF),XDIS,YDIS,
1      ZDIS,XK,YK,ZK
C      COMMON /PR/ AMP,CFL,DT,EPS,IB,IL,JL,KL,ILM,JLM,KLM,KWM,REP,RMU,
1      RK,RO,RP,SS,T
C
C      VARIABLES USED ONLY IN THE SOURCE SUBROUTINE:
C      BIX1,2:    X COMPONENTS OF INCIDENT B FIELD AT CELL CENTERS 1,2
C      BIY1,2:    Y COMPONENTS OF INCIDENT B FIELD AT CELL CENTERS 1,2
C      BIZ1,2:    Z COMPONENTS OF INCIDENT B FIELD AT CELL CENTERS 1,2
C      DIS1,2:    SPATIAL DELAY AT A CELL WITH CENTER OF I=1,2
C      DIX1,2:    X COMPONENTS OF INCIDENT B FIELD AT CELL CENTERS 1,2
C      DIY1,2:    Y COMPONENTS OF INCIDENT B FIELD AT CELL CENTERS 1,2
C      DIZ1,2:    Z COMPONENTS OF INCIDENT B FIELD AT CELL CENTERS 1,2
C      GAUS1,2:    INCIDENT FIELD AS A FCT OF W,GPT,GPD,DEL, AND DIS1,2
C      SINW1,2:    INCIDENT FIELD AS A FCT OF W,T, AND DIS1,2
C
C      C1=SQRT(RMU/REP)
C
C      CALCULATE SPATIAL DELAY
C      DIS1=XC1(J,K)*XDIS+YC1(J,K)*YDIS+ZC1(J,K)*ZDIS
C      DIS2=XC2(J,K)*XDIS+YC2(J,K)*YDIS+ZC2(J,K)*ZDIS
C
C      CALCULATE D FIELD IF A SINUSOID IS REQUIRED
C      IF (ISRC.EQ.0) THEN
C        SINW1=SIN(W*(TF+DIS1))
C        SINW2=SIN(W*(TF+DIS2))
C        DIX1=REP*AMPX*SINW1
C        DIX2=REP*AMPX*SINW2
C        DIY1=REP*AMPY*SINW1
C        DIY2=REP*AMPY*SINW2
C        DIZ1=REP*AMPZ*SINW1
C        DIZ2=REP*AMPZ*SINW2
C
C      CALCULATE D FIELD IF A GAUSSIAN PULSE IS REQUIRED

```

```

ELSE
  RGPT=1.0/GPT
  GP=GPD*GPT
  GAUS1=EXP(-(TF+DIS1-DEL-GP)*RGPT)**2)
  GAUS2=EXP(-(TF+DIS2-DEL-GP)*RGPT)**2)
  DIX1=REP*AMPX*GAUS1
  DIX2=REP*AMPX*GAUS2
  DIY1=REP*AMPY*GAUS1
  DIY2=REP*AMPY*GAUS2
  DIZ1=REP*AMPZ*GAUS1
  DIZ2=REP*AMPZ*GAUS2
END IF
C
C  CALCULATE THE COMPONENTS OF THE B FIELD
  BIX1=C1*(YK*DIZ1-ZK*DIY1)
  BIX2=C1*(YK*DIZ2-ZK*DIY2)
  BIY1=C1*(ZK*DIX1-XK*DIZ1)
  BIY2=C1*(ZK*DIX2-XK*DIZ2)
  BIZ1=C1*(XK*DIY1-YK*DIX1)
  BIZ2=C1*(XK*DIY2-YK*DIX2)
C
  RETURN
END
C *****

```

As can be seen in the code, the spatial and time delay is taken into account for the sinusoid and Gaussian pulse incident wave. The location of the grid point on the surface of the scatterer is accounted for in the calculation of the sinusoid incident wave. For the Gaussian pulse, the time delay for the center of the pulse, the time delay due to the length of the object, and the time delay due to the location of the grid point on the surface of the scatterer are used in calculating the amplitude of the pulse.

B.2.4 RCS Convergence Check

The RCS convergence check is used to end the time loop when the RCS values have converged to within a certain value when using a sinusoid incident wave. The RCS values are sampled every 10 degrees every period. If the values are within 0.1 dB of the previously sampled values, convergence has been reached and the time loop ends. The frequency data for the scattered fields are set to zero prior to each period.

```

C *****
  SUBROUTINE RCSCONV(FS,FU,N,NEND,NES,NP,RCSEC,RI)
  PARAMETER(ID=75,JD=125,KD=45,PI=3.14159265359,KF=15)
  COMMON /CC/ XC1(JD,KD),XC2(JD,KD),YC1(JD,KD),YC2(JD,KD),
1          ZC1(JD,KD),ZC2(JD,KD)
  COMMON /CO/ SXI(ID,JD,KD,3),SET(ID,JD,KD,3),SZT(ID,JD,KD,3),
1          V(ID,JD,KD),X(ID,JD,KD),Y(ID,JD,KD),Z(ID,JD,KD)
  COMMON /IN/ AMPX,AMPY,AMPZ,DEL,GPD,GPT,ISRC,W,WG(KF),XDIS,YDIS,
1          ZDIS,XK,YK,ZK
  COMMON /PR/ AMP,CFL,DT,EPS,IB,IL,JL,KL,ILM,JLM,KLM,KWM,REP,RMU,
1          RK,RO,RP,SS,T
  COMPLEX AX,AY,AZ,CX,CY,CZ,DE,FS(JD,KD,6,KF),FU(JD,KD,6,KF),
1          FUEC(JD,KD,6),RI,SUM EK1,SUM EK2,SUM EK3,SUM EJK1,SUM EJK2,
2          SUM EJK3
  DIMENSION RCSEC(19)

C
C VARIABLES USED ONLY IN THE RCSCONV SUBROUTINE:
C SEE MAIN PROGRAM AND RCS SUBROUTINE FOR MOST VARIABLE DESCRIPTIONS
C FUEC: FREQUENCY DATA USED FOR CONVERGENCE CHECK
C RCSCH: RATIO OF CURRENT RCS VALUES TO PREVIOUS RCS VALUES
C RCSCHI: INTERMEDIATE VALUE FOR RCSCH
C
  SME=SQRT(RMU/REP)
  C1=1.0/REP
  C2=1.0/RMU

C
C CALCULATE INTEGRATION LIMITS
  JLM1=JLM-1
  KLM4=KLM-4

C
C NORMALIZE SCATTERED FIELD DATA TO INCIDENT FIELD
  DO 5 K=1,KL
    DO 5 J=1,JL
      RFSB=SQRT(CABS(FS(J,K,1,1))**2+CABS(FS(J,K,2,1))**2
1          +CABS(FS(J,K,3,1))**2)
      DO 6 L=1,3
        FUEC(J,K,L)=FU(J,K,L,1)/RFSB
6      CONTINUE
      RFSD=SQRT(CABS(FS(J,K,4,1))**2+CABS(FS(J,K,5,1))**2
1          +CABS(FS(J,K,6,1))**2)
      DO 7 L=4,6
        FUEC(J,K,L)=FU(J,K,L,1)/RFSD
7      CONTINUE
5    CONTINUE

C
C GENERATE THE BISTATIC RADAR CROSS SECTION
C
  PHO=0.0
  SINPO=SIN(PHO)
  COSPO=COS(PHO)

C
C CHECK FOR CONVERGENCE OF RCS VALUES
  RCSCH=0.0
  DO 10 JO=1,19
    THO=(PI*FLOAT(JO-1)*10.0)/180.0
    SINTO=SIN(THO)
    COSTO=COS(THO)

```

```

C
C  CALCULATE CARTESIAN COMPONENTS OF THE R (OBSERVATION) UNIT VECTOR
      BX=SINTO*COSPO
      BY=SINTO*SINPO
      BZ=COSTO

C
C  PERFORM THE SURFACE INTEGRAL (FREE SPACE GREEN'S FUNCTION)
C  SET INITIAL VALUES FOR THE SURFACE INTEGRAL,J & K LOOPS
      SUMEJK1=(0.0,0.0)
      SUMEJK2=(0.0,0.0)
      SUMEJK3=(0.0,0.0)

C
      DO 20 J=3,JLM1

C
C  SET INITIAL VALUES FOR THE SURFACE INTEGRAL, K LOOP
      SUMEK1=(0.0,0.0)
      SUMEK2=(0.0,0.0)
      SUMEK3=(0.0,0.0)

C
      DO 30 K=1,KLM4

C
C  CALCULATE THE DOT PRODUCT OF R' AND R
      PV=BX*XC2(J,K)+BY*YC2(J,K)+BZ*ZC2(J,K)
      WP=WG(1)*PV

C
C  GENERATE SURFACE INTEGRAL SCALE & METRICS OF OUTWARD NORMAL
      DS=SQRT((0.5*(SXI(IB,J,K,1)+SXI(IB-1,J,K,1)))**2
1          +(0.5*(SXI(IB,J,K,2)+SXI(IB-1,J,K,2)))**2
2          +(0.5*(SXI(IB,J,K,3)+SXI(IB-1,J,K,3)))**2)
      SUMX=AMAX1(DS,SS)
      RSUMX=1.0/SUMX
      XIX=SXI(IB,J,K,1)*RSUMX
      XIY=SXI(IB,J,K,2)*RSUMX
      XIZ=SXI(IB,J,K,3)*RSUMX

C
C  GENERATE THE CROSS PRODUCTS OF THE ELECTROMAGNETIC FIELD
C  THE SURFACE ELECTRIC & MAGNETIC CURRENT DENSITIES
C  FOR THE EQUIVALENCE THEOREM
      AX=C1*(XIY*FUEC(J,K,6)-XIZ*FUEC(J,K,5))
      AY=C1*(XIZ*FUEC(J,K,4)-XIX*FUEC(J,K,6))
      AZ=C1*(XIX*FUEC(J,K,5)-XIY*FUEC(J,K,4))
      CX=C2*(XIY*FUEC(J,K,3)-XIZ*FUEC(J,K,2))
      CY=C2*(XIZ*FUEC(J,K,1)-XIX*FUEC(J,K,3))
      CZ=C2*(XIX*FUEC(J,K,2)-XIY*FUEC(J,K,1))
      DE=C1*(XIX*FUEC(J,K,4)+XIY*FUEC(J,K,5)+XIZ*FUEC(J,K,6))

C
      IF((J.EQ.3).OR.(J.EQ.JLM1)) THEN
          AX=AX/2.0
          AY=AY/2.0
          AZ=AZ/2.0
          CX=CX/2.0
          CY=CY/2.0
          CZ=CZ/2.0
          DE=DE/2.0
      END IF

C
C  PERFORM THE SURFACE INTEGRATIONS FOR NEAR TO FAR FIELD TRANSFORM
      SUMEK1=SUMEK1+WG(1)*(DE*BX+(AY*BZ-AZ*BY)-SME*CX)
1      *CEXP(-(RI*WP))*DS
      SUMEK2=SUMEK2+WG(1)*(DE*BY+(AZ*BX-AX*BZ)-SME*CY)

```

```

1          *CEXP(-(RI*WP))*DS
          SUMEK3=SUMEK3+WG(1)*(DE*BZ+(AX*BY-AY*BX)-SME*CZ)
1          *CEXP(-(RI*WP))*DS
C
30      CONTINUE
C
          SUMEJK1=SUMEJK1+SUMEK1
          SUMEJK2=SUMEJK2+SUMEK2
          SUMEJK3=SUMEJK3+SUMEK3
C
20      CONTINUE
C
C  CALCULATE THE RCS: 4*PI*(R**2)*|Es|**2/|Ei|**2
C  NOTE: NORMALIZATION WRT THE INCIDENT FIELD WAS DONE DURING FT
          RCSE=RCSEC(JO)
          RCSEC(JO)=(CABS(SUMEJK1)**2+CABS(SUMEJK2)**2+CABS(SUMEJK3)**2)
1          /(4.0*PI)
C
C  CHECK FOR CONVERGENCE, CONTINUE OR END TIME LOOP
          RCSE=AMAX1(RCSE,SS)
          RCSCHI=RCSEC(JO)/RCSE
          IF(RCSCHI.LT.1.0) RCSCHI=1.0/RCSCHI
          RCSCH=AMAX1(RCSCHI,RCSCH)
10      CONTINUE
C
C  IF ALL RCS VALUES ARE WITHIN 0.1 DB OF PREVIOUS VALUES,
C  CONVERGENCE HAS BEEN REACHED
          IF(RCSCH.LT.1.0233) THEN
              NEND=N
              NES=NEND
C  RESET THE INITIAL VALUES FOR ALL FOURIER TRANSFORM VARIABLES
          ELSE
              DO 40 L=1,6
                  DO 40 K=1,KL
                      DO 40 J=1,JL
                          FU(J,K,L,1)=(0.0,0.0)
                          FS(J,K,L,1)=(0.0,0.0)
40          CONTINUE
          END IF
          PRINT *, 'N,RCSCH: ',N,RCSCH
C
          RETURN
          END

```

B.2.5 Scattered-Field Threshold Check

The time loop ends if the amplitude of the scattered field is below a predetermined threshold when a Gaussian pulse is used for the incident wave. The amplitude of the scattered field on the virtual surface ($I=IB$) is checked every time step to determine the maximum

amplitude of the scattered field. The time loop which contains the threshold check is listed below.

```

C  PERFORM THE SOLVING SEQUENCE
      N=1
      DO WHILE(N.LE.NEND)
        T=FLOAT(N-1)*DT
        MR=0
        M=1
C        *****
        CALL BC(M,MR)
C        *****
C
        DO 11 MR=1,4
C          *****
            CALL FXI
            CALL GETA
            CALL HZETA
            CALL SUM(MR)
C          *****
11      CONTINUE
C
      IF((N.GT.NES).OR.(N.LT.NBS)) GOTO 10
C  PERFORM FOURIER TRANSFORM
      TF=T+DT
      RU=0.0
      DO 12 KW=1,KWM
        WT=WG(KW)*(TF)
        DO 12 K=1,KL
          DO 12 J=1,JL
C            *****
            CALL SOURCE(BIX1,SN(1),BIY1,SN(2),BIZ1,SN(3),DIX1,SN(4),
1              DIY1,SN(5),DIZ1,SN(6),J,K,TF)
C            *****
C
C  IF GAUSSIAN SOURCE, CHECK AMPLITUDE OF SCATTERED FIELD, END TIME LOOP
C  IF BELOW THRESHOLD
            IF(ISRC.EQ.1) THEN
              RUL=SQRT(U(1,IB,J,K,4)**2+U(1,IB,J,K,5)**2
1              +U(1,IB,J,K,6)**2)
              RU=AMAX1(RU,RUL)
            END IF
            DO 12 L=1,6
              FU(J,K,L,KW)=FU(J,K,L,KW)+(U(1,IB,J,K,L)+SN(L))
1              *CEXP(RI*WT)
              FS(J,K,L,KW)=FS(J,K,L,KW)+SN(L)*CEXP(RI*WT)
12      CONTINUE
            IF((ISRC.EQ.1).AND.(N.GE.100)) THEN
              IF(RU.LE.GTH) NEND=N
              NES=NEND
            END IF
C
C  IF SINUSOID SOURCE, RUN CONVERGENCE CHECK ON RCS VALUES
      IF((ISRC.EQ.0).AND.(ICON.EQ.1)) THEN
        IF(MOD(N,NP).EQ.0) THEN
C          *****

```

```

                CALL RCSCONV(FS,FU,N,NEND,NES,NP,RCSEC,RI)
C                *****
                END IF
                END IF
C
10             N=N+1
                END DO
C  END OF TIME LOOP

```

B.2.6 Bistatic-to-Monostatic Approximation

A description of the bistatic-to-monostatic approximation is given in Chapter 3. The code is not a subroutine for the FVTD code but is an independent program. The RCS values from the "rcsm0.plt" files are used for the HH polarization approximation. The incident wave must be specified with ETH polarization to obtain HH polarization results. To obtain RCS results for the VV polarization, the "rcse0.plt" files are used. The incident wave must be specified with EPH polarization to obtain VV polarization results. The code listed below is for obtaining a monostatic sweep for the ogive for HH polarization. A similar file is used for VV polarization and to obtain the monostatic results for the cone-sphere.

```

C  THIS FORTRAN CODE USES CONTINUOUS BISTATIC VALUES AND SEVERAL
C  MONOSTATIC VALUES TO APPROXIMATE A CONTINUOUS MONOSTATIC
C  SOLUTION FOR THE OGIVE
C
C  SOURCE:  THE MONOSTATIC/BISTATIC APPROXIMATION
C           MICHAEL SCHUH, ALEX WOO, MICHAEL SIMON
C           IEEE ANTENNAS AND PROPAGATION MAGAZINE
C           VOL. 36, NO. 4, AUGUST 1994, PAGES 76-78
C
C  VARIABLE DESCRIPTIONS
C    DEG:    ANGLE AT WHICH MONOSTATIC VALUE IS APPROXIMATED
C    NB:     INDEX FOR BISTATIC RCS VALUE
C    NU:     INDEX FOR FILE UNIT WHICH IS CURRENTLY BEING USED
C    RCSE:   MONOSTATIC AND BISTATIC RCS VALUES READ FROM FILE
C    RCSMON: CALCULATED MONOSTATIC RCS VALUES
C    W:      FREQUENCY IN RADIAN/SEC
C
C           PROGRAM RCSCONV
C           DIMENSION RCSE(721),RCSMON(721),A(15)
C
C  SPECIFY VARIOUS FORMATS FOR FILE INPUTS/OUTPUTS
100  FORMAT(F6.2,1X,E13.6)
C

```

```

OPEN(UNIT=50,FILE='rcsmon_v.plt',STATUS='UNKNOWN')
C
DO 10 N=1,361
  NU=(N+19)/40+11
  OPEN(UNIT=11,FILE='rcsm0_0.plt',STATUS='OLD')
  OPEN(UNIT=12,FILE='rcsm0_10.plt',STATUS='OLD')
  OPEN(UNIT=13,FILE='rcsm0_20.plt',STATUS='OLD')
  OPEN(UNIT=14,FILE='rcsm0_30.plt',STATUS='OLD')
  OPEN(UNIT=15,FILE='rcsm0_40.plt',STATUS='OLD')
  OPEN(UNIT=16,FILE='rcsm0_50.plt',STATUS='OLD')
  OPEN(UNIT=17,FILE='rcsm0_60.plt',STATUS='OLD')
  OPEN(UNIT=18,FILE='rcsm0_70.plt',STATUS='OLD')
  OPEN(UNIT=19,FILE='rcsm0_80.plt',STATUS='OLD')
  OPEN(UNIT=20,FILE='rcsm0_90.plt',STATUS='OLD')
C
  READ(NU,*) FILL,W
  DO 20 I=1,721
    READ(NU,*) DEGREE,RCSE(I)
20  CONTINUE
C
    IF(NU.EQ.11) THEN
      NB=(2*(N-1)+1)
      RCSMON(N)=RCSE(NB)
    ELSE IF(NU.EQ.20) THEN
      NB=-2*(361-N)+361
      RCSMON(N)=RCSE(NB)
    ELSE
      NB=2*(N-((NU-11)*40+1))+(NU-11)*40+1
      RCSMON(N)=RCSE(NB)
    END IF
C
  CLOSE (11)
  CLOSE (12)
  CLOSE (13)
  CLOSE (14)
  CLOSE (15)
  CLOSE (16)
  CLOSE (17)
  CLOSE (18)
  CLOSE (19)
  CLOSE (20)
C
10  CONTINUE
C
  WRITE(50,100) FILL,W
  DO 50 I=1,361
    DEG=FLOAT(I-1)*0.25
    WRITE(50,100) DEG,RCSMON(I)
50  CONTINUE
C
  DO 51 I=362,721
    DEG=FLOAT(I-1)*0.25
    WRITE(50,100) DEG,RCSMON(722-I)
51  CONTINUE
C
  CLOSE (50)
  STOP
  END

```

B.3 Additional Codes

The following code listings were helpful in analyzing and visualizing the FVTD results.

B.3.1 Error Calculations and Metrics

The following MATLAB code calculates the difference, in dB, and the mean-square-error (MSE) between the FVTD and MoM results and the cross-correlation and the Fourier transform of the results.

```
% This program uses several methods to calculate various
% parameters which can be used to compare FVTD and MoM Results
% MATLAB Code
%
% The various methods used include:
% 1. Difference in dB after considering phase by calculating
%    the minimum error between the FVTD result at one point and
%    several surrounding (+/-5 degrees) MoM results.
% 2. Mean Square Error (MSE) using FVTD and MoM results in
%    square meters. Before calculating the MSE, phase is taken
%    into consideration in the same way as for method 1.
% 3. Cross Correlation between FVTD and MoM results in square
%    meters.
% 4. FFT of the FVTD and MoM results in square meters.

% Load the data
load fvtd_hh.prn;
FS=fvtd_hh;
FS=FS(1:4:721); % FVTD results in square meters
FD=10.*log10(FS); % FVTD results in dB

load mom_hh.prn;
MD=mom_hh; % MoM results in dB
MS=10.^(MD./10); % MoM results in square meters

% Method 1
% Calculate difference in dB, Adjust Phase (dB vs. theta)
DDT=[0:1:180];
n=1;
while (n<=5),
    m=1;
    A=100;
    while (m<=6),
        A=min(abs(FD(n)-MD(n-(m-6))),A);
        m=m+1;
    end
    DDT(n)=A;
    n=n+1;
end
n=177;
```

```

while (n<=181),
    m=6;
    A=100;
    while (m<=11),
        A=min(abs(FD(n)-MD(n-(m-6))),A);
        m=m+1;
    end
    DDT(n)=A;
    n=n+1;
end

n=6;
while (n<=176),
    m=1;
    A=100;
    while (m<=11),
        A=min(abs(FD(n)-MD(n-(m-6))),A);
        m=m+1;
    end
    DDT(n)=A;
    n=n+1;
end
DD=max(DDT)
DDT=rot90(DDT,3);
save diffhh DDT -ascii % Save difference values in dB to a file

% Method 2
% Calculate MSE, Adjust Phase if Incorrect (square meters).^2
MSE=0;
n=1;
while (n<=5),
    MSE=MSE+(FS(n)-MS(n)).^2;
    n=n+1;
end
n=177;
while (n<=181),
    MSE=MSE+(FS(n)-MS(n)).^2;
    n=n+1;
end

n=6;
while (n<=176),
    m=1;
    A=100;
    while (m<=11),
        A=min(abs(FS(n)-MS(n-(m-6))),A);
        m=m+1;
    end
    MSE=MSE+A.^2;
    n=n+1;
end
MSE=(1./181).*MSE

% Method 3
% Compute cross-correlation (square meters)
XC=xcor(MS,FS,'coeff');

% Plot the cross-correlation
theta=[0:1:(2*length(FS)-2)];
plot(theta,XC)

```

```

title('Cross-Correlation Between FVTD and MoM results, HH')
xlabel('Theta (Degrees)')
ylabel('XCORR')
axis([170 190 0.95 1]);
save xcorrhh XC -ascii % Save cross-correlation values to a file

% Method 4
% Calculate FFT of FVTD and MoM results (square meters)
% Remove DC value first
n=1;
FST=0;
while (n<=181),
    FST=FS(n)+FST;
    n=n+1;
end
FST=FST./181;
FS=FS-FST;
n=1;
MST=0;
while (n<=181),
    MST=MS(n)+MST;
    n=n+1;
end
MST=MST./181;
MS=MS-MST;

% Use Hamming window
FS=ham(181).*FS;
MS=ham(181).*MS;

% Calculate FFT
FF=abs(fft(FS,1024));
MF=abs(fft(MS,1024));

% Plot the fft's
figure
thetai=(1./1024).*[0:1023];
plot(thetai,FF)
hold on
plot(thetai,MF,'--')
title('FFT of FVTD vs. MoM Results, HH')
xlabel('Cycles/Theta')
ylabel('FFT')
axis([0 0.1 0 0.06]);
save fft_fhh FF -ascii % Save FVTD fft values to a file
save fft_mhh MF -ascii % Save MoM fft values to a file

```

B.3.2 Scattered Electric Field Movie

The listed MATLAB code generates a movie of the scattered field for the cone-sphere.

The plots are contour plots of the scattered electric field.

```

% Movie of Electromagnetic Scattering from 3-D Object (Cone-Sphere)

```

```

% Movie displays contours of the scattered electric field
% MATLAB Code
% As the scattered field data is loaded and displayed at each of N time
% steps, snapshots of the graphics window are saved in a large matrix.
% The total storage required is proportional to the area of the
% graphics window.
% Load the grid
I=49;
J=36;
nframes=40;
fid = fopen('x.grd','r');
[x,Count] = fscanf(fid,'%13e',[I,J]);
fid = fopen('y.grd','r');
[y,Count] = fscanf(fid,'%13e',[I,J]);

% Set up movie frame
fid = fopen('plot50.dat','r');
[E1,Count] = fscanf(fid,'%11e',[I,J]);
% Plot the contour
pcolor(x,-y,E1)
shading('interp')
colormap(jet)
axis([-1.1 1.1 -1.1 1.7]);
axis('square')
caxis([0.0 0.3]);
title('Cone-Sphere Scattered Electric Field Contours (0.869 GHz)')
xlabel('x (m)')
ylabel('y (m)')
hold on
pcolor(-x,-y,E1);
shading('interp')
M=moviein(nframes);

% Record the Movie
for j=1:nframes
    if j==1
        fid=fopen('plot50.dat','r');
    end
    if j==2
        fid=fopen('plot51.dat','r');
    end
    if j==3
        fid=fopen('plot52.dat','r');
    end
    if j==4
        fid=fopen('plot53.dat','r');
    end
    if j==5
        fid=fopen('plot54.dat','r');
    end
    if j==6
        fid=fopen('plot55.dat','r');
    end
    if j==7
        fid=fopen('plot56.dat','r');
    end
    if j==8
        fid=fopen('plot57.dat','r');
    end
    if j==9

```

```

        fid=fopen('plot58.dat','r');
    end
    if j==10
        fid=fopen('plot59.dat','r');
    end
    if j==11
        fid=fopen('plot60.dat','r');
    end
    if j==12
        fid=fopen('plot61.dat','r');
    end
    if j==13
        fid=fopen('plot62.dat','r');
    end
    if j==14
        fid=fopen('plot63.dat','r');
    end
    if j==15
        fid=fopen('plot64.dat','r');
    end
    if j==16
        fid=fopen('plot65.dat','r');
    end
    if j==17
        fid=fopen('plot66.dat','r');
    end
    if j==18
        fid=fopen('plot67.dat','r');
    end
    if j==19
        fid=fopen('plot68.dat','r');
    end
    if j==20
        fid=fopen('plot69.dat','r');
    end
    if j==21
        fid=fopen('plot70.dat','r');
    end
    if j==22
        fid=fopen('plot71.dat','r');
    end
    if j==23
        fid=fopen('plot72.dat','r');
    end
    if j==24
        fid=fopen('plot73.dat','r');
    end
    if j==25
        fid=fopen('plot74.dat','r');
    end
    if j==26
        fid=fopen('plot75.dat','r');
    end
    if j==27
        fid=fopen('plot76.dat','r');
    end
    if j==28
        fid=fopen('plot77.dat','r');
    end
    if j==29

```



```

        fid=fopen('plot78.dat','r');
    end
    if j==30
        fid=fopen('plot79.dat','r');
    end
    if j==31
        fid=fopen('plot80.dat','r');
    end
    if j==32
        fid=fopen('plot81.dat','r');
    end
    if j==33
        fid=fopen('plot82.dat','r');
    end
    if j==34
        fid=fopen('plot83.dat','r');
    end
    if j==35
        fid=fopen('plot84.dat','r');
    end
    if j==36
        fid=fopen('plot85.dat','r');
    end
    if j==37
        fid=fopen('plot86.dat','r');
    end
    if j==38
        fid=fopen('plot87.dat','r');
    end
    if j==39
        fid=fopen('plot88.dat','r');
    end
    if j==40
        fid=fopen('plot89.dat','r');
    end
    [E1,Count] = fscanf(fid,'%11e',[I,J]);
    % Plot the contour
    pcolor(x,-y,E1)
    shading('interp')
    axis([-1.1 1.1 -1.1 1.7]);
    axis('square')
    caxis([0.0 0.3]);
    title('Cone-Sphere Scattered Electric Field Contours (0.869 GHz)')
    xlabel('x (m)')
    ylabel('y (m)')
    pcolor(-x,-y,E1);
    shading('interp')
    M(:,j)=getframe;
end
% Play Movie
movie(M,5,4)

```

B.4 FVTD FORTRAN Code

The entire code can be obtained from Dr. J.S. Shang of Wright Laboratory or the author.

Bibliography

1. M.J. Aftosmis, "Two Compact Cell-Vertex Methods for Computational Electromagnetics," *AIAA Paper 91-1504*. 22nd AIAA Fluid Dynamics, Plasmadynamics, and Lasers Conference, Honolulu HI, June 1991.
2. W. Kyle Anderson and James L. Thomas, "Comparison of Finite Volume Flux Vector Splittings for the Euler Equations," *AIAA Journal*, vol. 24, no. 9, pp. 1453-1460, Sept. 1986.
3. Constantine A. Balanis, *Advanced Engineering Electromagnetics*. New York: John Wiley & Sons, 1989.
4. Jean-Pierre Berenger, "A Perfectly Matched Layer for the Absorption of Electromagnetic Waves," *Journal of Computational Physics*, vol. 114, no. 2, pp. 185-200, Oct. 1994.
5. David G. Bishop and Dale A. Anderson, "A Comparison of Finite-Volume Time-Domain Schemes for the Maxwell Equations," *AIAA Paper 92-0456*. 30th Aerospace Sciences Meeting and Exhibit, Reno NV, Jan. 1992.
6. D.C. Blake and T.A. Buter, "Domain Decomposition Strategies for Solving Hyperbolic Systems on Distributed Parallel Architectures," *AIAA Paper 96-0834*. 34th Aerospace Sciences Meeting and Exhibit, Reno NV, Jan. 1996.
7. D.C. Blake and T.A. Buter, "Overset Grid Methods Applied to a Finite-Volume Time-Domain Maxwell Equation Solver," *AIAA Paper 96-0834*. 27th Fluid Dynamics, Plasmadynamics and Lasers Conference, New Orleans LA, June 1996.
8. Douglas C. Blake, *A Numerical Study of High-Speed Missile Configurations Using a Block-Structured Parallel Algorithm*. MS thesis, AFIT/GAE/ENY/93D-4. Graduate School of Engineering, Air Force Institute of Technology (AU), Wright-Patterson AFB, OH, Dec. 1993.
9. Mary L. Boas, *Mathematical Methods in the Physical Sciences*. New York: John Wiley & Sons, 1983.
10. Richard C. Booton, Jr., *Computational Methods for Electromagnetics and Microwaves*. New York: John Wiley & Sons, 1992.
11. David K. Cheng, *Field and Wave Electromagnetics* (Second Edition). Reading: Addison-Wesley Publishing Company, 1992.
12. J.W. Crispin, Jr. and K.M. Siegel, *Methods of Radar Cross Section Analysis*. New York: Academic Press, 1968.
13. Bjorn Engquist and Andrew Majda, "Absorbing Boundary Conditions for the Numerical Simulation of Waves," *Mathematics of Computation*, vol. 31, no. 139, pp. 629-651, July 1977.

14. N.T. Frink, P. Parikh, and S. Pirzadeh, "A Fast Upwind Solver for the Euler Equations on Three-Dimensional Unstructured Meshes," *AIAA Paper 91-0102*. 29th Aerospace Sciences Meeting, Reno NV, Jan. 1991.
15. K.S. Huh, M. Shu, and R.K. Agarwal, "A Compact High-Order Finite-Volume Time-Domain/Frequency-Domain Method for Electromagnetic Scattering," *AIAA Paper 92-0453*. 30th Aerospace Sciences Meeting and Exhibit, Reno NV, Jan. 1992.
16. Elliot B. Koffman and Frank L. Friedman, *FORTRAN with Engineering Applications* (Fifth Edition). Reading: Addison-Wesley Publishing Company, 1993.
17. Eugene F. Knott, John F. Shaeffer, and Michael T. Tuley, *Radar Cross Section*. Dedham: Artech, 1985.
18. Karl S. Kunz and Raymond J. Luebbers, *The Finite Difference Time Domain Method for Electromagnetics*. Boca Raton: CRC Press, 1993.
19. Yen Liu, "Fourier Analysis of Numerical Algorithms for the Maxwell Equations," *AIAA Paper 93-0368*. 31st Aerospace Sciences Meeting and Exhibit, Reno NV, Jan. 1993.
20. A. H. Mohammadian, V. Shankar, and W.F. Hall, "Application of Time-Domain Finite-Volume Method to Some Radiating Problems in Two and Three Dimensions," *IEEE Transactions on Magnetics*, vol. 27, no. 5, pp. 3841-3844, Sept. 1991.
21. Gerrit Mur, "Absorbing Boundary Conditions for the Finite Difference Approximation of the Time-Domain Electromagnetic-Field Equations," *IEEE Transactions on Electromagnetic Compatibility*, vol. EMC-23, no. 4, pp. 377-382, Nov. 1981.
22. Ralph W. Noack and Dale A. Anderson, "Time-Domain Solutions of Maxwell's Equations Using a Finite-Volume Formulation," *AIAA Paper 92-0451*. 30th Aerospace Sciences Meeting and Exhibit, Reno NV, Jan. 1992.
23. Alan V. Oppenheim and Ronald W. Schaffer, *Discrete-Time Signal Processing*. Englewood Cliffs, New Jersey: Prentice-Hall, 1989.
24. P.L. Roe, "Approximate Riemann Solvers, Parameter Vectors, and Difference Schemes," *Journal of Computational Physics*, vol. 43, pp. 357-372, 1981.
25. Alfred Rosenblatt and George F. Watson, "Concurrent Engineering," *IEEE Spectrum*, pp. 22-37, July 1991.
26. Shepley L. Ross, *Introduction to Ordinary Differential Equations* (Fourth Edition). New York: John Wiley & Sons, 1989.
27. George T. Ruck, Donald E. Barrick, William D. Stuart, and Clarence K. Krichbaum, *Radar Cross Section Handbook*. New York: Plenum Press, 1970.

28. Schuh, Michael J., Alex C. Woo, and Michael P. Simon, "The Monostatic/Bistatic Approximation," *IEEE Antennas and Propagation Magazine*, vol. 36, no. 4, pp. 76-78, Aug. 1994.
29. J.S. Shang, "A Characteristic-Based Algorithm for Solving 3-D, Time-Domain Maxwell Equations," *AIAA Paper 92-0452*. 30th Aerospace Sciences Meeting and Exhibit, Reno NV, Jan. 1992.
30. J.S. Shang, "Characteristic-Based Algorithms for Solving Maxwell's Equations in the Time-Domain," *IEEE Antennas and Propagation Magazine*, vol. 37, no. 3, pp. 15-25, June 1995.
31. J.S. Shang, "Characteristic-Based Methods for the Time-Domain Maxwell Equations," *AIAA Paper 91-0606*. 29th Aerospace Sciences Meeting, Reno NV, Jan. 1991.
32. J.S. Shang, "A Fractional-Step Method for Solving 3-D Time-Domain Maxwell Equations," *AIAA Paper 93-0461*. 31st Aerospace Sciences Meeting and Exhibit, Reno NV, Jan. 1991.
33. J.S. Shang, "A Fractional-Step Method for Solving 3-D Time-Domain Maxwell Equations," *Journal of Computational Physics*, vol. 118, pp. 109-119, 1995.
34. J.S. Shang and Robert M. Fithen, "A Comparative Study of Numerical Algorithms for Computational Electromagnetics," *AIAA Paper 94-2410*. 25th AIAA Plasmadynamics and Lasers Conference, Colorado Springs CO, June 1994.
35. J.S. Shang, K.C. Hill, and D. Calahan, "Performance of a Characteristic-Based, 3-D, Time-Domain Maxwell Equations Solver on a Massively Parallel Computer," *AIAA Paper 93-3179*. 24th AIAA Plasmadynamics and Lasers Conference, Orlando FL, July 1993.
36. J.S. Shang, D.A. Calahan, and B. Vikstrom, "Performance of a Finite Volume CEM Code on Multicomputers," *AIAA Paper 94-0236*. 32nd Aerospace Sciences Meeting and Exhibit, Reno NV, Jan. 1994.
37. J.S. Shang and D. Gaitonde, "Characteristic-Based Time-Dependent Maxwell Equations Solvers on a General Curvilinear Frame," *AIAA Paper 93-3178*. 24th AIAA Plasmadynamics and Laser Conference, Orlando FL, July 1993.
38. J.S. Shang and D. Gaitonde, "On High Resolution Schemes for Time-Dependent Maxwell Equations," *AIAA Paper 96-0832*. 34th Aerospace Sciences Meeting and Exhibit, Reno NV, Jan. 1996.
39. J.S. Shang and D. Gaitonde, "Scattered Electromagnetic Field of a Reentry Vehicle," *AIAA Paper 94-0231*. 32nd Aerospace Sciences Meeting and Exhibit, Reno NV, Jan. 1996.
40. J.S. Shang and S.J. Scherr, "Time-Domain Electromagnetic Scattering Simulations on Multicomputers," *AIAA Paper 95-1966*. 26th AIAA Plasmadynamics and Lasers Conference, San Diego CA, June 1995.

41. J.S. Shang and C.C. Shang, "Concurrent Computation of Electromagnetic Phenomena on the Paragon," *AIAA Paper 95-0592*. 33rd Aerospace Sciences Meeting and Exhibit, Reno NV, Jan. 1995.
42. Vijaya Shankar, "Computational Electromagnetics (CEM) - Development of a Finite-Volume, Time-Domain Solver for Maxwell's Equations," Report NAWCADWAR-93052-60, Contract N62269-90-C-0257, Thousand Oaks, CA: Rockwell International Science Center, 1993.
43. Vijaya Shankar, "Research to Application - Supercomputing Trends for the 90's, Opportunities for Interdisciplinary Computations," *AIAA Paper 91-0002*. 29th Aerospace Sciences Meeting, Reno NV, Jan. 1991.
44. Vijaya Shankar, W.F. Hall, and A.H. Mohammadian, "A CFD-based Finite-Volume Procedure for Computational Electromagnetics - Interdisciplinary Applications of CFD Methods," *AIAA Paper 89-1987*. 9th AIAA Computational Fluid Dynamics Conference, Buffalo NY, June 1989.
45. Vijaya Shankar, W.F. Hall, and A.H. Mohammadian, "A Time-Domain, Finite-Volume Treatment for the Maxwell Equations," *Electromagnetics*, vol. 10, pp. 127-145, 1990.
46. Vijaya Shankar, W.F. Hall, A.H. Mohammadian, and R. Erickson, "CFD Spinoff - Computational Electromagnetics for Radar Cross Section (RCS) Studies," *AIAA Paper 90-3055*. 8th AIAA Applied Aerodynamics Conference, Portland OR, Aug. 1990.
47. Vijaya Shankar, W.F. Hall, A.H. Mohammadian, and C. Rowell, "Algorithmic Aspects and Supercomputing Trends in Computational Electromagnetics," *AIAA Paper 93-0367*. 31st Aerospace Sciences Meeting, Reno NV, Jan. 1993.
48. Joseph L. Steger and R.F. Warming, "Flux Vector Splitting of the Inviscid Gasdynamic Equations with Application to Finite-Difference Methods," *Journal of Computational Physics*, vol. 40, pp. 263-293, 1981.
49. Gilbert Strang, *Linear Algebra and its Applications* (Third Edition). Fort Worth: Saunders College Publishing, 1988.
50. Julius Adams Stratton, *Electromagnetic Theory*. New York: McGraw-Hill, 1941.
51. Allen Taflove, *Computational Electrodynamics: The Finite-Difference Time-Domain Method*. Boston: Artech House, 1995.
52. Allen Taflove, "Re-inventing Electromagnetics: Supercomputing Solution of Maxwell's Equations via Direct Time Integration on Space Grids," *AIAA Paper 92-0333*, 30th Aerospace Sciences Meeting, Reno NV, Jan. 1992.
53. Bram van Leer, "Flux-Vector Splitting For the Euler Equations," Eighth International Conference on Numerical Methods in Fluid Dynamics, Berlin: Springer-Verlag, pp. 507-512, 1982.

54. John L. Volakis and Leo C. Kempel, "Electromagnetics: Computational Methods and Considerations," *IEEE Computational Science and Engineering*, pp. 42-57, Spring 1995.
55. John L. Volakis, Alex C. Woo, Helen T.G. Wang, Michael J. Schuh, and Michael L. Sanders, "Benchmark Radar Targets for the Validation of Computational Electromagnetics Programs," *IEEE Antennas and Propagation Magazine*, vol. 35, no. 1, pp. 84-89, Feb. 1993.
56. Kane S. Yee, "Numerical Solution of Initial Boundary Value Problems Involving Maxwell's Equations in Isotropic Media," *IEEE Transactions on Antennas and Propagation*, vol. AP-14, no. 3, pp. 302-307, May 1966.
57. Li Zhao and Andreas C. Cangellaris, "A General Approach for the Development of Unsplit-Field Time-Domain Implementation of Perfectly Matched Layers for FDTD Grid Truncation," *IEEE Microwave and Guided Wave Letters*, vol. 6, no. 5, pp. 209-211, May 1996.

Vita

Captain Frederick G. Harmon was born the son of [REDACTED] and [REDACTED]

He graduated as valedictorian from Sweet Grass County High School in Big Timber, Montana in 1987.

He joined the Air Force Reserve Officer Training Corps (ROTC) detachment at Embry-Riddle Aeronautical University in Prescott, AZ in 1987. He received his Bachelor of Science degree in Electrical Engineering, graduated Magna Cum Laude, and was commissioned as a second lieutenant in April 1992.

His initial assignment was at the National Air Intelligence Center (NAIC) at Wright-Patterson AFB, OH where he analyzed foreign electronic warfare equipment such as airborne radar jammers, radar warning receivers, and ground-based radar jammers. He was the technical manager for the exploitation of a foreign radar jammer and received the Air Force Commendation Medal for his performance at NAIC. Upon completion of this assignment, he entered the Air Force Institute of Technology to pursue a Master of Science degree in Electrical Engineering specializing in electromagnetic scattering, antennas, and communication and radar systems.

REPORT DOCUMENTATION PAGE			Form Approved OMB No. 0704-0188	
Public reporting burden for this collection of information is estimated to average 1 hour per response, including the time for reviewing instructions, searching existing data sources, gathering and maintaining the data needed, and completing and reviewing the collection of information. Send comments regarding this burden estimate or any other aspect of this collection of information, including suggestions for reducing this burden, to Washington Headquarters Services, Directorate for Information Operations and Reports, 1215 Jefferson Davis Highway, Suite 1204, Arlington, VA 22202-4302, and to the Office of Management and Budget, Paperwork Reduction Project (0704-0188), Washington, DC 20503.				
1. AGENCY USE ONLY (Leave blank)		2. REPORT DATE December 1996		3. REPORT TYPE AND DATES COVERED Master's Thesis
4. TITLE AND SUBTITLE APPLICATION OF A FINITE-VOLUME TIME-DOMAIN MAXWELL EQUATION SOLVER TO THREE-DIMENSIONAL OBJECTS				5. FUNDING NUMBERS
6. AUTHOR(S) Frederick G. Harmon, Captain, USAF				
7. PERFORMING ORGANIZATION NAME(S) AND ADDRESS(ES) Air Force Institute of Technology, WPAFB, OH 45433-6583				8. PERFORMING ORGANIZATION REPORT NUMBER AFIT/GE/ENG/96D-06
9. SPONSORING / MONITORING AGENCY NAME(S) AND ADDRESS(ES) Dr. J.S. Shang Dr. Kueichien Hill Wright Laboratory, WL/FIM Wright Laboratory, WL/XPB, Bldg 254 2645 Fifth St, Ste 6 2591 K St WPAFB, OH 45433-7912 WPAFB, OH 45433-7602				10. SPONSORING / MONITORING AGENCY REPORT NUMBER
11. SUPPLEMENTARY NOTES				
12a. DISTRIBUTION / AVAILABILITY STATEMENT				12b. DISTRIBUTION CODE
13. ABSTRACT (Maximum 200 words) Concurrent engineering approaches for the disciplines of computational fluid dynamics (CFD) and electromagnetics (CEM) are necessary for designing future high-performance, low-observable aircraft. A characteristic-based finite-volume time-domain (FVTD) computational algorithm, developed for CFD and now applied to CEM, is implemented to analyze the radar cross section (RCS) of two three-dimensional objects, the ogive and cone-sphere. The FVTD formulation implements a Monotone Upstream-Centered Scheme for Conservation Laws (MUSCL) algorithm for the flux evaluation and a Runge-Kutta multi-stage scheme for the time integration. Developmental FVTD work for the thesis focused on algorithm development to analyze scattering and obtain RCS data for closed-surface perfect electric conductor (PEC) 3-D objects using either a Gaussian pulse or sinusoid incident wave. In addition, specification of the direction and polarization of the incident wave gives monostatic and bistatic RCS results. Convergence and threshold checks end the simulation run to ensure accurate computation of the RCS. Validation of the characteristic-based FVTD formulation and code for electromagnetic scattering problems is completed by comparing RCS results obtained from the FVTD code to Moment Method and empirical RCS data. The FVTD results for the ogive and cone-sphere are within 3.0 dB of the MoM results and 3.1 dB of the empirical RCS results. Accurate FVTD computations of diffraction, traveling waves, and creeping waves require a surface grid point density of 15-30 cells/ λ .				
14. SUBJECT TERMS electromagnetic scattering, radar cross section, RCS, finite-volume time-domain, FVTD, computational fluid dynamics				15. NUMBER OF PAGES 168
				16. PRICE CODE
17. SECURITY CLASSIFICATION OF REPORT UNCLASSIFIED		18. SECURITY CLASSIFICATION OF THIS PAGE UNCLASSIFIED		19. SECURITY CLASSIFICATION OF ABSTRACT UNCLASSIFIED
				20. LIMITATION OF ABSTRACT UL

GENERAL INSTRUCTIONS FOR COMPLETING SF 298

The Report Documentation Page (RDP) is used in announcing and cataloging reports. It is important that this information be consistent with the rest of the report, particularly the cover and title page. Instructions for filling in each block of the form follow. It is important to *stay within the lines* to meet optical scanning requirements.

Block 1. Agency Use Only (Leave blank).

Block 2. Report Date. Full publication date including day, month, and year, if available (e.g. 1 Jan 88). Must cite at least the year.

Block 3. Type of Report and Dates Covered. State whether report is interim, final, etc. If applicable, enter inclusive report dates (e.g. 10 Jun 87 - 30 Jun 88).

Block 4. Title and Subtitle. A title is taken from the part of the report that provides the most meaningful and complete information. When a report is prepared in more than one volume, repeat the primary title, add volume number, and include subtitle for the specific volume. On classified documents enter the title classification in parentheses.

Block 5. Funding Numbers. To include contract and grant numbers; may include program element number(s), project number(s), task number(s), and work unit number(s). Use the following labels:

C - Contract	PR - Project
G - Grant	TA - Task
PE - Program Element	WU - Work Unit Accession No.

Block 6. Author(s). Name(s) of person(s) responsible for writing the report, performing the research, or credited with the content of the report. If editor or compiler, this should follow the name(s).

Block 7. Performing Organization Name(s) and Address(es). Self-explanatory.

Block 8. Performing Organization Report Number. Enter the unique alphanumeric report number(s) assigned by the organization performing the report.

Block 9. Sponsoring/Monitoring Agency Name(s) and Address(es). Self-explanatory.

Block 10. Sponsoring/Monitoring Agency Report Number. (If known)

Block 11. Supplementary Notes. Enter information not included elsewhere such as: Prepared in cooperation with...; Trans. of...; To be published in.... When a report is revised, include a statement whether the new report supersedes or supplements the older report.

Block 12a. Distribution/Availability Statement. Denotes public availability or limitations. Cite any availability to the public. Enter additional limitations or special markings in all capitals (e.g. NOFORN, REL, ITAR).

DOD - See DoDD 5230.24, "Distribution Statements on Technical Documents."

DOE - See authorities.

NASA - See Handbook NHB 2200.2.

NTIS - Leave blank.

Block 12b. Distribution Code.

DOD - Leave blank.

DOE - Enter DOE distribution categories from the Standard Distribution for Unclassified Scientific and Technical Reports.

NASA - Leave blank.

NTIS - Leave blank.

Block 13. Abstract. Include a brief (*Maximum 200 words*) factual summary of the most significant information contained in the report.

Block 14. Subject Terms. Keywords or phrases identifying major subjects in the report.

Block 15. Number of Pages. Enter the total number of pages.

Block 16. Price Code. Enter appropriate price code (*NTIS only*).

Blocks 17. - 19. Security Classifications. Self-explanatory. Enter U.S. Security Classification in accordance with U.S. Security Regulations (i.e., UNCLASSIFIED). If form contains classified information, stamp classification on the top and bottom of the page.

Block 20. Limitation of Abstract. This block must be completed to assign a limitation to the abstract. Enter either UL (unlimited) or SAR (same as report). An entry in this block is necessary if the abstract is to be limited. If blank, the abstract is assumed to be unlimited.